Examining the Feasibility of Sentinel-1 InSAR data for landslide monitoring and failure forecasting in western Canada.

By

Peter Blenman

B.Sc., University of Victoria, 2023

A Thesis Submitted in Partial Fulfillment of the Requirements for the Degree of

Master of Science

In the School of Earth and Ocean Sciences

University of Victoria

We acknowledge and respect the lək'ʷəŋən peoples on whose traditional territory the university stands and the Songhees, Esquimalt and W̱SÁNEĆ peoples whose historical relationships with the land continue to this day.

Examining the Feasibility of Sentinel-1 InSAR data for landslide monitoring and failure forecasting in western Canada.

By

Peter Blenman

B.Sc., University of Victoria, 2023

Supervisory Committee

Dr. Andrew Schaeffer, Co-Supervisor

School of Earth and Ocean Sciences

Dr. Ed Nissen, Co-Supervisor

School of Earth and Ocean Sciences

Dr. Lucinda Leonard, Committee Member

School of Earth and Ocean Sciences

Abstract

Landslides are geological hazards that significantly threaten human life, infrastructure, and biotic habitat in areas with steep slopes. Precursory signs of a landslide can be undetectable or non-existent, making the evacuation of residents unlikely. The ongoing climatic cycles and geological triggers imposed on regions susceptible to landslides exhibit long-term ground movement superimposed with accelerations due to seismicity or precipitation. Landslide monitoring and forecasting aims to understand the structural dynamics of the slide accelerations to estimate when there will be a catastrophic failure. The thesis explores the potential of InSAR technology for monitoring slope movement in the western Canadian Cordillera. The study takes a two-pronged approach: first, investigating the capability of the technique to detect movement on slopes that have already undergone previous landslide activity, focussing on the Garibaldi Volcanic Complex (GVC) as a case study, and second, analyzing five sites that have recently experienced landslides to determine if InSAR technology could have forecasted the failures.

The InSAR results presented in the thesis show that ground displacement occurred on the slopes of all the study sites, which corresponded with previous landslide activity. However, InSAR results collected during winter months were less detailed and frequent than those collected using a seasonal approach. The forecasting study discovered that all the sites displayed signs of preceding movement on the slopes, which were successfully detected by InSAR. Furthermore, each site encountered extreme weather conditions, resulting in catastrophic failure. The Elliot Lake and Ecstall River sites experienced seismic activity the same afternoon as the landslide events, potentially connected to glacial loss and retreat. Results obtained during snowfall were less reliable than the summer acquisitions.

The results from the thesis demonstrate that the Sentinel-1 mission's temporal resolution is inadequate for creating a real-time monitoring system for landslide-prone slopes in western Canada. Factors that trigger landslide acceleration, such as precipitation, seismicity, and geological processes, can occur over decades or hours. Hence, the primary role of Sentinel-1 in landslide monitoring is identifying large-scale moving slopes. Future InSAR platforms could provide a promising solution with high temporal resolution, making landslide forecasting and monitoring a reality.

Table of Contents

List of Tables

List of Figures

List of Equations

List of Abbreviations

Abbreviation	Full Text
ATM	Atmosphere
APS	Atmosphere Phase Screening
DEM	Digital Elevation Model
DISP	Displacement
ESA	European Space Agency
InSAR	Interferometric Synthetic Aperture Radar
GBInSAR	Ground-Based Interferometric Synthetic Aperture Radar
GNSS	Global Navigation Satellite Systems
GPS	Global Positioning Systems
GVC	Garibaldi Volcanic Complex
IW	Interferometric Wide
LOE	Look Angle Errors
LOS	Line of Sight
MAP	Maximum a posteriori Probability
MT-InSAR	Multi-Temporal Interferometric Synthetic Aperture Radar
PS	Persistent Scatterers
PSI	Persistent Scattering Intensity
SAR	Synthetic Aperture Radar
SBAS	Small Baseline Subset
SLC	Single Look Complex
SNAPHU	Statistical-Cost, Network-flow Algorithm for Phase Unwrapping
StaMPS	Stanford Method for Persistent Scatterers
StaMPS/MTI	Stanford Method for Persistent Scatterers Multi-Temporal InSAR
TRAIN	Toolbox for Reducing Atmospheric InSAR Noise
VV	Vertical-Vertical

1.0 Chapter One: Introduction

Remote sensing techniques involving satellite technologies have made it possible to observe and monitor remote corners of the Earth (Carlà et al., 2017; Hooper et al., 2008). To meet the demand for free remote sensing data, the European Space Agency (ESA) established the Copernicus program in 2014, encompassing the Sentinel constellation. Sentinel-1A, a C-band Synthetic Aperture Radar (SAR) system, was launched in April 2014, followed by Sentinel-1B in April 2016, boasting a temporal resolution of six days. With its high spatial resolution of 5 x 20 m and precise orbits, the Sentinel-1 system enables various research inquiries and methods, including the exploration of surface displacement time series of small areas using Interferometric Synthetic Aperture Radar (InSAR) techniques (Carlà et al., 2017; Intrieri et al., 2019).

The InSAR technique demonstrates a remarkable capacity to detect surface displacements such as slope failures and landslides (Carlà et al., 2019; Intrieri et al., 2019; Michoud et al., 2016), which pose a severe threat to human life and manufactured structures (Crosta et al., 2017). The landslide process involves a single failure event and a sequence of stability states. Detection and prevention measures can be established by monitoring pre-failure movements of a few millimetres daily and their progression over time (Tavenas & Leroueil, 1981). Given the influx of data from Sentinel-1, the potential to identify numerous landslides and prevent casualties through modern Differential InSAR (DInSAR) methods that analyze displacement time series data is enormous.

In 2018, it was revealed that the Maoxian landslide in China, which resulted in 83 fatalities, could have been predicted through the utilization of Sentinel-1 data and InSAR processing (Intrieri et al., 2018). The abundance of freely available data from the Sentinel-1 catalogue raises the question whether this methodology can detect slope movement preceding a landslide event. This thesis investigates the potential and limitations of combining the InSAR technique and Sentinel-1 data for monitoring slope movement in the Coastal Mountain ranges of western Canada.

The thesis adopted a two-pronged approach: first, investigating the capability of the technique to detect movement on slopes that have already undergone previous landslide activity in the Garibaldi Volcanic Complex (GVC) and second, analyzing five sites that have recently experienced landslides to determine if InSAR technology could have forecasted the failures. The findings of this study may have significant implications for future landslide monitoring and risk assessment efforts in the region.

The thesis is structured to outline the climatic factors that contribute to landslide activity, the dynamics of landslides, and the InSAR methodology. The remainder of Chapter one provides an overview of these topics and a literature review on monitoring and forecasting landslides using InSAR. Chapter two presents the results from an InSAR case study on the landslide-prone slopes of the Garibaldi Volcanic Complex. Chapter three examines five regionally distributed sites that have recently experienced landslides and tests whether the catastrophic failures could have been predicted. Finally, Chapters four and five of the thesis delve into the InSAR technique's potential and limitations for monitoring landslides on the western Canadian Cordillera slopes.

In British Columbia, landslides in remote alpine valleys have caused debris flows that have adversely affected streams and riverbeds situated kilometres away. Large catastrophic failures have created large mass wasting events that have disturbed and destroyed infrastructure. This, along with the atmospheric river incident of 2021 that resulted in the shutdown of several highways surrounding the city of Vancouver, prompted an inquiry into the feasibility of using

InSAR technology for landslide monitoring. The following section reviews the influence of climate change on landslide activity in BC's mountains, considering the changing climatic and hydrological conditions.

1.1 Climate Change and Increased Landslide Activity

Climate change is causing extreme weather events that challenge the management of infrastructure and land resources in mountainous regions worldwide (Cui et al., 2019; Flentje et al., 2005; Turner, 2018). Across Canada, over the next 50 years, measurable changes will occur in temperature, precipitation, and other climatic factors (Arias et al., 2021; Crozier, 2010; Weaver, 2003). In mountainous terrain, several climate-driven geohazards will leave infrastructure vulnerable to loss or damage. Depending on location, climate change will trigger positive or negative feedback in groundwater recharge, flow and discharge, flooding and stream erosion, the extent and duration of wildfires, magnitude and frequency of landslides, and the distribution of wildlife and vegetation (Bruce & Cohen, 2004; Masson-Delmotte, et al., 2021; Weaver, 2003).

For communities in the Western Cordillera of Canada (i.e., British Columbia, Yukon, western NWT, and western Alberta), slope stability issues occur through a combination of natural geomorphic processes and anthropogenic activities (Cloutier et al., 2017; Evans, 1982; Porter & Morgenstern, 2013). In British Columbia, for municipalities encroaching on steep mountain terrain (e.g., Kelowna, North Vancouver, Kitimat), changes in the rate and magnitude of surface runoff, groundwater flow, and slope instability are controlled by weather variables (e.g., precipitation, temperature, and barometric pressure), local hydrogeological conditions (e.g., lineaments, bedrock, and surficial deposits), seismicity (e.g., earthquakes, ice quakes, and tectonics), and anthropogenic activities (e.g., housing development, agriculture, and industry).

Managing land use for the next few decades will require a deep understanding of the cumulative climatic factors and their impact on future infrastructure risks.

Another factor that will be impacted by climate change is the acceleration of glacier retreat and loss (Hugonnet et al., 2021). The highest rates of glacier loss on Earth occur in the southern Coast Mountains of Western Canada (Bevington & Menounos, 2022; Hugonnet et al., 2021). As glaciers retreat, they destabilize valley walls, primarily related to debuttressing the bedrock slopes, leading to rockfalls, rockslides and debris flows (Cossart et al., 2008; Deline et al., 2012; Kos et al., 2016). Often, the regions of instability are not where human settlement and infrastructure occur, but large moving rock avalanches, debris flows, and outburst floods can cause damage further downstream from the initial event (Hermanns et al., 2004; Holm et al., 2004; Shugar et al., 2021). Thus, knowledge and understanding of high alpine slope dynamics are imperative for the safety of communities living below these potential hazards (Kilburn & Petley, 2003; Turner 2018).

The mechanisms that contribute to glacier loss and landslides are closely related. As glaciers retreat, the confining weight on the rock below decreases and the rock may slide downhill due to instability (Huggel et al., 2012). In addition, glaciers exert substantial pressure on the Earth's crust, and as they melt, this pressure is released, leading to minor earthquakes or tremors (Bungman et al., 2010; Ekstrom et al., 2006) through isostatic adjustment. Researchers have also documented a surge of seismic activity before ice calving from glaciers (O'Neel et al., 2010; Winberry et al., 2020). The instability caused by realignments in ground deformation due to changes in weight and displacement further makes the slopes susceptible to landslides.

Glacier loss also reduces the ice structures' natural water storage capacity, resulting in a rise in landslides. Glaciers store significant water that is gradually released as the ice melts. However, as glaciers vanish, the water stored inside the ice is released, with the potential to activate landslide events (Evans, 1982; Roberti et al., 2018). In addition, melting glaciers produce significant amounts of meltwater that alters the hydrological regime leading to slope instability (Hugonnet et al., 2021; Huntley et al., 2021).

There is a connection between climate change, glacial loss, and landslides. As glaciers gradually melt away, the rock and soil that was beneath glacier becomes unstable, which leads to a surge in landslide occurrences. Furthermore, the loss of glaciers can alter water infiltration patterns, leading to more landslides and even triggering seismic activity due to pressure release. Therefore, keeping track of glacial loss and its environmental effects is crucial to minimize the risk of landslides to communities downslope of these natural hazards.

1.2 Landslide Basics

Landslides can be defined as the mass wasting or movements of rock, earth, or debris down a slope (Cruden et al., 1991; Cruden and Varnes, 1996; Glade & Crozier, 2005) under the influence of gravity. The balance between the gravitational and the resisting forces of friction and cohesion keep the ground stable. A landslide occurs when the slope-parallel component force of gravity exceeds the resisting forces of the slope. The formula below shows the relationship between the shear strength (resisting forces) and shear stress (slope component of gravity) (Fig. 1). where F is the safety factor. If the $F > 1$, the slope is stable, and conversely, if $F < 1$, the slope is unstable, and a landslide may occur (Eq. 1).

$$\mathrm{F} = \frac{\text{Shear Strength}}{\text{Shear Stress}} \tag{1}$$

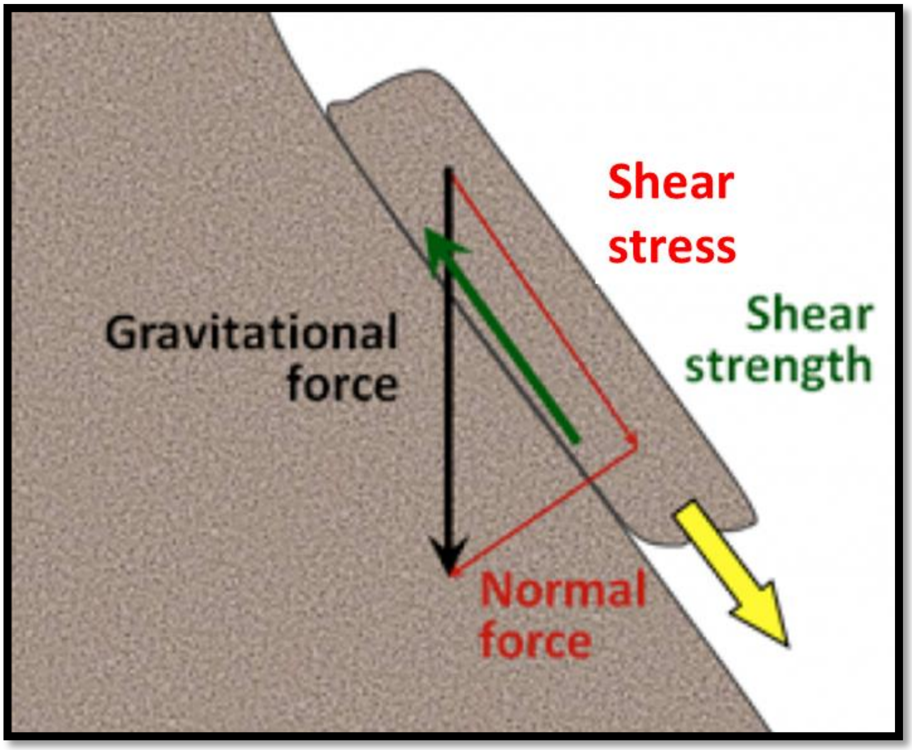

Figure 1 The diagram depicts an instance where the shear strength is less than the shear stress and the rock moves downhill like a landslide (Earle, 2019).

Landslide movement results from various kinematic drivers, including but not limited to gravity, water infiltration, seismic activity, freeze-thaw cycles, and human disturbance. While gravity remains the primary force behind landslides, other contributing factors, such as water infiltration, can significantly accelerate landslide activity (Evans, 1982). The increased water infiltration and temperature fluctuations during winter months accelerate freeze-thaw cycles that fracture and cleave high alpine rock (Roberti et al., 2018). In addition, as previously mentioned, the alteration of water infiltration patterns leads to more landslides due to glacial loss and retreat (Huggonet et al., 2021).

A landslide follows a cycle of stability to failure with slow movements between the two states. The development of a tension crack or a weakened area on the slope typically marks the commencement of a landslide. As time progresses, the gap widens and deepens, causing the material to shift downwards due to the force of gravity (Cruden et al., 1991; Glade & Crozier et al., 2005). The duration of this process can vary depending on the specific circumstances involved, and the landslide may ultimately come to a halt or stabilize in a different state (Tavenas & Leroueil, 1981).

The landslide type and potential hazard depend on the slope's characteristics and the material involved. The classification of landslides is based on the type of movement that occurs. A rotational slide involves movement along a curved rupture surface (Fig. 2). On the other hand, a translational slide happens along a distinct weakness plane between a stable underlying area and the material that is sliding over it (Fig. 2). One of the most common types is a rockslide, which involves the sudden movement of rock down a slope (Cruden et al., 1991). Examples of landslides are shown in figure two: topples, block slides and rock falls. Another common type is a debris flow, the rapid movement of water-saturated soil, sand, and other loose materials down a slope. A debris flow can be compared to a fast-moving stream and can entrain large boulders and trees along the way (Fig. 2) (Glade & Crozier et al., 2005).

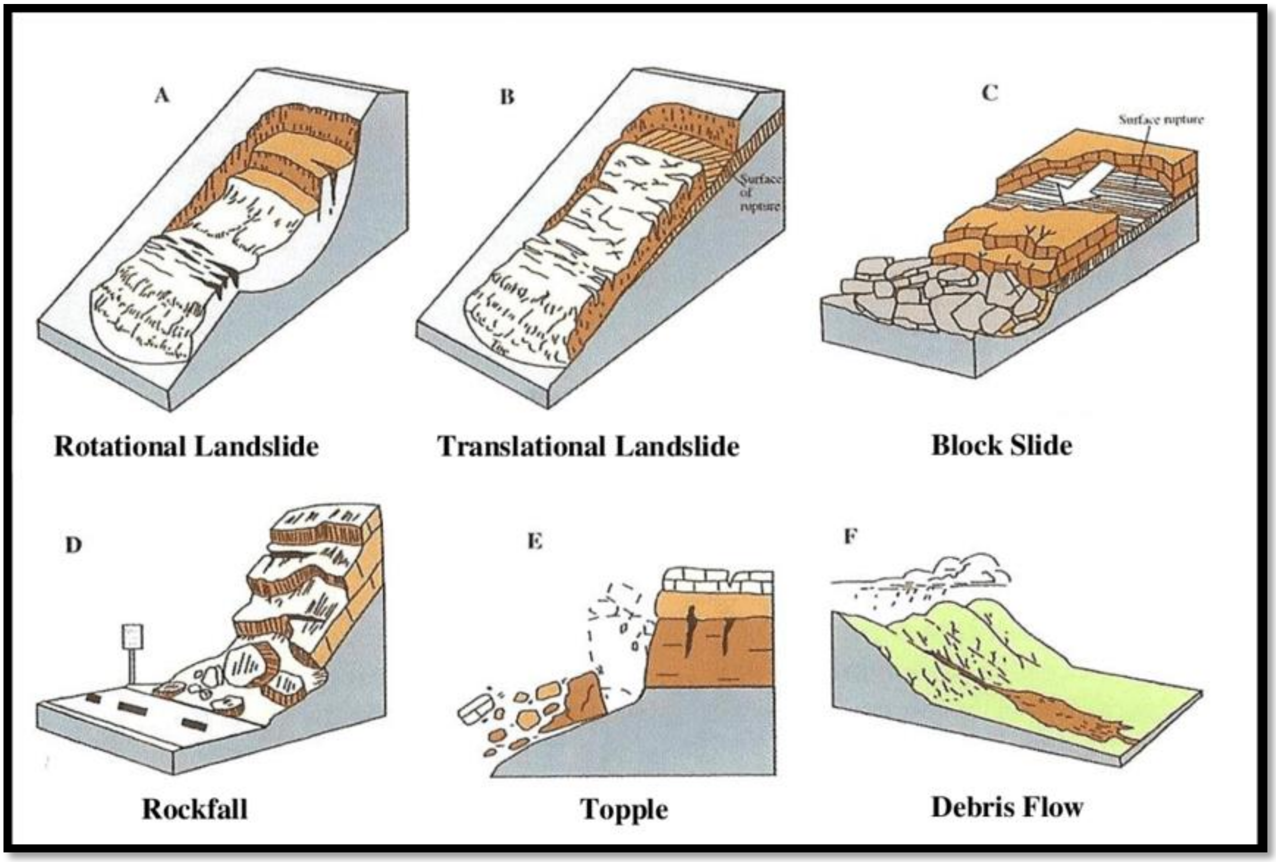

Figure 2 Examples of landslide types (adapted from Schwab et al., 2005).

Landslide monitoring relies on a methodology that analyzes both zones of depletion and accumulation. The zone of depletion refers to the section of the slope where soil and rock are lost due to erosion or water infiltration, and the zone of accumulation is where these materials accumulate at the base of the slope (Cruden and Varnes, 1996; Glade & Crozier, 2007). Characterizing these regions aids in the identification of areas susceptible to landslide failure, and estimation of the quantity of material that may be involved.

Mitigating landslide risks involves various methods, such as engineering, slope stabilization infrastructure, and hazard mapping. One of the most common strategies is constructing retaining walls, which act as a barrier between the slope and nearby structures. These walls protect nearby buildings by preventing debris from reaching them (Lacasse et al., 2009). Slope stabilization can also be achieved using structural elements like anchors or piles. Additionally, creating hazard maps can help identify landslide-prone areas and assist in future land-use decision-making.

Landslides are challenging to predict due to trends of non-linear displacement and stochastic factors such as seasonal precipitation, seismicity, and topographical complexity. The evolution of a landslide unfolds over thousands of years due to cumulative geological factors (e.g., seismicity, rock type, glacial processes) and climatic factors (e.g., temperature and precipitation) (Crosta et al., 2017). The ongoing climatic cycles and geological triggers imposed on regions susceptible to landslides exhibit long-term ground movement superimposed with accelerations due to seismicity or precipitation (Cappa et al., 2004).

Landslide monitoring aims to understand the structural dynamics of slide accelerations to estimate when there will be a catastrophic failure (Intrieri et al., 2019). Precursory signs of a landslide can be undetectable or non-existent, making the evacuation of residents unlikely. Thus, developing early warning systems of slope movement is imperative for the safety of communities living below these potential geohazards (Kilburn & Petley, 2003). Satellite interferometry, a remote sensing application, is an innovative approach for measuring ground deformation. Using satellite-based Synthetic Aperture Radar (SAR) has proven effective in monitoring landslides and deformation on both local and regional scales (Cascini et al., 2010; Mateos et al., 2017; Michoud et al., 2016).

1.3 InSAR and ground deformation monitoring

1.3.1 Introduction

The first successful application of SAR was accomplished by extracting the elevation information of the surface of Venus and the Moon (Rogers & Ingalls, 1969). The Synthetic term in SAR is because the antenna is enlarged virtually to increase the spatial resolution. The orbit movement in the azimuth direction of the satellite is used as the virtual antenna length. The length of the synthetic antenna is the entire distance from where a scatterer enters the radar beam until it leaves. The beam changes in width in range direction, and shorter period scatterers are detected with a narrow beam and far-range scatterers with a wider beam (Ferritti et al., 2007). The energy transmitted from the antenna over the scene is equal; thus, the imaging is uniform for the entire image.

InSAR is a remote sensing technique that uses two or more radar images of the exact same location taken at different times to detect changes in the ground surface. A series of radar images are acquired by satellites or aircraft of the same location over time. The acquired images are then processed to remove noise or interference, and co-registered, or aligned, with each other based on their time and location.

This process is called interferometry, which compares two or more radar images of the exact location to determine any changes in the ground surface (Hooper et al., 2004; Wright et al., 2004). This is achieved by measuring the phase difference between the two images or the amount of change in the radar signal. An interferogram visually represents the phase difference between two radar images (Rocca, 1997). It shows the areas of the ground surface that have deformed between the two images. The interferogram is then analyzed to determine the amount and location of any ground surface changes (Gabriel et al., 1989). The results yield theoretical millimetre precision, but studies have shown accuracy compared to ground instrument data to be ~4-8 mm, dependent on the number of interferograms generated (Bamler & Hartl, 1998). Overall, the InSAR methodology is robust for remote sensing and monitoring ground surface changes.

1.3.2 InSAR geometries and basics

The satellite acquires imagery in a slant angle geometry mode. Thus, the displacement values reference the satellite's Line of Sight (LOS) (Fig. 3). The LOS displacement includes components of both vertical and horizontal movement towards or away from the satellite. Mathematical methods have been developed to deconstruct the geometry of the LOS measurements to obtain an actual vertical component and the east/west horizontal geometry. Acquiring north/south geometries is not possible due to the polar orbit of the Sentinel-1 constellation. Deconstructing the LOS geometry is essential for accurately comparing displacement velocities acquired from space to ground-based monitoring sensors (Crosetto et al., 2003).

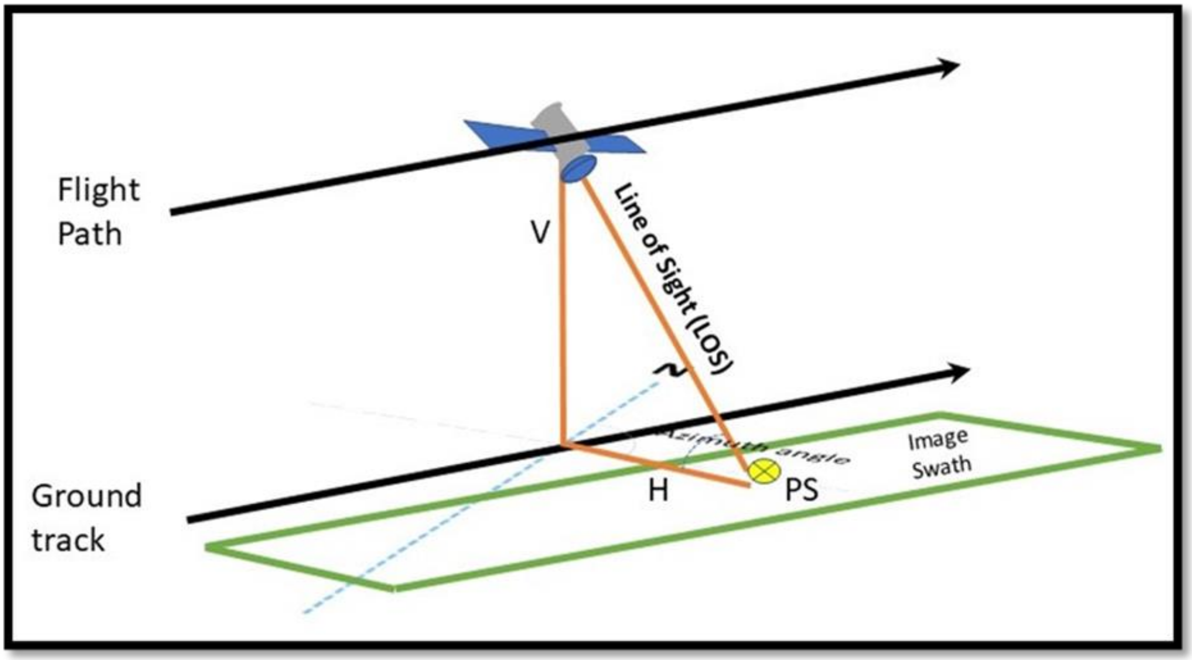

Figure 3 Schematic diagram of the LOS in relation to the satellite's path (PS=Persistent Scatterer, V=Vertical, H=Horizontal (Modified from Crosetto, 2003).

Multiple satellite sensors and antennae lengths have been built for InSAR. Starting in the early 1990s with the JERS and ERS-1 constellations, SAR data have been acquired over the last 30 years (Fig. 4). The satellite sensors are differentiated by their antenna length and classified by their Band name. The C-Band is 3.8-7.5 cm long and is the most popular sensor; the L-Band is 15-30 cm, and the X-Band is in the 2.4-3.8 cm range (Dini et al., 2020). The antenna length corresponds to the penetration capability of the sensor. The L-band has the most extended antennae and can penetrate vegetation and tree cover, while the C and X-band antenna are short and are used to penetrate snow and ice, respectively.

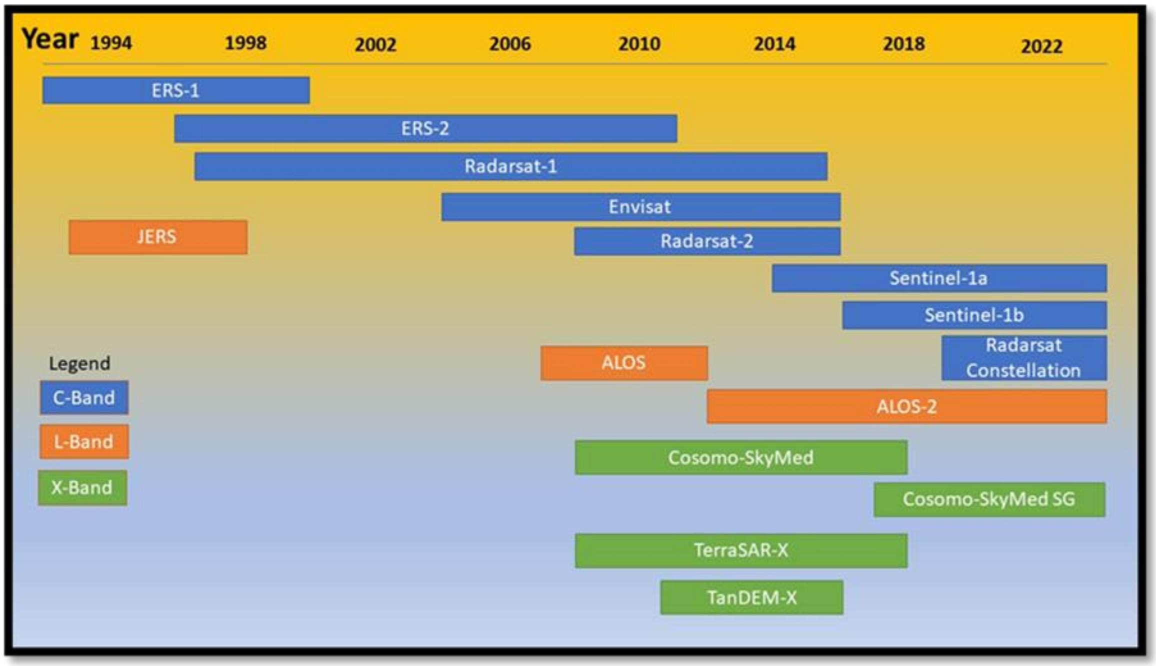

Figure 4 Timeline of past and present satellites and their band type used for InSar analysis.

In this thesis, data were exclusively obtained from the Sentinel-1 constellation mission. To provide a brief overview of the sensor's specifications, Sentinel-1, a C-band transmits electromagnetic microwave pulses with a wavelength of 5.6 cm to illuminate a swath on the Earth's surface and subsequently collects the resulting backscatter within that swath (Yague-

Martinez et al., 2016). The collected image utilizes side-looking geometry at an angle of 20°-45° to the right. The angle increases as the sensor moves from near-range to far-range positions. The sensor has both ascending and descending orbits and is circumpolar. Ground range refers to the direction perpendicular to the azimuth from off-nadir. In contrast, slant range refers to the direction along the LOS from the sensor as determined through the incident angle (Fig. 3) (Ferretti et al., 2001; Yague-Martinez et al., 2016).

1.3.3 InSAR calculations and outputs

The SAR sensor is an active system that emits microwave radiation to the Earth's surface and receives the signal reflection referred to as backscatter. The benefit of an active sensor is that it works any time of the day and is not impeded by cloud cover. The results are the backscattered signals expressed as a complex image (c) with both amplitude (A) and phase (Φ), with (i) the imaginary number (Eq.2) (Strozzi et al., 2002).

$$\mathrm{c} = \mathrm{A}e^{i\Phi} \tag{2}$$

When pairing two SAR images from different periods and look angles but of the same location, one image is deemed the reference (r) and the other the secondary (s). The interferogram (I) is a complex combination of the images' phase differences. In Equation 3, the difference between the phases (Φ_r) and (Φ_s) is expressed as the interferometric phase (Φ_{ip}) and is defined in Equation #4 (Ramirez et al., 2020).

$$\mathrm{I} = \mathrm{C_r}\,\mathrm{C_s} = \mathrm{A_r}\,\mathrm{A}_s^{e^{i(\Phi r - \Phi s)}} \tag{3}$$

The co-registered images are cross-multiplied, forming the interferogram that contains the phase difference between the images. Each pixel in the interferogram is the difference in acquisitions in each SAR pixel. The resulting interferogram contains phase variation Φ from multiple factors, including the flat-earth phase Φ_{flat} (curvature of the earth), the topographic phase Φ_{DEM} (topography of the earth-Digital Elevation Model), atmospheric factors Φ_{atm} (temperature, precipitation, and humidity), signal noise Φ_{noise} (backscattering differences), and finally the surface deformation between the two images Φ_{disp} (Eq. 4) (Rocca, 1997).

$$\Phi_{\mathrm{r}} - \Phi_{\mathrm{s}} = \Phi_{\mathrm{ip}} = \Phi_{\mathrm{DEM}} + \Phi_{\mathrm{flat}} + \Phi_{\mathrm{disp}} + \Phi_{\mathrm{atm}} + \Phi_{\mathrm{noise}} \quad (4)$$

This formula assumes that the Φ_{flat} and Φ_{DEM} are equal for both images and can be estimated by manipulating the variable’s displacement or topography heights. In addition, the best results are achieved when the atmospheric conditions and signal noise are kept as small as possible (Rocca, 1997).

1.3.4 Quality assurance through coherence

The InSAR technique creates imagery across the entire satellite swath, though not every pixel contains information with veracity. When there is too much change between ground targets and satellite acquisition, the sum of the backscattering signal varies, resulting in decorrelation. Coherence indicates how identical each image is to its pair by quantifying the impact of decorrelation on the interferogram result. The coherence is measured on a scale of 0-1, with values close to 1 indicating locations completely in phase and values close to 0 out of phase (Lu et al., 2018). Generally, areas that are vegetated or are waterbodies have low coherence because the interferogram does not recognize these features across imagery dates - there is too much change in the returned signal.

The baseline is the line between the different locations after satellite repetition. As an essential factor in InSAR, the baseline describes the spatial or temporal geometric relations between the antennas and the slant range; the high-accuracy baseline can enhance interferometry of receiving the signal, but poor-quality baseline will cause interference loss and lead to low precision of the LOS measurement. Thus, the longer the spatial baseline, the weaker the interference of the images, so a longer baseline can decrease the accuracy of the InSAR product (Wang, 2015).

The interferometric baseline is the distance between the two satellites (orbits) in the plane perpendicular to the orbit (Fig. 5). Its projection perpendicular to the slant range is the perpendicular baseline.

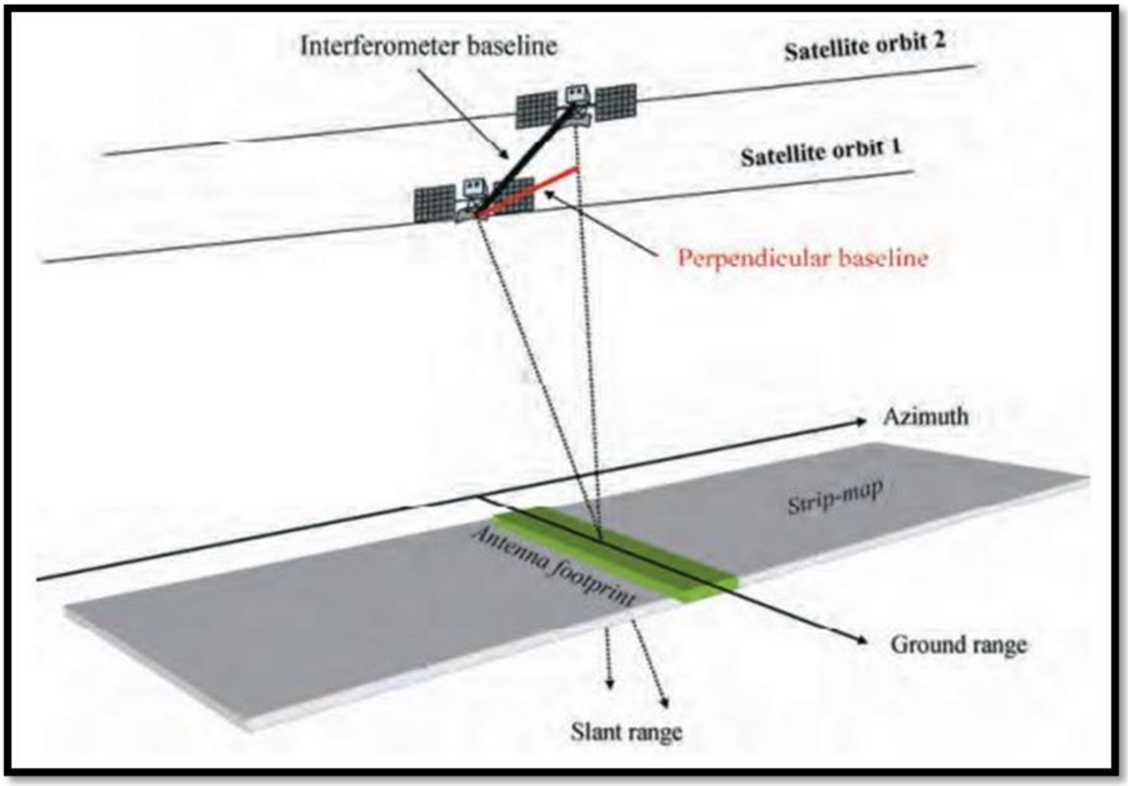

Figure 5 Visualization of the distance between two different satellite orbits. The perpendicular baseline is the red line in the image (Ferretti et al., 2007).

Coherence is related to the perpendicular and temporal baselines. The smallest distance and time interval between the satellite images has the best coherence. The inverse of long perpendicular and time intervals yields interferograms with low coherence. In addition, longer look angles may have different backscattering characteristics, increasing error in the final interferogram (Rocca, 1997).

1.3.5 Phase unwrapping

The phase in the interferogram is only known within the scale of 2π, and the phase must be unwrapped for the analyst to ascertain any actual world values. Phase unwrapping flattens the 2π phase cycles into the LOS difference between the two images. Thus, the unwrapped results should be interpreted as a relative LOS displacement between the pixels of two images. The image below illustrates the flattening of the 2π phase results (Fig. 6). The quality of the unwrapped phase depends on the coherence of the area of interest and a minimum coherence of 0.3 is suggested. Thus, reliable results can only be expected if high coherence values are associated with pixels of interest (Rocca, 1997).

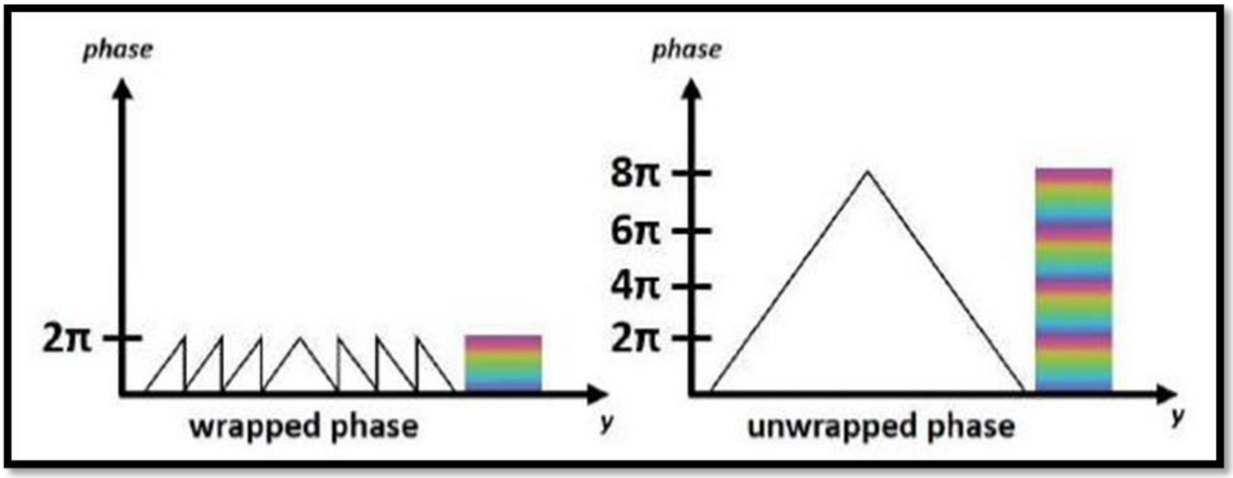

Figure 6 Diagram illustrating the unwrapped versus wrapped phase (Braun, 2021).

One method created to acquire higher-quality unwrapped phase data is the Statistical-Cost, Network-flow Algorithm for Phase Unwrapping (SNAPHU) (Chen & Zebker, 2001). The phase unwrapping is done as a maximum a posteriori probability (MAP) estimation problem, where the observable data are used to compute the most likely unwrapped solution. SNAPHU incorporates three built-in statistical models for topography, deformation, and smooth generic data. The optimization program is solved using a network-flow technique that minimizes the total cost of paths through the network. An iterative optimization procedure analyzes all paths until the optimal solution is found (Chen & Zebker, 2001; Hooper, 2010).

The steps of the SNAPHU algorithm are first to create a network of pixels representing the interferogram. Each pixel is assigned a cost proportional to its phase value, aiming to find the optimal path through the network that yields the lowest total cost. The next step is to define the sources and sinks in the network. Sources are pixels with known phase values, while sinks are pixels with unknown phase values that need to be unwrapped (Chen & Zebker, 2001). To find the optimal path, the algorithm constructs a flow graph that models the network's topology and assigns flow values to its edges to maximize the flow from the sources to the sinks (Hooper, 2010). The next step is calculating the residual or the difference between the observed phase and the predicted phase along each path in the network. The residual is then compared to a threshold value to determine if it should be considered a valid path. This process is repeated until all paths have been analyzed and the optimal solution has been found (Chen & Zebker, 2001).

Although SNAPHU has high accuracy for phase unwrapping, there are still limitations to using only two images related to temporal and geometric decorrelation and atmospheric inhomogeneities (Delgado et al., 2019). These issues degrade the accuracy of results obtained, and differential InSAR only allows for comparing two dates (typically before and after a significant event). However, Multi-temporal InSAR techniques (MT-InSAR) involving processing multiple acquisitions in time can rectify these problems with single-pair interferograms. One such method called Persistent Scattering Intensity (PSI) relies on the identification of single targets (called Persistent Scatterers, PS) that are coherent over longtime intervals and for wide look-angle variations to measure changes in phase positions (Ferretti et al., 2001; Hooper et al., 2004; Crosetto et al., 2016).

1.3.6 Persistent scatterers

InSAR persistent scattering methodology is based on identifying stable radar reflectors (PS) on the surface of the Earth that remain fully coherent over time (Fig. 7). PS are usually located on artificial structures such as buildings, roads, and bridges and natural features such as rocky outcrops, cliffs, and areas devoid of vegetation. The methodology involves acquiring a series of radar images of the same area over time. The radar images are then processed to identify the persistent scatterers and measure their phase differences between each pair of two images (Ferretti et al., 2001). The phase differences indicate the changes in distance between the radar and the ground surface, which can be attributed to deformation, such as subsidence or uplift. The measurements of phase differences are combined to map the deformation between the two satellite images. High-precision surface deformation measurements are valuable for geological hazards, infrastructure monitoring, and land-use planning (Hooper et al., 2008).

Hooper (2007) simulated the phase stability of distributed and persistent scatterers over 100 samples. The study found that the Distributed Scatterers (DS) changed randomly over time while the persistent scatterers were stabilized by the contribution of the one dominant scatterer (Fig. 7) (Hooper et al., 2007).

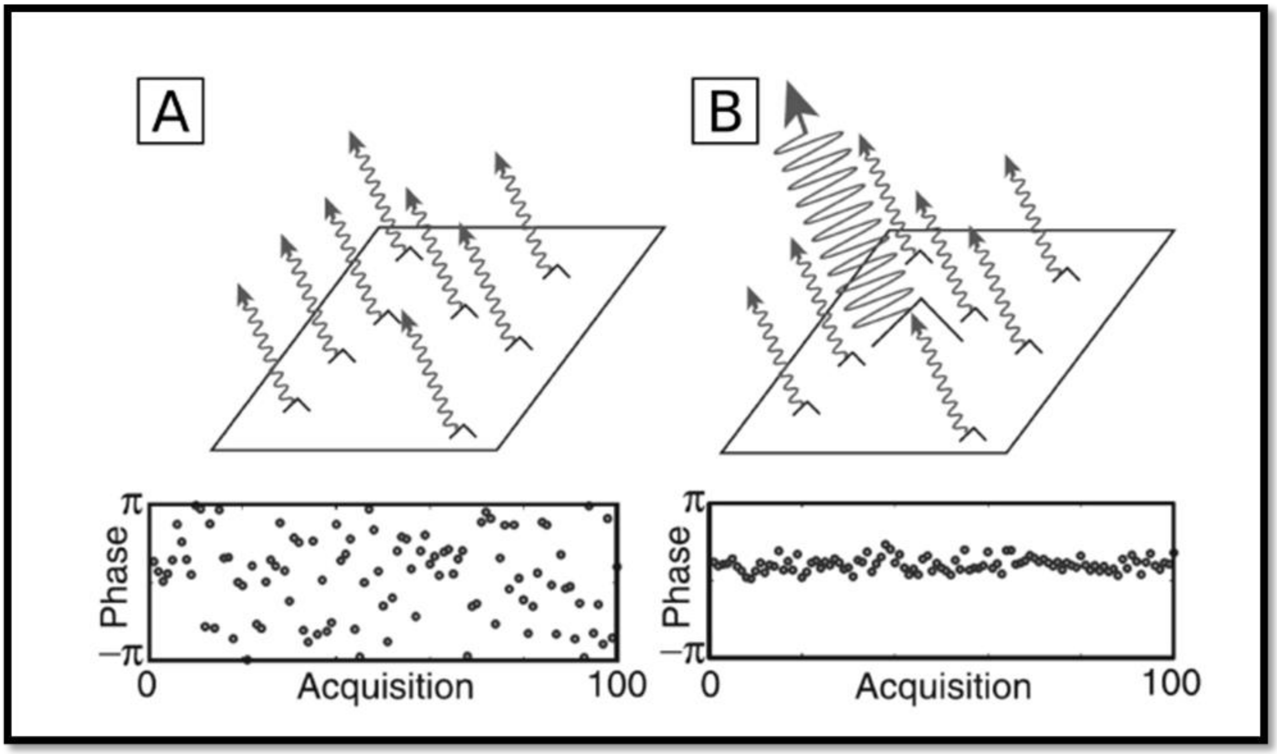

Figure 7 Examples of a simulated phase stability of distributed scatterers (A) and persistent scatterers (B) over 100 samples. The DS phase changes randomly over time, whereas the PS phase is stabilized by the major phase contribution of one dominant scatterer. (Hopper et al., 2007).

Various methods have been developed to isolate PS and unwrap the phase signal. Two of the most used are the SqueeSAR algorithm introduced by Ferretti et al. (2001) and the Stanford Method for Persistent Scatterers Multi-Temporal InSAR (StaMPS/MTI) (Hooper et al., 2012). The SqueeSAR software is operated at a cost, and the StaMPS/MTI is open-source and free. In addition, the StaMPS uses amplitude and phase analysis to identify the dominant scatterers. StaMPS also utilizes the SNAPHU algorithm for the final phase unwrapping of the designated PS. This thesis uses the StaMPS/MTI approach, and the fundamentals of this approach are briefly summarized below.

StaMPS (Stanford Method for Persistent Scatterers) is a software package that utilizes the persistent scatterer method developed to work in areas that exhibit non-steady deformation. The original development of StaMPS was undertaken at Stanford University and is now continued by the University of Iceland, Delft University of Technology, and the University of Leeds. StaMPS/MTI is an extended version of StaMPS, including a small baseline method and a combined multi-temporal InSAR method (Hooper et al., 2012).

A co-registered stack of processed interferograms is needed before the StaMPS software processing. The reference image is calculated before the interferogram processing with the image with the lowest temporal and perpendicular baselines out of the entire stack. Once the interferograms are all co-registered and aligned, the initial PS candidates are found based on the amplitude dispersion index D_A (Ferretti et al., 2001).

$$D_A = \frac{\sigma_A}{\mu_A} \tag{5}$$

In equation 5, the D_A is calculated by dividing the standard deviation σ_A by the mean μ_A of one pixel over all the interferograms of the time series. Because of the research conducted by Ferretti (2001) and Hooper (2007) demonstrating the correlation between phase stability and amplitude (Fig. 7), the amplitude filter is used to determine PS candidates. The PS candidates are further evaluated based on noise estimation, and PS that exhibit higher noise than the threshold are filtered out of the PS selection (c.f. Hooper et al., 2007). The PS are unwrapped using a 3D-unwrapping algorithm SNAPHU (c.f. Hooper et al., 2007; Hooper et al., 2010). Finally, the Atmosphere Phase Screening (APS), orbit and Look Angle Errors (LAE) are estimated and subtracted, resulting in the LOS displacement (Hooper et al., 2007).

The PS methodology finds pixels that are phase stable over time, generally in urban areas and areas clear of vegetation. In the context of landslide monitoring, these regions are often in remote, non-urban alpine areas. One method overcomes this by processing the distributed scatterers in addition to the PS called the Small Baseline Subset (SBAS). Instead of one reference image for the whole stack, smaller stacks are created with shorter temporal and perpendicular baselines (Fig. 8).

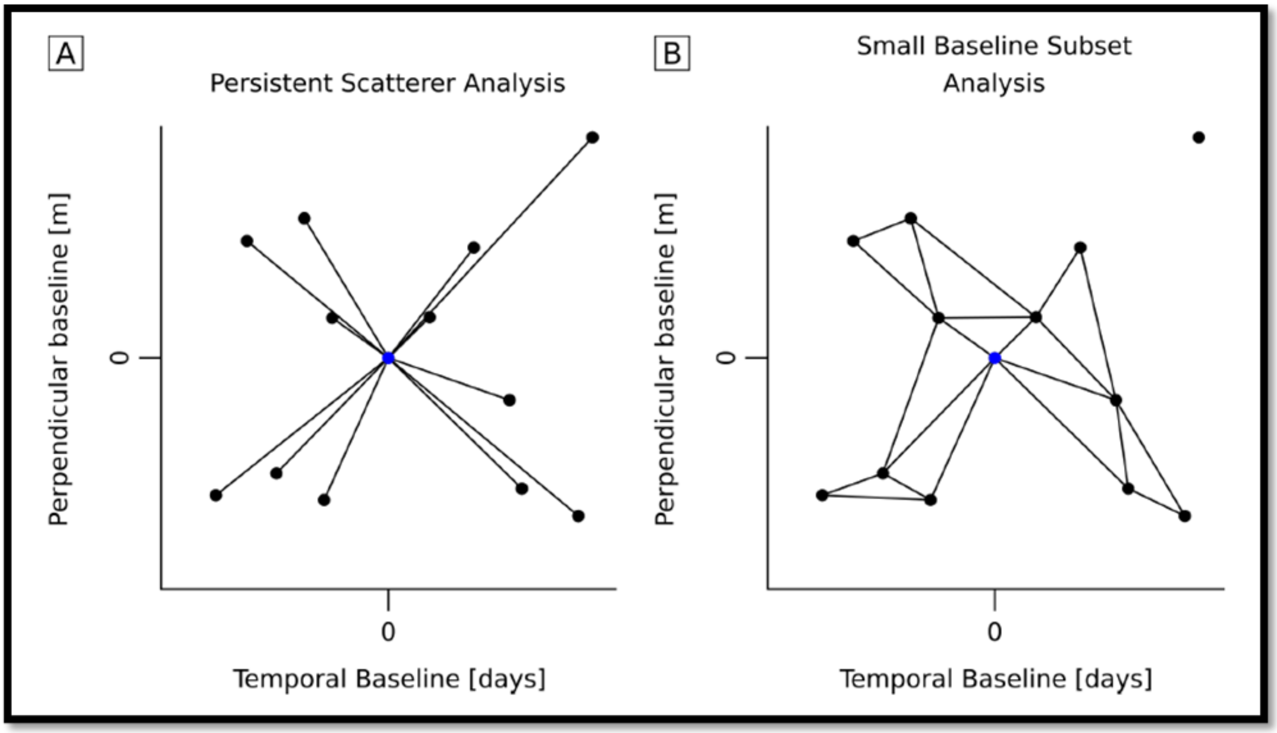

Figure 8 Conceptualized baseline plots for (A) PS processing and (B) SBAS processing. The perpendicular baseline is on the Y-axis, and the temporal baseline is on the X-axis (Hoeser, 2018).

This thesis only used the StaMPS software method for the PS methodology. Further details of the steps and various parameters chosen are covered in chapter two.

1.4 InSAR and Landslide Forecasting

Landslide monitoring and forecasting aim to understand the structural dynamics of slide accelerations to estimate when there will be a catastrophic failure (Intrieri et al., 2019). Monitoring involves regular measurements of a landslide to detect any signs of deformation, while forecasting calculates the probability of catastrophic failure within a defined time interval.

The term "prediction" is used in literature to refer to a future time and place of catastrophic failure.

Slopes that exhibit landslide activity are monitored from the ground with in-situ methods such as seismometers, and Global Navigation Satellite Systems (GNSS). Extensometers quantify the strain rate of the landslide region, while GNSS instrumentation measures ground movement over time. Often, these methods are part of a multimethod approach to monitoring the landslide area. In-situ methods have detected the movement of large landslides but struggle to detect the movement of more minor landslides (Barla et al., 2010; Crosta et al., 2017; Del Ventisette et al., 2012; Gaffet et al., 2010).

Ground-based in-situ methods often fail to detect ground movement due to limitations in the scale of the monitoring program. Predicting a landslide with accuracy is constrained by the limitations of ground-based instrumentation: inadequate field of view of the instrument, the sparse number of data points, ignorance that the slope is unstable, and logistical and economic constraints of the site (Carlà et al., 2019). It is not easy to detect the movement of a mountain slope if the entire slope is moving. When the ground-based monitoring is only deployed in a uniformly moving region, all the results will show no movement as they are relative. In addition, the cost and human resources included in maintaining in-situ monitoring often create sparse networks and, subsequently, fewer data (Carlà et al., 2019). Thus, it is imperative to have large-scale monitoring capabilities to forecast landslide activity effectively.

InSAR monitoring of ground movement and displacement from space allows for large-scale monitoring of slopes in landslide-risk regions at a low cost to the end user. This section examines the literature about landslide prediction and satellite imagery capable of calculating displacement velocities. It focuses on articles related to satellite SAR imagery and the monitoring and detection of precursor tertiary creep or ground deformation before a landslide event.

1.4.1 Creep curve and inverse velocity models

This review defines failure or ruptures as a complete material paroxysmal collapse (e.g., landslides, rockfalls, and debris flow). Most failure-forecasting methodology relies on the premise that slopes undergo displacements that accelerate with a creep curve before failure (Fig. 9) (Carlà et al., 2019; Tavenas & Leroueil, 1981). In Figure 9, the primary creep exhibits a decreasing logarithmic strain rate, the secondary creep has a constant strain rate, and the tertiary stage has an accelerating creep rate, which leads to failure. For example, a landslide has occurred. As it settles, it undergoes primary creep; once the slide is stable, it is in the secondary creep. Something triggers the landslide to accelerate again, and the tertiary creep begins. This creep curve cycle of stability and accelerated creep periods is only a model to understand landslide cycles. The primary goal of time of failure forecasting is to accurately quantify the tertiary creep stage's acceleration (Intrieri et al., 2019).

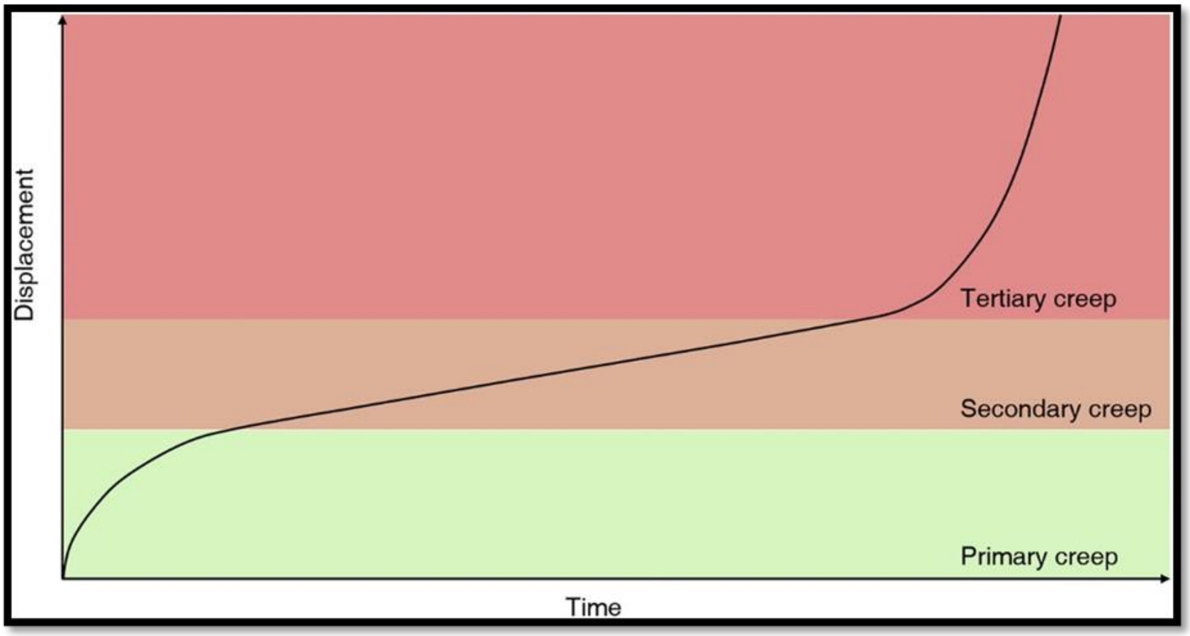

Figure 9 Three-state interpretation of creep behaviour (Intrieri et al., 2019).

Terzaghi (1950) foresaw the potential of quantifying slope mechanics to predict the time of failure. Saito and Uezawa (1961) developed a method to forecast the time of failure based on the tertiary creep curve. The authors developed an empirical formula based on the relationship between the constant strain rate and the time before catastrophic failure (Saito & Uezawa, 1961). Saito (1969) then refined the formula with a graphical approach, which was further simplified by Fukuzono (1985), and now the inverse velocity plot methodology is often used to forecast the time of failure (Intrieri et al., 2019).

Fukuzono (1985) proposed that at the onset of acceleration, there are two possible outcomes: complete failure where the velocity is equal to infinity or no failure and the velocity decreases. The graphical method developed by Fukuzono plots the inverse velocity versus time. Thus, if the landslide velocity is slow and steady, the line plotted is parallel to the time axis. Conversely, the plotted line will cross the time axis if the slide's velocity increases. The point where the plotted line crosses the time axis is the time of failure (Fig. 10) (Fukuzono, 1985). Finally, Voight

(1988) derived a mathematical generalization of Fukuzono's inverse velocity method. Modern-day studies incorporate displacement velocities as the strain rate and use Fukuzono's or Voight's inverse velocity method to predict the failure time.

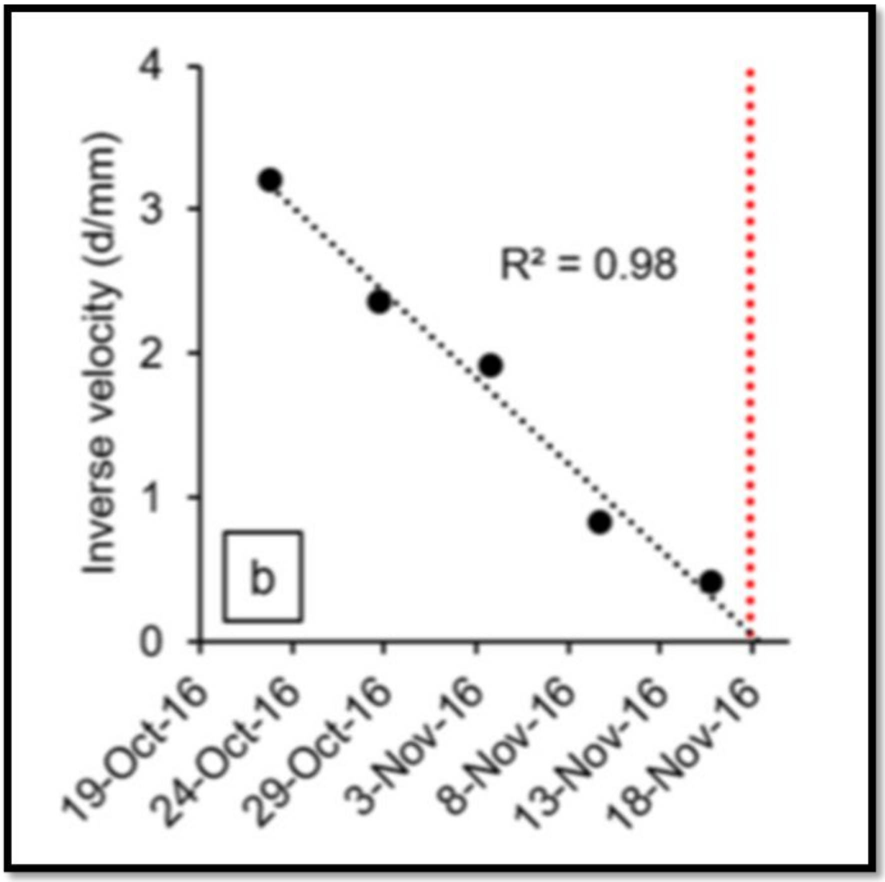

Figure 10 An example of an inverse velocity plot where time is on the x-axis and inverse velocity (day/mm) is on the y-axis. The red dashed line denotes the failure time (Carlà et al., 2019).

Not all landslides follow the creep curve model, and the velocities of different stages depend on various geological and climatic factors. While some landslides occur randomly without any measurable acceleration to plot inverse velocity, others experience secondary creep that accelerates due to seismic activity or precipitation and then slows down again (Crosta et al., 2017). The duration of a landslide and how long it stays in secondary creep are unique to the site.

The length of time a slope can be in the tertiary creep stage can range from hours to decades (Intrieri et al., 2019). This variability in landslide dynamics makes predicting the failure time specific to each site.

1.4.2 Slope failures at mining sites

The findings from the articles centered around InSAR monitoring of mining sites are consistent in their affirmation of the capability of InSAR in detecting acceleration. They also highlight the limitation of ground-based instrumentation in detecting acceleration and emphasize the necessity for increased satellite coverage. In Australia, multiple failures were studied where the ground-based systems had failed to detect the slope acceleration, but the InSAR results displayed acceleration six to eight weeks before the collapse (Carlà et al., 2018; Bar & Dixon, 2021). The Duro (2020) study showed InSAR results of acceleration and deceleration associated with heavy precipitation events before Brazil's Brumadinho tailings dam failed. Mazzanti et al. (2021) examined deformation processes at the Legnica Glogow Copper District (Poland) by Satellite InSAR and monitored slope accelerations over five years. The Mazzanti et al. (2021) study proposes a correlation between the construction of urban development above the mine site in 2014 and increased slope acceleration. Although the mentioned studies have detected acceleration, they also stated that there is currently inadequate satellite coverage with the necessary spatial and temporal resolutions to establish a reliable, automated, and rapid early warning system (Raspini et al., 2018).

1.4.3 Slope failures in nature

Most articles reviewed utilized satellite platforms such as ALOS, TerraSAR-X, and RadarSat-2 and had similar outcomes as the mining case studies (Dehls et al., 2014; Dong et al., 2018; Li et al., 2020; Schaefer et al., 2015). The studies show that InSAR can detect the acceleration before failure, and that ground-based monitors failed to detect acceleration and stress the need for more InSAR sensor-capable satellites. In addition, two of the sites showed a correlation between seismicity or precipitation as the catalyst for acceleration of the tertiary creep stage (Dini et al., 2020; Kos et al., 2016). Unfortunately, neither study performed an inverse velocity prediction plot due to the sparseness of the data.

The Sentinel-1 platform yielded results similar to those of the previously reviewed articles. Two studies incorporated the inverse velocity method and, in hindsight predicted the failure time to be three weeks before the event, which would have allowed ample time to evacuate the community's downslope (Dai et al., 2021; Intrieri et al., 2018). Other Sentinel-1 data was incorporated with seismic data and correlated slope acceleration to regional earthquake activity (Roy et al., 2022; Svennevig et al., 2020). The remaining studies examined the acceleration of slope movement by analyzing their line-of-sight geometries. The results were consistent with the data from GNSS stations and ground based InSAR, showing an error of only 2 mm. (Grebby et al., 2021; Liu et al., 2020; Mancini et al., 2021). The Squarzoni (2020) study in the Northern Apennines found that the methodology failed to detect fast-moving ground movement when the displacement velocities were >4 cm between satellite acquisitions. The Sentinel-1 studies have shown that InSAR can be effectively used as a tool for landslide forecasting, with the ability to detect movements ranging from 2 mm to 40 mm.

1.4.4 Discussion

The articles incorporated in the literature review in sections 1.4.2 and 1.4.3 on landslide prediction and InSAR produced similar findings: InSAR detection of the acceleration before the failure, ground-based monitoring failed to detect the acceleration and the lack of adequate InSAR satellite coverage. A few studies detected acceleration initiated by a seismic or a heavy precipitation event (Kos et al., 2016; Dini et al., 2020; Svennevig et al., 2020; Roy et al., 2020; Duro et al., 2021). Overall, the literature review demonstrated that InSAR data could predict the time of failure of a landslide within a month. However, satellite temporal resolution is insufficient for an effective automated early warning system (Morgan et al., 2020).

Experts suggest utilizing both InSAR results and ground-based monitoring techniques, such as GNSS campaigns and GBInSAR, along with borehole data, to achieve more accurate monitoring of slope movements (Carlà et al., 2019). The combination of ground and space-based monitoring can help determine the optimal size and location of ground-based monitoring deployments. InSAR can be used as a qualitative tool to identify areas where ground-based monitoring techniques should be deployed (Intrieri et al., 2018). However, it should be noted that in-situ and InSAR monitoring may not always be sufficient to detect acceleration, and a multi-method approach to landslide prediction is recommended (Carlà et al., 2019).

InSAR methodology has multiple limitations related to the sensor, temporal resolution, and landslide orientation. InSAR has difficulty detecting ground movement in highly vegetated areas, slushy or melting snow, and regions undergoing deformation >4 cm between satellite acquisitions. These constraints inhibit the ability of InSAR to monitor the tertiary creep continuously. If the landslide at the tertiary creep stage is snow-covered, highly vegetated, or fast-moving, InSAR will not be a viable monitoring option. Also, the satellite may not be able to acquire imagery of the landslide of interest due to the angle of the sensor not being capable of detecting north-south movement. All these considerations make the InSAR capability of detection site-specific.

A key finding from the review is that InSAR satellite temporal resolution is insufficient to predict accurate collapse time (Morgan et al., 2020). In this review, only a few case studies indicated the failure time relatively accurately, within 4-6 weeks (Dai et al., 2021; Intrieri et al., 2018). The case studies of the mining sites had a higher accuracy for the time of failure of 1-7 days (Carlà et al., 2018). There was a direct correlation between the number of images processed during the tertiary creep stage and the accuracy of the time of failure predictions (Bozzano et al., 2017). Thus, greater temporal resolution is needed to predict failures with high accuracy. Another limitation to address is associated with the back plotting of an event; it is different from accurately predicting a catastrophic failure (Duro et al., 2020). Furthermore, at this point, there has not been a catastrophic failure predicted in advance by an InSAR sensor, but the future is bright for InSAR satellites.

InSAR satellite missions such as ERS-1 and ERS-2 started in the 1990s with a temporal resolution of 35 days. Current satellites have revisit times of a few days. The future of InSAR will have even shorter revisit times with geosynchronous SAR systems with 10-metre resolution and images acquired every 8 hours (Monti et al., 2017). Soon, SAR microsatellites are expected to be launched with revisit times of 1-2 hours (Paek et al., 2020). This higher temporal resolution of the new generation of InSAR satellites allows for more data collection during the acceleration. The acquisition of more data points will improve the accuracy of predicting the failure time.

1.4.5 Conclusion

The review of the literature on landslide forecasting and InSAR showed that it is possible to back-plot a catastrophic event and forecast a time of failure. In addition, the InSAR could detect the onset of acceleration due to seismic or precipitation events. However, InSAR fails to detect fast-moving earth deformation > 4cm between acquisitions and brief time intervals of tertiary creep. Currently, the Sentinel-1 mission has a 12-day revisit temporal resolution, and this time window is only effective for landslide forecasting if the tertiary creep is over weeks or months. Landslides with only hours or days of tertiary creep before failure cannot be predicted. Only when more InSAR-capable satellites predict the failures of slopes that exhibit short tertiary creep time durations will reliable landslide forecasting be possible (Moretto et al., 2021).

The future of InSAR and landslide prediction promises short satellite repeat times (hours), giving hope for a feasible early warning system. The uncertainty of climate change and increased landslide activity in the world warrants future research concerning InSAR and landslide prediction. Today, InSAR can identify active slopes over vast terrain at low cost. InSAR imagery could be acquired and processed now to highlight regions of instability in valleys with transportation corridors, settlements, and infrastructure. Thus, utilizing InSAR can be utilized as a qualitative tool to guide where to deploy ground-based monitoring instrumentation.

1.5 Thesis Objectives

The thesis explores the feasibility of Sentinel-1 InSAR time-series displacement velocity maps as a landslide monitoring tool. The study's first part (Chapter two) examines three regions that have exhibited glacial retreat and landslide activity in the western Coastal mountains in the last 150 years: Mt Meager, Mt Cayley, and Mt Garibaldi. Multiple InSAR time series stacks were created spanning from 2017-2021 for each study area to detect slope movement. Historical landslides were used as reference points to evaluate the efficacy of the InSAR methodology. In addition, the displacement velocities were compared to bedrock geology for each site.

The second part (Chapter three) of the study focuses on the feasibility of satellite SAR imagery for monitoring and detecting precursor tertiary creep or ground deformation before a landslide event. Five sites with recent landslides were chosen for the study: Taku River, Canoe Glacier, Elliot Lake, Koidern River, and Ecstall River. Each site's InSAR time series stacks were created to include the images presiding the landslide events. The precipitation and seismicity data over a period of two weeks before the landslides were also collected. Landslides generally follow a pattern of slow creep that begins to accelerate due to precipitation, seismicity, or human activity. The InSAR will be evaluated on its ability to capture the moments of acceleration or tertiary creep.

2.0 Chapter Two: Feasibility of Sentinel-1 InSAR satellite monitoring of landslide movement in the Western Coastal Mountains of BC.

2.1 Introduction

Glacier retreat and loss are accelerating globally (Hugonnet et al., 2021). Glacier retreat destabilizes valley walls, primarily related to debuttressing bedrock slopes, leading to rockfalls, rockslides and debris flows (Cossart et al., 2008; Kos et al., 2016). In remote areas where instability occurs, large moving rock avalanches, debris flows, and outburst floods can travel far enough downslope to affect human settlement and infrastructure (Clague & O'Connor, 2021; Hermanns et al., 2004; Holm et al., 2004; Shugar et al., 2021). Thus, knowledge and understanding of high alpine slope dynamics are imperative for the safety of communities living below these potential hazards (Kilburn & Petley, 2003).

One of the areas with the highest rates of glacier loss in the world occurs in the southern Coast Mountains of Western Canada (Bevington & Menounos, 2022; Hugonnet et al., 2021). The glacial retreat makes the area subject to geomorphic and hydrological processes, with landslides being the most destructive (Friele et al., 2008). Landslide events in glaciated alpine regions such as Mt Meager, Mt Cayley, and Mt Garibaldi have left evidence of debris flows and rockslides (Bovis & Evans, 1996; Evans et al., 2001; Roberti et al., 2018). Regional monitoring of glacial recession in western Canada has been conducted with optical satellites (Landsat and Sentinel-2) (Bevington & Menounos, 2022; Bolch et al., 2010); this technique offers insight into glacial retreat but not the velocity of movement on slopes that are being debuttressed.

A remote sensing application called satellite interferometry is an increasingly popular technique for quantifying ground deformation. Satellite-based Synthetic Aperture Radar (SAR) has been used to monitor landslide deformation at local and regional scales (Cascini et al., 2010; Mateos et al., 2017; Michoud et al., 2016). The comparison of SAR images taken on separate dates shows a change in the radar phase signal for locations undergoing ground deformation. The interference caused by the phase difference in radar waves over a given time interval at a fixed location allows for creating an interferogram image, a map of ground deformation computed using InSAR. This monitoring of ground movement and displacement from space allows for large-scale monitoring of slopes in landslide-prone regions (Carlà et al., 2019; Intrieri et al., 2019; Liu et al., 2020; Grebby et al., 2021; Kim et al., 2022).

The study covered in this chapter encompasses three different regions that have exhibited glacial retreat and landslide activity in the western Coastal mountains in the last 150 years: Mt Meager, Mt Cayley, and Mt Garibaldi (Fig. 11). Multiple InSAR time series stacks were created spanning 2017 to 2021 for each study area to detect movement on the slopes. The study aims to ascertain the feasibility of InSAR as a landslide monitoring tool for the Coastal mountains of southwestern BC. In addition, the displacement velocities were compared to bedrock geology for each site.

2.2 Study Areas

2.2.1 Mt Meager

Mt. Meager (Qwe̓ lqwe̓ lústenis) located on the traditional territories of the Lil’Wat nation. Radiocarbon dating of deposits in the Mt Meager area shows evidence of debris flows dating back over 4000 years (McNeely & McCuaig, 1991). In the last century, recorded landslides occurred at Devastation Creek in 1937, 1947 and 1975 (Carter, 1932; Mokievsky-Zubok, 1977; Read, 1978) (Fig. 11). Mt Meager also had a documented rock avalanche in 1986 (Evans, 1987), and a debris flow at the Capricorn Creek region in 1998 (Bovis & Jacob, 2000). In 2010, the south flank of Mt. Meager had a landslide, the largest in Canadian history (Roberti et al., 2018), creating a large debris flow that flowed into the Lillooet Valley (Ward et al., 2020). Recently, many areas on the mountain complex have been designated as prone to landslides (Roberti et al., 2018). Mt Meager, one of the Cascade Arc volcanoes, is composed of rock from three different volcanic periods. The southern edge has remnants of an early rhyodacite episode from <1.9+/-0.2 Ma to >1.0+/-0.1 Ma, and in the north, a later rhyodacite episode have a postglacial age 0.1+/-0.02 Ma to 2340+/-50 years B.P. An extensive layer of andesite from 1.0+/-0.1 Ma to 0.5+/-0.01 Ma underlies the central and southern portions of the complex (Read, 1990).

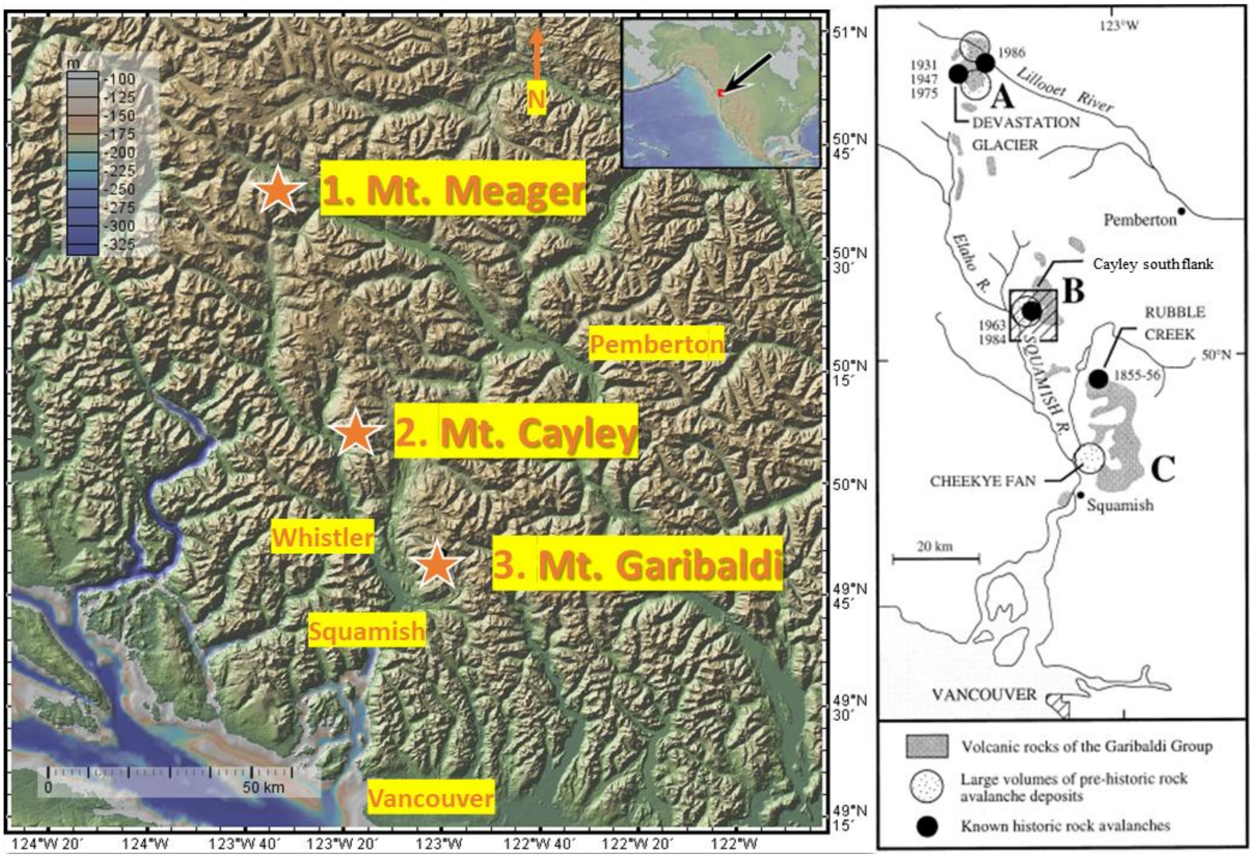

Figure 11 The study area in western Canada and the study areas highlighted in orange on the left. On the right are the historical landslides in the region (A) Mt Meager, (B) Mt Cayley, (C) Mt Garibaldi (Roberti et al., 2018).

2.2.2 Mount Cayley

Mt. Cayley is located on the traditional territories of the Squamish nation. The mountain has a history of landslides with evidence of pre-history volcanic sediments downslope of the western flank that has created the multiple fans and dams in the Squamish River (Cruden & Lu, 1992). In the last century, landslides occurred in 1963 and 1984 (Evans et al., 2001; Ward et al., 2020). The area is also part of the Garibaldi Volcanic Group, with eruptions dating between the Pliocene and the Holocene (Massey et al., 2005). The volcanic rocks overlie basement plutonic and metamorphic rocks from the Mesozoic and Tertiary Coast Plutonic Complex and range in age from 0.31 to 3.8 Ma (Green et al., 1988).

2.2.3 Mount Garibaldi

Mt. Garibaldi, another of the Cascade Arc volcanoes, is located on the traditional territories of the Squamish nation. The region is a popular recreation area with a provincial park bearing the mountain's name. On the southeast-west flank is evidence of a large landslide called the Cheekeye Fan (Evans et al., 2001) (Fig.11). Radiocarbon dating of wood collected 13 metres below the fan surface provided an age of 6,800 years BP. More recent activity occurred in 1958 when a debris flow entered the Squamish River (Jakob et al., 2005). The area is also part of the Garibaldi Volcanic Group with eruptions dating between the Pliocene and Holocene (Massey et al., 2005). The oldest volcanic rocks are pyroclastic and andesite lavas, which erupted from 1.1 to 1.3 Ma (Green, 1990). Another period of volcanic activity produced andesitic pyroclastic and laharic breccias that erupted between 670,000 and 750,000 years ago. Similar andesite and pyroclastic volcanic rocks are found on the south ridge, suggesting that volcanic activity migrated southward during this period (Green et al., 1988).

2.3 Data

Multiple time series stacks were created for analysis for each location, encompassing images during the summer months and one winter season. The images had a repeat window of 12 days, and the Single Look Complex (SLC) SAR was acquired at Vertical-Vertical (VV) polarization (Table 1). The topographic phase removal and geocoding were completed using ALOS-PALSAR imagery, creating a DEM from acquisitions between July 2011 and August 2011. The product has a pixel size of 12.5 square metres. The resulting time series from the Sentinel-1 co-registered stack has an output .csv file containing average displacement velocities and corresponding georeferenced data. The displacement measurements were converted into a shapefile with a WGS 1984 projection.

Finally, the StaMPS Visualizer tool was used to detect the movements of the ground (Hoeser, 2018; Hoeser, 2020). The tool allows the user to pick a PS, and the software creates a graph of the cumulative displacement. Finally, a shapefile of bedrock geology was overlain with a NAD 83 projection (Cui et al., 2018).

Table 1 The orbits, orientation, period, and amount of interferograms used to make the time-series stacks for the monitoring study.

Location	Orbit	Orientation	Period	# Images
Mt Meager	137	Ascending	Summer 2018-2021	23
	13	Descending	Summer 2018-2021	24
	86	Descending	Summer 2017-2021	29
	86	Descending	Summer, 2017-including Winter 2021	55
Mt Cayley	137	Ascending	Summer 2018-2021	24
	13	Descending	Summer 2018-2021	24
	86	Descending	Summer 2017-2021	35
	86	Descending	Summer, 2017-including Winter 2021	52
Mt Garibaldi	137	Ascending	Summer 2018-2021	21
	13	Descending	Summer 2018-2021	24
	86	Descending	Summer 2017-2021	31
	86	Descending	Summer, 2017-including Winter 2021	57

2.4 Processing Methodology

Creating the ground displacement time series required two sub-processing steps for satellite images of the same orbit pass. The first processing step derived relative ground displacement by measuring the phase change between all dated images and a reference image. This created multiple interferograms for each dated pair. The second sub-processing step created measured values of ground displacement at each pixel for all imaged dates by stacking and analyzing these interferograms. The two sub-processing steps were performed in different software environments: the first step used SNAP software (SNAP 2020); the second step used the Stanford Method for Persistent Scatterers (StaMPS) (Hooper et al., 2012) and Toolbox for Reducing Atmospheric InSAR Noise (TRAIN) software packages (Bekaert et al., 2015). Figure 12 outlines the workflow for the first sub-processing steps: from raw images to StaMPs-ready files. Figure 13 shows the subsequent steps to produce the final displacement map and data.

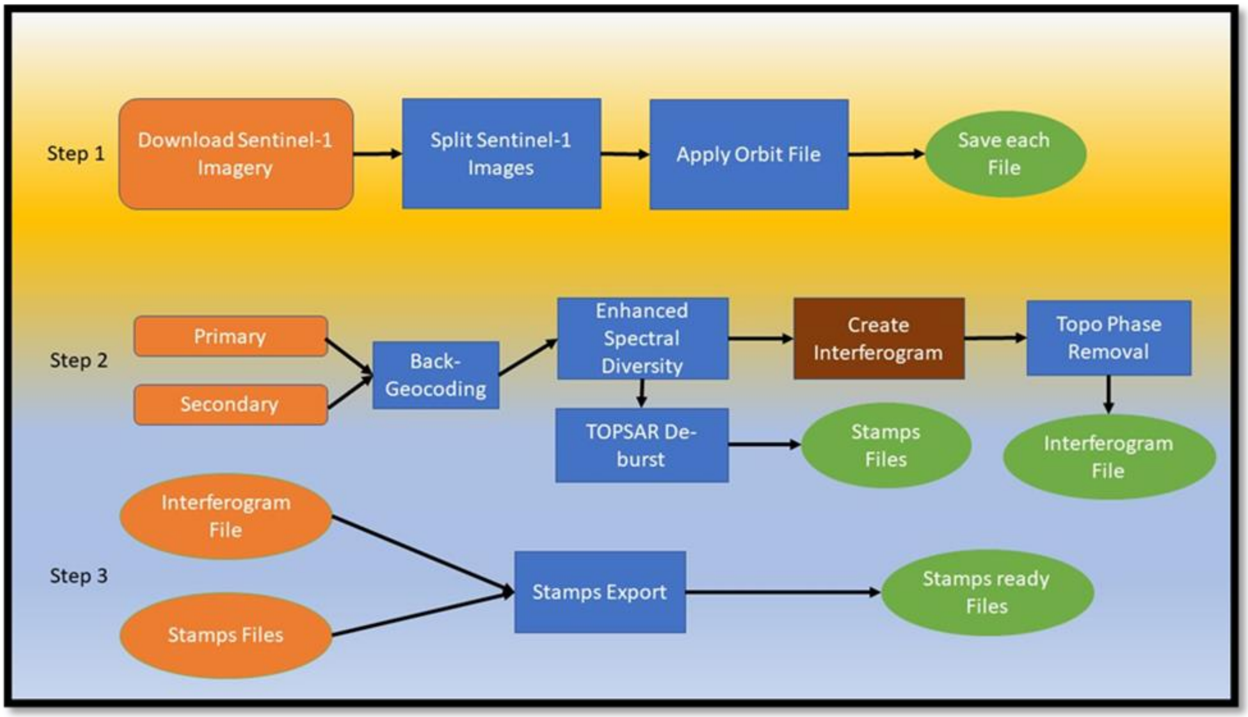

Figure 12 Differential InSAR processing flow chart within the ESA's SNAP software environment.

2.4.1 Interferogram Formation

The first sub-processing step began with spatially sub-setting all the Sentinel-1 images to the area of interest. The data are downloaded as Single Look Complex (SLC) TOPSAR data acquired in Interferometric Wide (IW) mode with VV Polarisation. After this, the accurate positions of the satellite during the image acquisition were applied using updated, precise orbit files. These ensured that images from multiple dates were optimally aligned (co-registered). Before images could be compared for phase differences, an optimal primary image was selected by analyzing the perpendicular and temporal differences between all the images. The image with the smallest temporal and perpendicular baselines became the ‘reference’ image. Interferograms were created by comparing this image with all other dated ‘secondary’ images.

Co-registration of each image pair followed, using back-geocoding co-registration with enhanced spectral diversity. An ALOS PALSAR digital elevation model, created from acquisitions between May and August 2011, assisted in the back-geocoding of the images. Images were additionally de-bursted to remove the dark bars between the acquisition bursts (cf. Yague-Martinez et al., 2016). Interferograms were then created by comparing the difference in phase signal between the two dates. The effect of topography was subsequently removed by applying the ALOS PALSAR digital elevation model. The resulting interferograms were stacked as a single file and then formatted for StaMPS software in preparation for the second sub-processing step (Fig. 13).

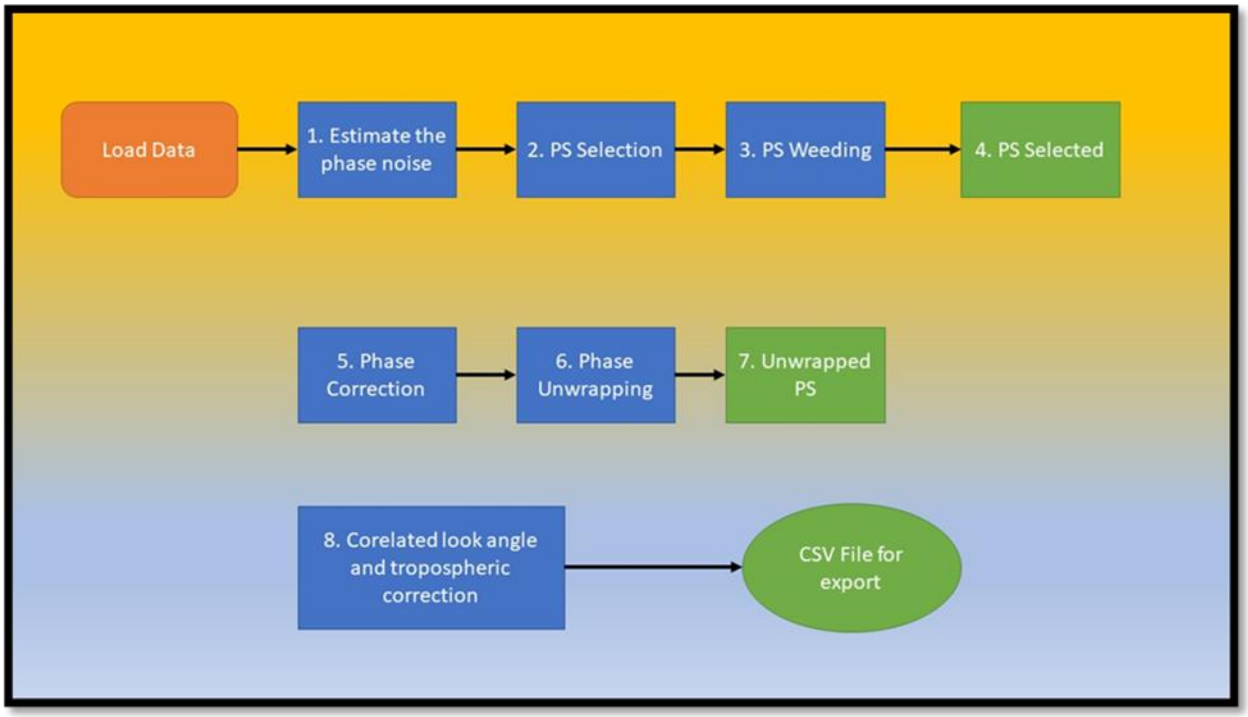

Figure 13 PSI processing chain with the StaMPS software package.

2.4.2 Interferogram Unwrapping

Persistent Scatterer (PS) Analysis isolated pixels that express a consistent backscatter signal across an interferogram stack, hence the term. This method also removed noise primarily caused by satellite orbital differences and changes in the atmosphere between acquisition dates. The remaining differences due to phase change were converted to satellite (LOS) measurements in metres (termed unwrapping). StaMPS software was selected to handle the PS Analysis because of its documented capability for determining surface displacement in areas that exhibit non-steady deformation (Intrieri et al., 2018; Raspini et al., 2018; Carlà et al., 2019). It allowed PS to be queried for their deformation throughout the acquisition time series.

2.4.3 Persistent Scattering

An eight-step procedure, outlined in the StaMPS/MTI manual (Hooper et al., 2012), was used to perform the processing (Figure 13). An initial bash script run in a Linux environment loaded all interferograms in the time series. These multiple steps were conducted in patches across all interferograms and the entire scene. The merged single stack was then unwrapped to convert the interferograms, measured in radians, into deformation in millimetres. The first step in the eight-step process was estimating phase noise for each candidate pixel in each interferogram. PS were then selected by evaluating phase noise characteristics and accounting for the number of non-PS pixels in a scene. Pixels with noise attributed to neighbouring ground resolution elements were eliminated. The remaining selected pixels were phase-corrected for spatially uncorrected look-angle errors, and patches were merged. The phase was unwrapped, and then the DEM, atmosphere, and orbit errors were removed. Atmospheric correction was performed using the TRAIN software package devoted to the atmospheric correction of interferometric products (Baekaert et al., 2015). An ALOS-PALSAR DEM provided a substantial topographic base for terrain correction to the SAR images. Multiple methods to apply an atmosphere correction were available; this study employed a linear method.

2.4.4 StaMPS Parameters

The StaMPS software is readily available for use, with reasonable preset values. However, specific parameters have the potential to affect the quality of the results obtained. To ensure optimal outcomes, it is highly recommended to execute StaMPS one step at a time and to explore the effects of adjusting specific parameters. For this study I redefined some of the default parameters to detect and monitor landslides. The first alteration was to initiate phase ramp estimation for each interferogram. The estimated ramp will be subtracted before unwrapping, which helps identify local signals, such as landslides over a larger area (Hoeser, 2018). Additionally, the maximum topographic error was reduced from the recommended 20 metres by Lazecky (2016) and Hooper (2008) to only 10 metres.

The default standard deviation threshold of 1.0 was deemed too high, causing many PS to be left in waterbodies and ice. As a solution, it was lowered to 0.8. This threshold is calculated for each pixel based on the phase noise standard deviation of all pixel pairs, including the pixel. The PS is dropped if a pixel's minimum standard deviation exceeds the threshold. The filter grid size was also reduced from 50 to 40 metres to further improve accuracy. Before filtering, candidate pixels are resampled to a grid with this spacing to determine the spatially correlated phase. These adjustments were based on research conducted by Hooper et al. (2007; 2012).

I adjusted the default settings in the unwrapping step based on the recommendations of other landslide studies that used the StaMPS software (Hooper et al., 2008; Lazecky et al., 2016; Hoeser, 2018). I reduced the unwrapping grid size from 200 to 100 metres and decreased the unwrapping Goldstein filtering window from 32 (default) to 8. These changes will help detect PS in local areas like landslides. I shortened the unwrapping time window from 730 to 50 days to smooth the estimated phase noise using a Gaussian window with a standard deviation (Hooper et al., 2008).

The parameters were changed based on landslide detection and monitoring criteria. The setting for the maximum gamma threshold of 0.005 was not satisfied with the default setting of 3 maximum iterations. I set the number of iterations to 10 based on examining the datasets individually; it was determined that the stacks could take 5-8 iterations to reach the maximum gamma threshold of 0.005. Finally, the number of cores used was changed from the default of 1 to 16. Below is a table outlining the StaMPS processing parameters utilized here.

Table 2 List of StaMPS parameters used in this research. The Default and the Used values are given with a rationale for the deviation.

Parameter	StaMPS Step	Default	Used	Rationale
“no_cores”	1	1	16	Processing
“Max_topo_size”	2	20 m	10 m	Quality
“filter_grid_size”	2	50	40	Quality
“Gamma_max_iterations	3	3	10	Quality
“Weed_standard_dev”	4	1	0.8	Quality
“Unwrap_grid_size”	6	200	100	Landslide detection
“Unwrap_gold_n_win”	6	32	8	Landslide detection
“Unwrap_time_win”	6	730 d	50 d	Landslide detection
“Scla_deramp”	7	‘n’	‘y’	Landslide detection
“Subtr_tropo”	8	“n”	‘y’	Atmospheric correction

2.5 Displacement Results

The LOS measurements were calculated using a best fit line over the entire time series using linear regression. The points are individually weighted based on their standard deviation from the line, with smaller weights applied to the points farther from the line and larger weights applied to points closer to the line. The resulting averaged and weighted velocities were used to analyze the different surficial geology types in the study area. The LOS values range from positive to negative with the positive values measuring the distance towards the satellite and negative as the distance away from the satellite. For the purposes of this study negative values denote a increase in and positive denotes an decrease in range direction.

Each location had a unique statistical fingerprint based on the number of interferograms, years, and geographical location. Thus, each orbit's classification system is based on the standard deviation of that orbit. All the orbits had means close to zero but different SDs. The displacement velocities were classified as high increase or decrease in range direction greater than plus/minus 3 SD, and moderate increase or decrease in range direction was between plus/minus 3 SD and 2 SD. Stable regions were classified as everything between plus/minus 2 SD (Tab. 4). Other studies have used this approach to quantify the general error in displacement velocities (Short et al., 2011; Wolfe et al., 2014). In the following maps I removed the stable PS, leaving only the PS deemed in motion by the above SD classification.

Table 3 The classification system used to compare the velocity displacements.

Displacement velocity range (mm/year)	Classification
Greater than 3 SD	High decrease
Between 3 SD and 2 SD	Moderate decrease
Between -2 SD and 2 SD	Stable
Between -2 SD and -3 SD	Moderate increase
Less than -3 SD	High increase

2.5.1 Mount Meager

The displacement results for Mount Meager from 2018-2021 illustrate areas of a high increase in range direction on the north and south flanks in orbits 13, 137, and 86. The highlighted areas of high increase in range direction correspond to areas adjacent to the Plinth and Devastation Peak landslide areas. In orbit 13, on the slope across from Plinth Peak there is a significant decrease in range direction demonstrating that both slopes of that valley are moving. All the orbits display no PS with high increase or decrease in range direction in the 2010 slide area. The winter results from this study detected fewer PS than the snow free summer stacks. The low detection of PS during the winter months is expected as InSAR cannot penetrate deep or wet snow (Carlà et al., 2019).

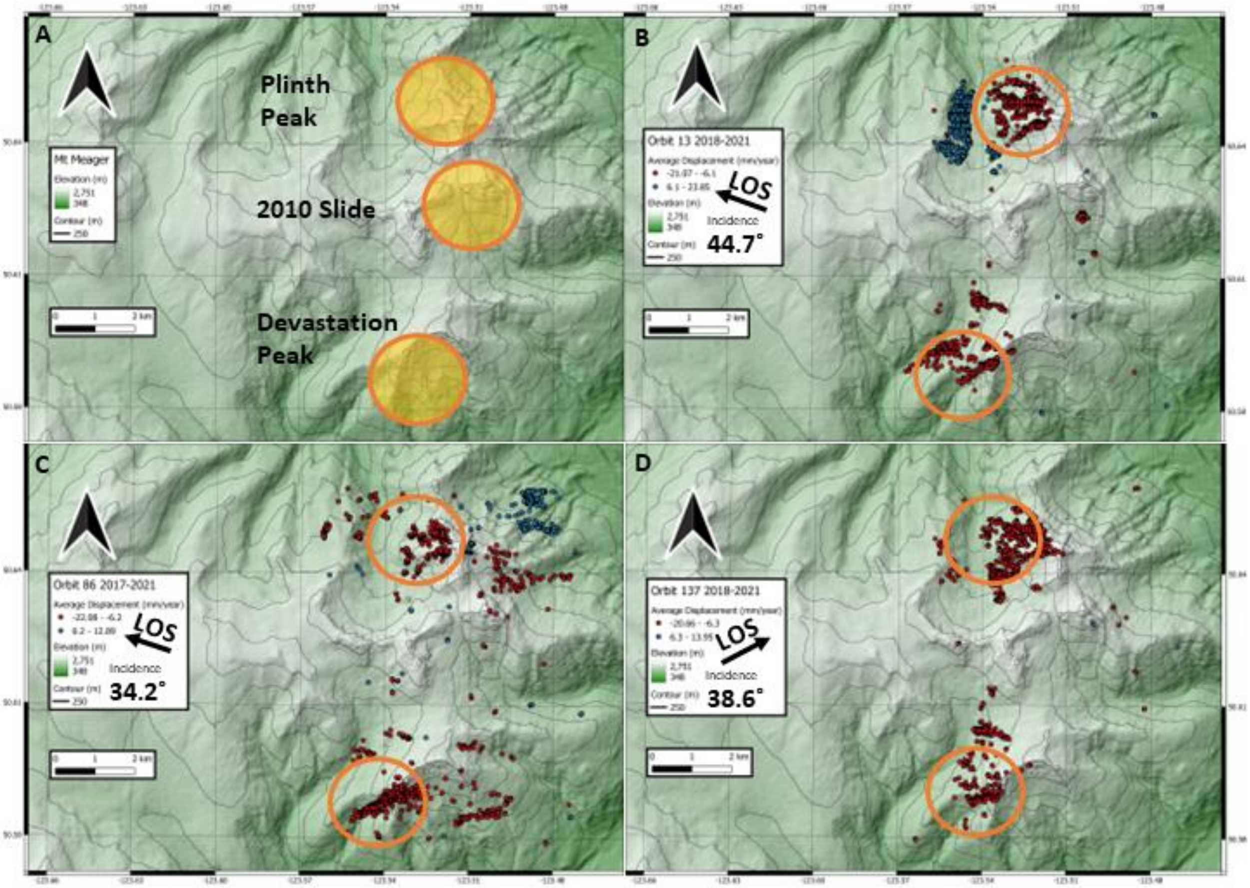

Figure 14 The orange circles highlight areas of significant LOS velocities for Mt Meager. The red dot represents an increase in range direction and blue as a decrease. A. Yellow circles show historical landslide activity, B. results from orbit 13, C. results from orbit 86, and D. results from orbit 137.

2.5.2 Mount Cayley

The InSAR displacement results detected movement on the southern slopes of Mt Cayley between 2018-2021. In the historical landslide areas, there were few PS displaying significant movement. However, there was an decrease in range direction detected north of the slide areas in orbits 13 and 86 (Fig. 15). On the southeast corner of the map there is an area of increase in range direction found in orbits 13,86 and 137. The winter results are not shown due to the spareness of data produced.

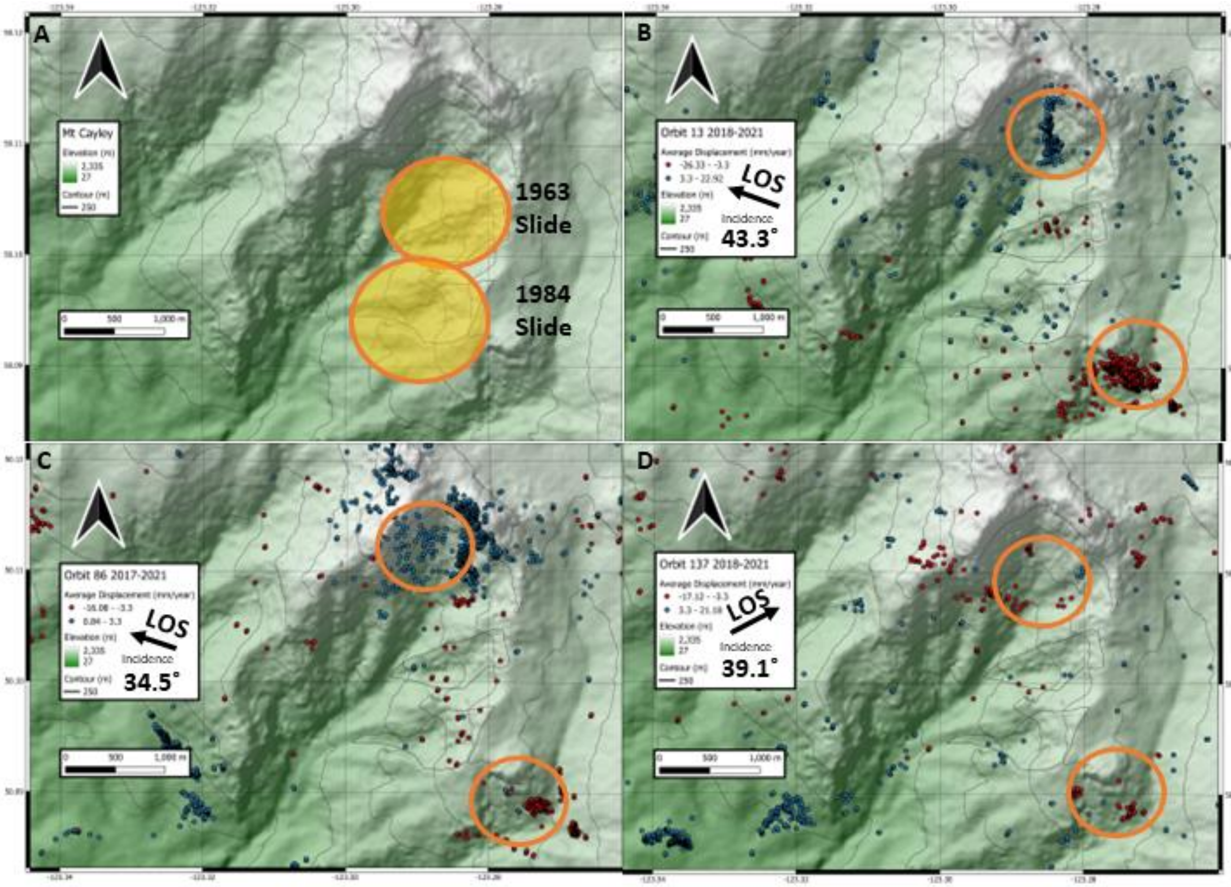

Figure 15 The orange circles highlight areas of significant LOS velocities for Mt Cayley. The red dot represents an increase in range direction and blue as a decrease. A. Yellow circles show historical landslide activity, B. results from orbit 13, C. results from orbit 86, and D. results from orbit 137.

2.5.3 Mount Garibaldi

The InSAR results detected movement on the slopes of Mt Garibaldi from 2018-2021, with movement detected in the Cheekye slide area for orbits 13 and 137, while the results from orbit 86 are notably sparser and have a dispersed pattern (Fig. 16). On the slopes northwest of the Cheekye slide area there are clusters of PS with movement away from the satellite in orbit 137. Finally, the Mt Garibaldi winter results have not been displayed due to the poor quality of the results.

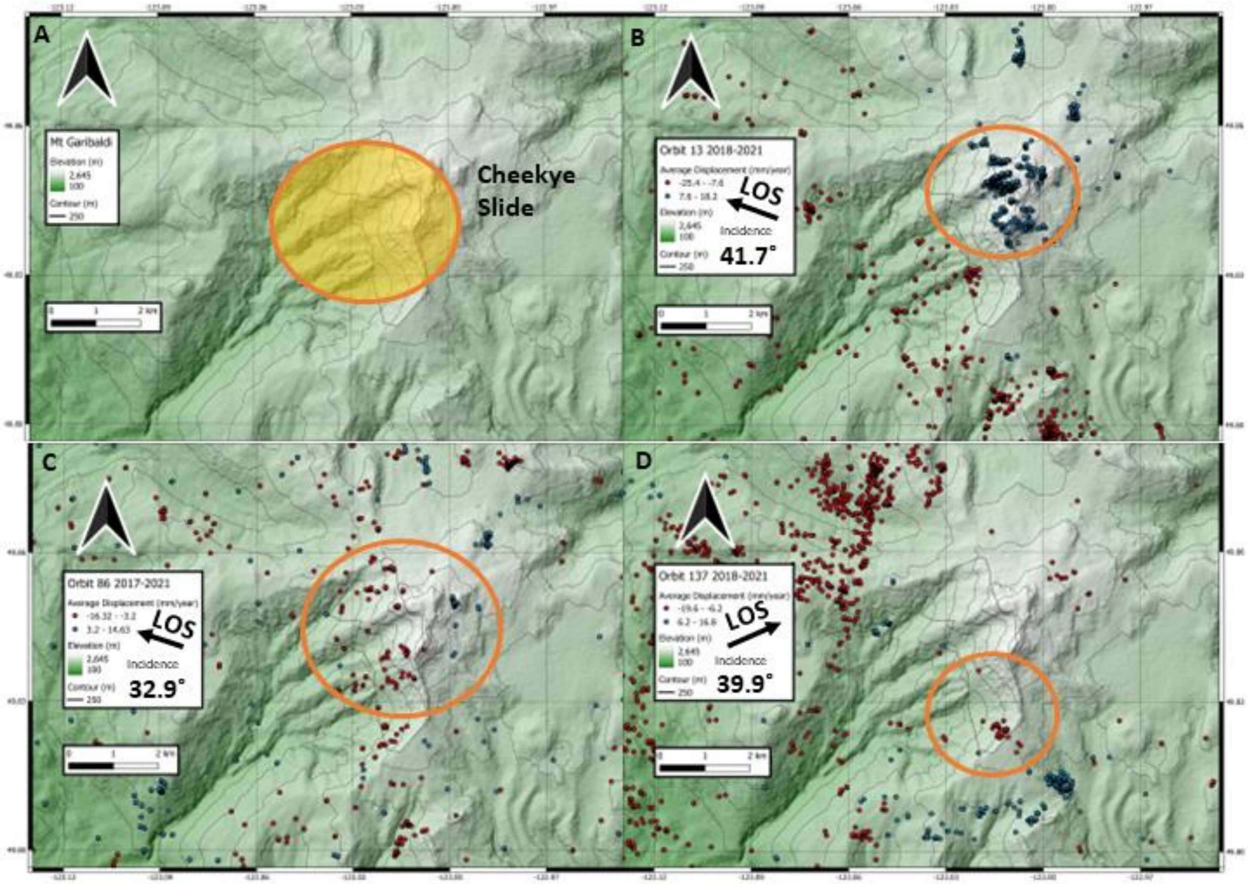

Figure 16 The orange circles highlight areas of significant LOS velocities for Mt Garibaldi. The red dot represents an increase in range direction and blue as a decrease. A. Yellow circles show historical landslide activity, B. results from orbit 13, C. results from orbit 86, and D. results from orbit 137.

2.6 Bedrock Geology

The displacement velocities from orbit 86 were used for the bedrock geology evaluation. Orbit 86 was chosen because it had five years of prolonged temporal coverage and the most significant number of interferograms. The bedrock units used in the study are volcanic, sedimentary, and intrusive (Cui et al., 2018). Each bedrock geology's displacement velocities were classified based on the SD of each location. Examining the percent stable results of each bedrock unit compared to the entire sample will highlight nuances of instability. Finally, the PS distribution per bedrock unit was calculated and analyzed.

2.6.1 Mount Meager

Most of the PS were detected in the volcanic unit at 60%, followed by the intrusive units at 38% and the sedimentary units with the remaining 2%. Figure 14 shows that the sedimentary units have least amount of area in the image corresponding to the low PS detection percentage. The entire sample had a percent stable value of 94.6%, with the intrusive units exhibiting the highest percent stable of 97.6%. The volcanic units had a percent stable of 90.7%, and the sedimentary units had the lowest percentage with 82.8%. The sedimentary units showed the highest percentage of total decrease in range direction of 15.9%, and the volcanic units had the highest total increase in range direction percentage of 8.7% (Table 4).

Table 4 Percent results of the stable classification of Mt Meager for each bedrock geology unit.

Classification	All	Volcanic	Sedimentary	Intrusive
Stable (%)	94.6	90.7	82.8	97.6
High decrease (%)	0.1	0.1	0.4	0
Moderate decrease (%)	1.0	0.7	15.5	0.8
Moderate increase (%)	4.4	6.5	1.1	1.3
High increase (%)	1.4	2.2	0.2	0.4

2.6.2 Mount Cayley

Most of the PS were detected in the intrusive unit at 75%, followed by the volcanic units at 20% and the sedimentary units with the remaining 5%. Like Mt Meager the sedimentary units are a small portion of the study area which corresponds to the low PS density. The entire sample had a percent stable value of 96.8%, with the sedimentary units exhibiting the highest percent stable of 99.6%. The volcanic units had a percent stable of 97.2%, and the intrusive units had the lowest percentage with 96.1%. The intrusive units showed the highest percentage of decrease in range direction with 2.4%, and the volcanic units had the highest increase in range direction at 2.4% (Table 5).

Table 5 Percent results of the stable classification of Mt Cayley for each bedrock geology unit.

Classification	All	Volcanic	Sedimentary	Intrusive
Stable (%)	96.8	97.2	99.6	96.1
High decrease (%)	1.8	0.1	0	1.7
Moderate decrease (%)	0.6	0.3	0.2	0.7
Moderate increase (%)	1.1	1.3	0.1	1.1
High increase (%)	0.5	1.1	0.1	0.4

2.6.3 Mount Garibaldi

Most of the PS were detected in the intrusive unit at 63%, followed by the volcanic units at 24% and the sedimentary units with the remaining 13%. The area of the sedimentary units on Mt Garibaldi is considerably larger than Mt Meager and Mt Cayley and as such exhibit a higher PS density. The entire sample had a percent stable of 96.8%, with the volcanic and intrusive units exhibiting the highest percent stable value of 98.7%. The sedimentary units had the lowest percentage, with 97.7%. The intrusive units showed the highest percentage of an decrease in range direction with 0.6%, and the sedimentary units had the highest total increase in range direction percentage of 1.7% (Table 6).

Table 6 Percent results of the stable classification of Mt Garibaldi for each bedrock geology unit.

Classification	All	Volcanic	Sedimentary	Intrusive
Stable (%)	96.8	98.7	97.7	98.7
High decrease (%)	0.4	0.1	0.1	0.2
Moderate decrease (%)	1.0	0.2	0.4	0.4
Moderate increase (%)	2.2	0.8	1.5	0.6
High increase (%)	0.8	0.2	0.2	0.2

2.7 Discussion

This study aimed to determine whether InSAR technology could be used to monitor landslide-prone regions in the GVC in western Canada. The InSAR successfully detected movement at all three study sites, but fewer PS were detected during winter due to the sensor's inability to penetrate snow and ice. Most PS identified showed little to no movement or were classified as stable. The areas with movement corresponded to regions with a history of landslide activity. Ultimately, a map marked extreme movement areas, highlighting regions with significant increase and decrease in range direction. However, the results had detection gaps, possibly due to vegetation, snow, or the ground moving too quickly for the method to detect.

The study evaluated the InSAR technique's feasibility with the Sentinel-1 by accessibility, cost, validity, and monitoring capability. Fortunately, the Sentinel-1 data are free, and the LOS measurement software tools are also open-source and free. DeGlado (2019) developed automated methods, and Hoeser (2020) provided further documentation to facilitate the computerized interferogram stack formation. The van der Kooij (2002) and Roberti (2018) studies used the DInSAR technique to measure deformation on the slopes of Mt Meager. They yielded results of ~1-2 cm/year of deformation on the Plinth and Devastation peaks, similar to our findings of 5-20 mm/year, providing validity to this study’s displacement velocities. We detected movement on the slopes known to be moving in the past, indicating that this methodology could be used to monitor slow acceleration rates and/or persistent creep, but not fast-moving slopes.

As per Roberti's (2018) research, the Sentinel-1 InSAR technique can effectively track gradual accelerations. The 2010 Mount Meager failure was not triggered by a single event but by multiple destabilizing factors, including prolonged high temperatures during summer, and pre-existing failures at the slope's base in the years preceding the landslide (Roberti et al., 2018). The study's findings indicate that InSAR can monitor the slow-moving acceleration due to the cumulation of multiple factors leading to landslide activity.

2.7.1 Displacement Velocities

Many displacement velocity results were stable in the study area, due to the SD methodology used for classification. This methodology determined that 95% of all velocities were near-zero. The high number of PS classified as stable supports the use of InSAR for long-term monitoring of remote slopes potentially susceptible to landslides. InSAR's ability to detect sub-centimetre movement allows for temporal analysis of ground displacement in the past and future. Areas that show changes in displacement velocity are suggested to undergo further examination to identify any acceleration in ground movement using terrestrial monitoring methods. This information could inform local governments, businesses, and communities of potential landslide risks.

These sites were chosen based on their previous history of landslides, as demonstrated in Figure 11. The InSAR results showed movement in the areas surrounding past landslide activity in all three locations. This confirms that the Sentinel-1 data can identify and measure LOS displacement on the dynamic mountain slopes in the western Canadian Cordillera. Additionally, the Sentinel-1 data enabled a comprehensive analysis of the summer movement, revealing whether the ground surface was accelerating or moving at a consistent velocity over time. A year-round monitoring program would require sufficient high-quality data for maximum effectiveness.

2.7.2 Winter Displacement Velocities

Snow thickness and moisture content can pose problems and affect results when conducting InSAR studies in high alpine environments. Many studies exclude winter images due to their low coherence and decorrelation to mitigate these issues. However, despite these limitations, our study obtained winter results from all three orbits. The findings of the Carlà (2019) study also suggest that while wet snow can negatively impact correlation, InSAR Radar can penetrate dry, cold snow up to approximately 20 metres. It is important to note that the quality of winter InSAR results may vary depending on the elevation of the site and its impact on the level of snow moisture content.

To monitor landslide-prone slopes in real time, it is crucial to detect any acceleration in ground movement before failure occurs (Carlà et al., 2019). However, during winter months, the presence of snow can make it more difficult to capture movement using this methodology accurately. Despite this challenge, the winter results still managed to identify areas of movement, albeit with a lower quantity of PS. To achieve reliable results throughout the year, an InSAR system for year-round monitoring would need to consider factors such as weather, elevation, and moisture content of the snow.

2.7.3 Bedrock Geology

The outcomes of the bedrock geology study varied depending on the location. To compare the different areas, the percentage stability of each bedrock unit was compared to the overall stability of the sample. The hypothesis was that the volcanic units would show more significant variation than the intrusive units. Results from Mt. Meager and Mt. Cayley indicated that the volcanic units had a higher total percentage of decrease in range direction than the intrusive units. However, the bedrock geology results from Mt. Garibaldi did not exhibit the same decrease in range direction trend associated with the volcanic units observed at Mt. Meager and Mt. Cayley. Additionally, Mt. Meager displayed the highest instability among the three volcanic areas.

InSAR results indicate that a site's stability is correlated with the frequency of landslide events. The most recent landslide activity occurred in 2010 on Mt Meager, while Mt Cayley experienced its last event in 1984. Mt Garibaldi has not seen any activity since 1958, according to Evans (2001). The percent stability calculated for Mt Meager was 94.6%, lower than the 96.8% calculated for Mt Cayley and Garibaldi. Additionally, the volcanic units at Mt Cayley showed less stability than those at Mt Garibaldi. Mt Meager had the highest percentage of volcanic units among the three sites at 60%, indicating that it is more prone to instability than Mt Cayley and Mt Garibaldi. The instability of Mt Meager can be attributed to the volcanic activity beneath the volcano, as Allstadt (2013) and Roberti (2018) reported.

The instability on Mt. Meager is also influenced by the hydrothermal alteration of the slopes and the fractured volcanic structure. The intrusive rhyodacite plug at the peak is surrounded by ochre-coloured hydrothermal alteration, while the lower slopes display block and ash evidence of volcanic activity. Read (1978) reports that the lower parts of the slope also show signs of hydrothermal alteration. This activity has caused the volcanic breccias around the peak to fracture, rendering the environment more vulnerable to landslides due to increased water infiltration, weathering, erosion, and frost heave processes (Roberti et al., 2018).

This assessment examined the rock types at only three locations, a small component of the overall geological scenario. Additional factors like fracture density and orientation, proximity to faults, presence of surface water and melting, and slope gradient should also be considered to comprehend the geological mechanisms involved fully. The findings indicate that the LOS displacement velocities show varying stability patterns based on the type of rock present.

Additionally, it is difficult to accurately determine the physical processes that lead to observations of an increase or decrease in range direction. The measurements taken in the LOS are influenced by the satellite's angle and the slope's aspect and orientation. Thus, steep mountain topography might show opposite trends dependent on the orbit’s angle to the landslide area. Due to these factors, it is essential to thoroughly analyze the results and LOS geometries before making any conclusions about the InSAR results.

2.7.4 Feasibility of Monitoring with Sentinel-1

Using Sentinel-1 InSAR findings to keep track of landslides in the western Canadian Coast mountains during certain seasons is possible. However, the outcomes from the winter stacks were not enough to create a reliable year-round monitoring system. Detecting the acceleration onset before a landslide occurs is essential to warn people of potential danger. When InSAR produces unsatisfactory results from winter acquisitions, detecting the precursor acceleration through InSAR becomes impossible. The snow-free satellite images detected both areas of movement and stability. Thus, the InSAR technique can identify unstable areas from space, which can guide geotechnical surveys on the ground. Finally, the study's results can serve as a reference point for future InSAR research to observe changes in stability.

2.8 Conclusion

The study aimed to determine if Sentinel-1 InSAR data could be used to detect precursor ground movement-associated landslides. The InSAR results showed that ground displacement occurred on the slopes of all three study sites, which corresponded with slopes that had previous landslide activity. However, the InSAR results collected during winter months were less detailed and frequent than those collected through a seasonal approach. While a year-round monitoring system is possible with Sentinel-1 data, there may be gaps in data coverage due to snow conditions and site topography. The volcanic units showed more instability than the intrusive bedrock units, except for Mt Garibaldi. Ultimately, the study generated baseline maps of all three mountains' displacements for 2017-2021.

3.0 Chapter Three: InSAR satellite time series imagery and detection of precursor landslide movements in western Canada.

3.1 Introduction

“We demand rigidly defined areas of doubt and uncertainty!” (Adams, 1979, p.115)

The quote above is steeped in irony and satire and encapsulates the challenges that British Columbians who reside in steep mountain valleys and slopes face for the future. Recent atmospheric river events triggered multiple landslides in southwestern BC and have generated uncertainty concerning potential geo-hazards. Landslides are geological hazards that significantly threaten human life, infrastructure, and biotic habitat in areas with steep slopes (Cloutier et al., 2017). Precursory signs of a landslide can be detected, making the evacuation of residents likely. Thus, forecasting and early warning systems of slope movement are needed for the safety of communities living in the valleys below (Kilburn & Petley, 2003).

Landslides are challenging to predict due to trends of non-linear displacement and stochastic factors such as seasonal precipitation, seismicity, and topographical complexity. The preconditioning of a landslide unfolds over thousands of years due to cumulative geological factors (e.g., seismicity, rock type, glacial processes) and climatic factors (e.g., temperature and precipitation) (Crosta et al., 2017). The ongoing climatic and geological cycles imposed on regions susceptible to landslides may exhibit long-term ground deformation superimposed with episodic accelerations due to triggers like seismicity or precipitation (Cappa et al., 2004). Landslide prediction aims to understand the structural dynamics of the slide accelerations to estimate when there will be a catastrophic failure (Intrieri et al., 2019).

A remote sensing application called satellite interferometry is an emerging technique for quantifying ground deformation. Satellite-based synthetic aperture radar (SAR) has successfully monitored landslide deformation at local and regional scales (Cascini et al., 2010; Mateos et al., 2017; Michoud et al., 2016). The comparison of SAR images taken on separate dates shows a change in the radar phase signal for locations undergoing ground deformation. The interference caused by the phase change between 2 SAR images is captured by creating an interferogram image, which can be used to make precise measurements of ground deformation, using a method referred to as Interferometric Synthetic Aperture Radar (InSAR).

The study covered in this chapter focuses on the feasibility of satellite SAR imagery for monitoring and detecting precursor tertiary creep or ground deformation before a landslide event. Five sites with recent landslides were chosen for the study: Taku River, Canoe Glacier, Elliot Lake, Koidern River, and Ecstall River (Fig. 17). Each site's InSAR time series stacks were created to include the images before the landslide events. The precipitation and seismicity data in the two-week period before the landslides were also collected. Landslides generally follow a pattern of slow creep that begins to accelerate due to precipitation or seismicity. The InSAR method will be evaluated on its ability to capture the moments of acceleration or tertiary creep.

3.2 Study Areas

All the sites are located on the Coast Mountains of Canada in a mountainous area called the western Cordillera. A chain of mountains stretching from Alaska to Washington, encompasses the entire coast of BC (Fig. 17). Glaciers are abundant in the region, with all the study sites having a glacier adjacent to the slide, apart from the Koidern River slide. All the areas have had landslides since 2019, making them good candidates for accessing sufficient Sentinel-1 data to test the feasibility of precursor detection. In addition, all the sites had seismic waveform data pinpointing the date and time of the landslide event.

3.2.1 Koidern River

On December 20, 2019, a landslide and debris flow occurred in the traditional territory of the Kluane First Nation on the Koidern River in the Yukon (Fig. 17). It was a rock avalanche with a high velocity that scoured downslope, damming the Koidern river in the valley floor with landslide debris (Petley, 2020a).

3.2.2 Taku River

On December 24, 2020, a landslide and debris flow occurred in the traditional territory of the Taku River Tlingit First Nation on the Taku River, located in the northern Coast Mountains of British Columbia (Fig. 17). The slide was the result of a significant rock slope failure, with a substantial mass detaching from high on the slope. This mass then triggered the collapse of the face of the slope below. The mass was in free fall for a considerable distance – on impact with the valley floor, it instantaneously fragmented to create an avalanche with a long run out and substantial dispersion (Petley, 2020b; Stewart-Jones & Gruber, 2023).

3.2.3 Canoe Glacier

On July 1, 2021, a landslide and debris flow occurred in the traditional territory of the Nisaga First Nation on the Canoe Glacier, located in the northern Coast Mountains of British Columbia (Fig. 17). At the height of the record warming event known as the “heat dome,” about five million tonnes of rock and ice fell from the Canoe Glacier. The debris had a massive runout, missing a mine site 6 kilometres away with 600 hundred workers (Pollon, 2021).

3.2.4 Ecstall River

On September 1, 2022, a landslide and debris flow occurred in the traditional territory of the Tsimshian First Nation on the Ecstall River, located in the northern Coast Mountains of British Columbia (Fig. 17). The landslide appears to have started as a failure on a near-vertical rockface, and then to have transitioned into a classic ice/rock avalanche—the slide deposited rock into a lake, creating a tsunami and outburst flood downstream (Petley, 2022).

3.2.5 Elliot Lake

On November 28, 2020, a landslide, tsunami, and outburst flood occurred within the traditional territory of the Homalco First Nation in the headwaters of Bute Inlet, located in the southern Coast Mountains of British Columbia (Fig. 17). The landslide deposited debris into a glacier lake that displaced water sending a tsunami and outburst flood scouring the stream to the ocean (Geertsema et al., 2021).

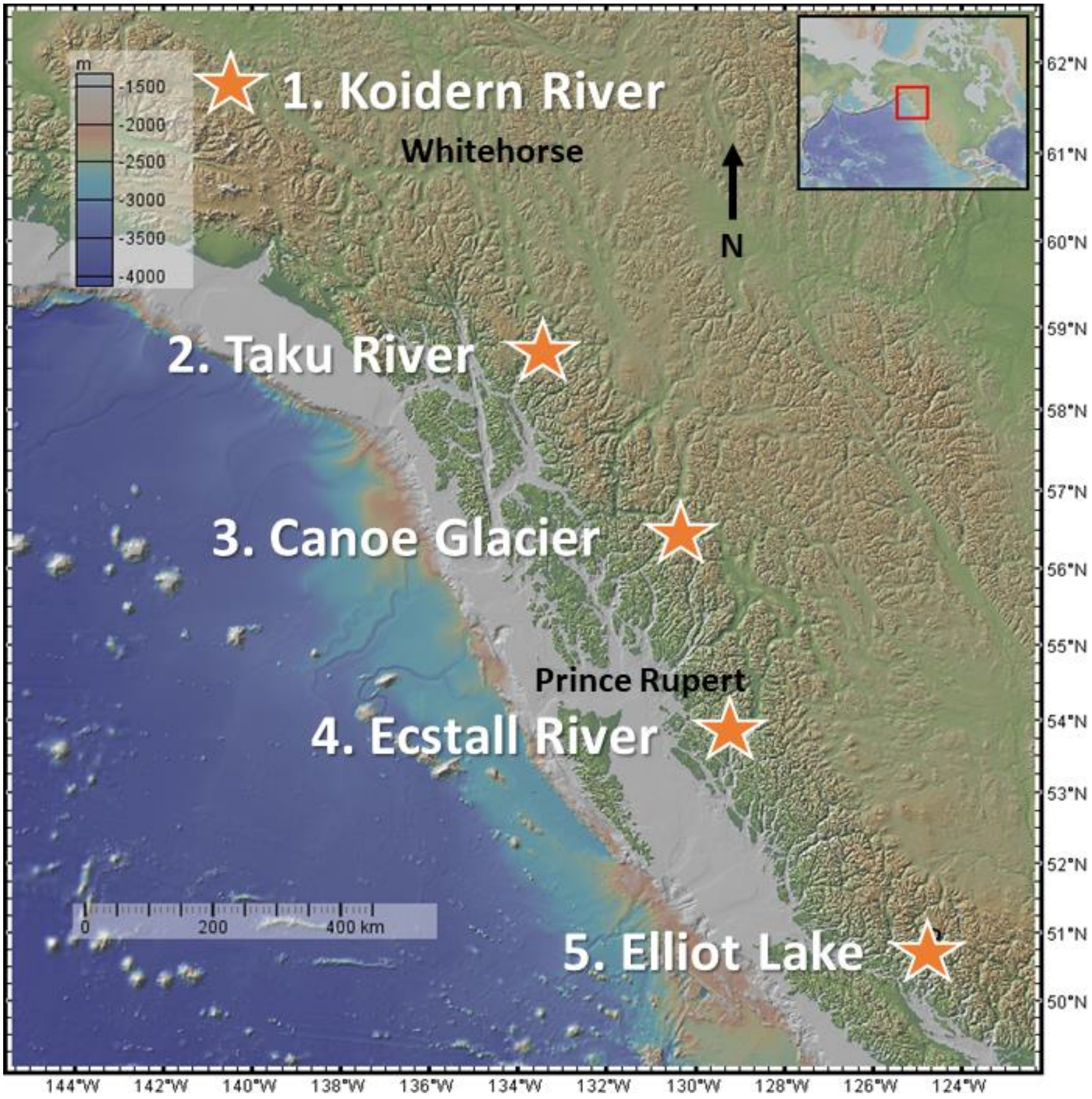

Figure 17 The study sites and their relation to North America.

3.3 Data

Multiple time series stacks were created for analysis for each location, encompassing summer images, and winter images before the failure. The images had a repeat window of 12 days, and the Single Look Complex (SLC) SAR data were acquired at Vertical-Vertical (VV) polarization

(Table 7). The topographic phase removal and geocoding were completed using ALOS-PALSAR imagery, creating a DEM from acquisitions between July 2011 and August 2011. The product has a pixel size of 12.5 square metres. The resulting time series from the Sentinel-1 co-registered stack has an output .csv file containing average displacement velocities and corresponding georeferenced data. The displacement measurements were converted into a shapefile with a WGS 1984 projection.

Table 7 The orbits, orientation, period, and amount of interferograms used to make the time-series stacks for the forecasting study.

Location	Orbit	Orientation	Period	# Images
Koidern River	116	Descending	Summer 2016-2019	19
	116	Descending	Summer 2016-December 2019	26
	123	Ascending	Summer 2017-2019	14
	123	Ascending	Summer 2017-December 2019	18
Taku River	101	Descending	Summer 2017-2020	34
	101	Descending	Summer 2017-December 2019	40
	174	Descending	Summer 2017-2020	31
	174	Descending	Summer 2017-December 2019	37
Canoe Glacier	108	Ascending	Summer 2018-2021	27
	28	Descending	Summer 2018-2021	34
Ecstall River	6	Descending	Summer 2018-2022	28
	108	Ascending	Summer 2018-September 2021	31
Elliot Lake	86	Descending	Summer 2017-2020	26
	86	Descending	Summer 2018-November 2020	32
	137	Ascending	Summer 2017-2020	20
	159	Descending	Summer 2017-2020	26

3.3.1 Supplementary Data

Two weeks of weather and seismic data were collected before each landslide event from the Government of Canada. The historical weather records website contained the total precipitation and average temperature values (Government of Canada, 2023). Seismic data were collected from the waveform archive (Earthquake Database), only picking records within 50 km and greater than 2 ML (Government of Canada, 2023). Finally, the StaMPS Visualizer tool was used to detect the movements of the ground just before catastrophic failure (Hoeser, 2018; 2020). The tool allows the user to pick a PS, and the software creates a graph of the cumulative displacement.

3.4 Processing methodology

Refer to section 2.4 for the methodology of time series stack production.

3.5 Displacement Velocities

The forecasting study adopted the same classification methodology based on the standard deviation as the monitoring study (section 2.5). The rationale for using this method is that the objective of the study is to detect movement and not to determine where the stable PS are located. In addition, the primary objective is detecting when acceleration begins, which would only involve the PS exhibiting significant movement.

3.5.1 Koidern

The landslide originated where the orange circle is located a rock avalanche with a high velocity that scoured downslope, damming the Koidern river in the valley floor with landslide debris (Fig. 18). Both orbits display decrease in range direction upslope of the slide area, and orbit 116 shows significant decrease in range direction on the ridge and valley opposite the slide over the previous three years. Orbit 123 shows decrease in range direction directly above where the landslide originated in the last three years before the landslide (Fig. 18).

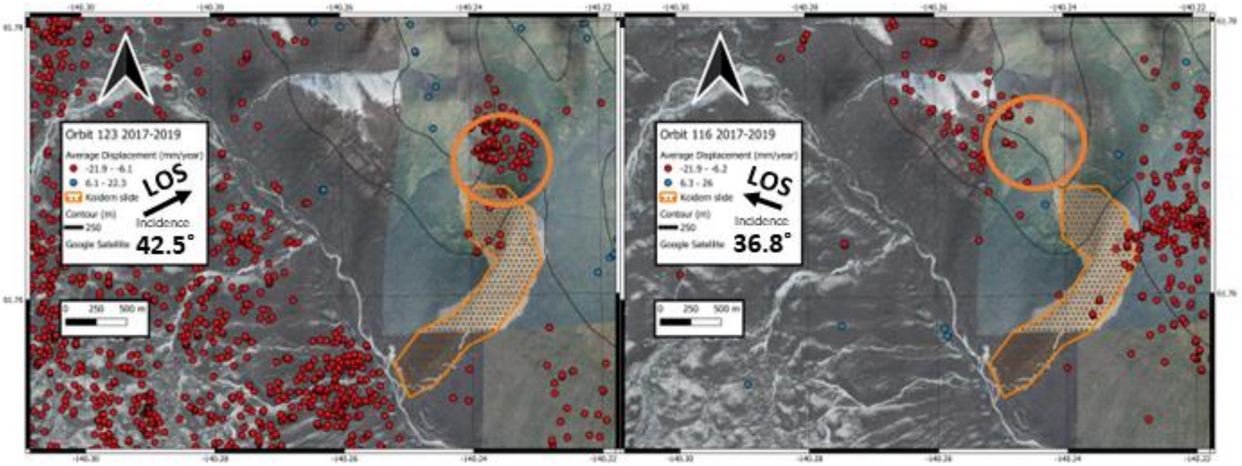

Figure 18 LOS displacement velocity results from the Koidern landslide. The red dot represents an increase in range direction and blue as a decrease. On the left are the results from orbit 123 summer acquisitions, and on the right the results from orbit 116 including the interferograms preceding the landslide event.

3.5.2 Taku River

The Taku slide started as a significant rock slope failure, with a substantial mass detaching from high on the slope. This mass then triggered the collapse of the face of the slope below. Depositing rocks and landslide debris over the Taku River as shown in Figure 19. Both orbits display decrease and a decrease in range direction upslope of the slide area over the last three summers. Orbit 101 shows significant decrease in range direction on the southeast side of the slide and a considerable decrease in range direction on the south side of the slide area. Orbit 174 shows movement away from the satellite directly above and on the landslide (Fig. 19).

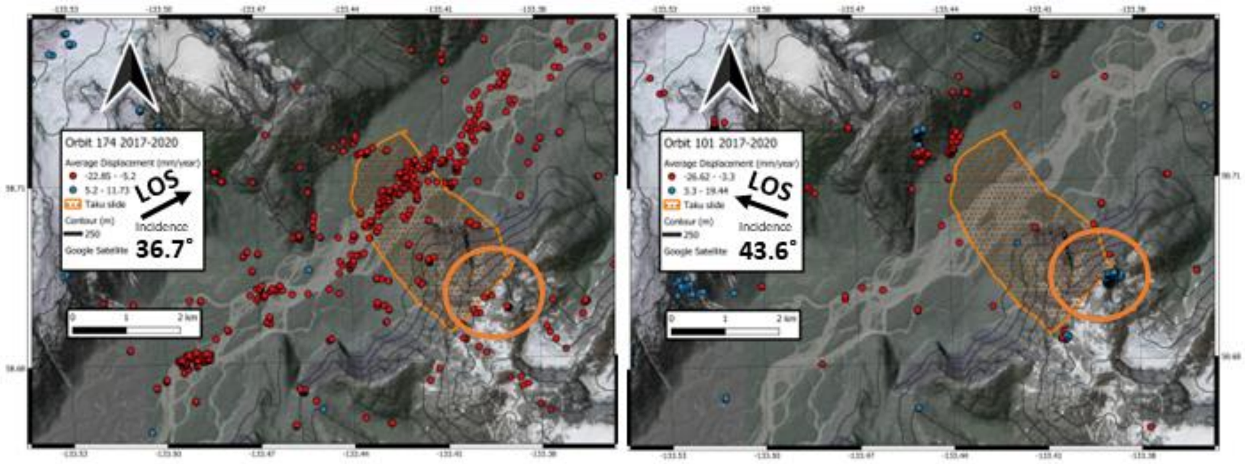

Figure 19 LOS displacement velocity results from the Taku landslide. The red dot represents an increase in range direction and blue as a decrease. On the left are the results from orbit 174 and on the right the results from orbit 101.

3.5.3 Canoe Glacier

Roughly, five million tonnes of rock and ice fell from the Canoe Glacier creating a large runout debris flow. The landslide occurred on the north side of the glacier, moving southwards and then onto the glacier below (Fig. 20). The slide happened on July 1/2021; only the summer images were used in the time-series processing. In orbit 28, two areas show an increase in range direction are on either side of the glacier, and orbit 108 also captures these two points moving. However, the movement on the north side of the glacier is displayed as a decrease in range direction in orbit 108 (Fig. 20). No displacements of significance were detected above where the slide occurred as the area is a high-altitude snow-dominated environment.

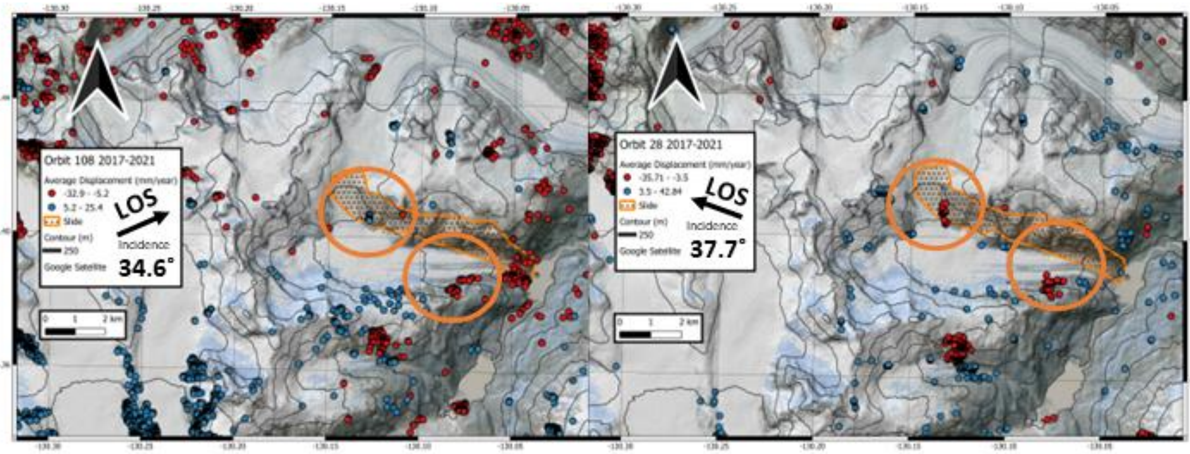

Figure 20 LOS displacement velocity results from the Canoe landslide. The red dot represents an increase in range direction and blue as a decrease. On the left are the results from orbit 101 and on the right the results from orbit 174.

3.5.4 Ecstall River

The orange circles show where the landslide started as a failure on a near-vertical rockface, and then transitioned into a classic ice/rock avalanche—the slide deposited rock into a lake, creating a tsunami and outburst flood downstream (Fig. 21). The slide occurred on September 1/2022, and only the summer images were used in the time-series processing. In orbit 6, one area shows a increase in range direction located above the slide area. Orbit 108 also captures the movement above and to the west of the slide area (Fig. 21).

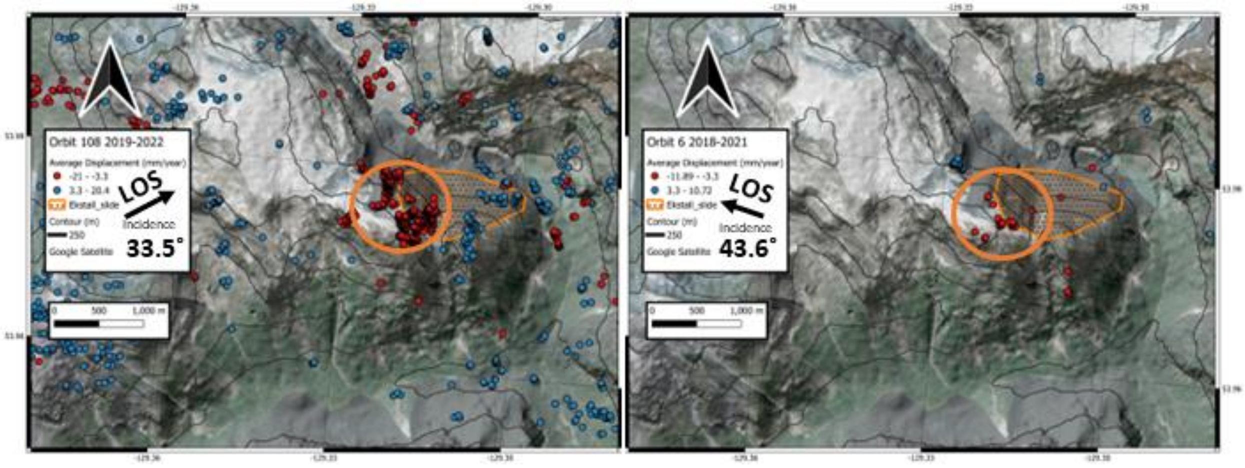

Figure 21 LOS displacement velocity results from the Ecstall landslide. The red dot represents an increase in range direction and blue as a decrease. On the left are the results from orbit 174 and on the right the results from orbit 101.

3.5.5 Elliot Lake

The landslide deposited debris into a glacier lake that displaced water sending a tsunami and outburst flood scouring the stream to the ocean (Fig. 22). The slide area is large and shows evidence of previous landslide area. Orbits 86 displays a decrease in range direction in the middle of the slide area. While orbit 137 shows an decrease in range direction in the same part of the slide area as orbit 86 (Fig. 22).

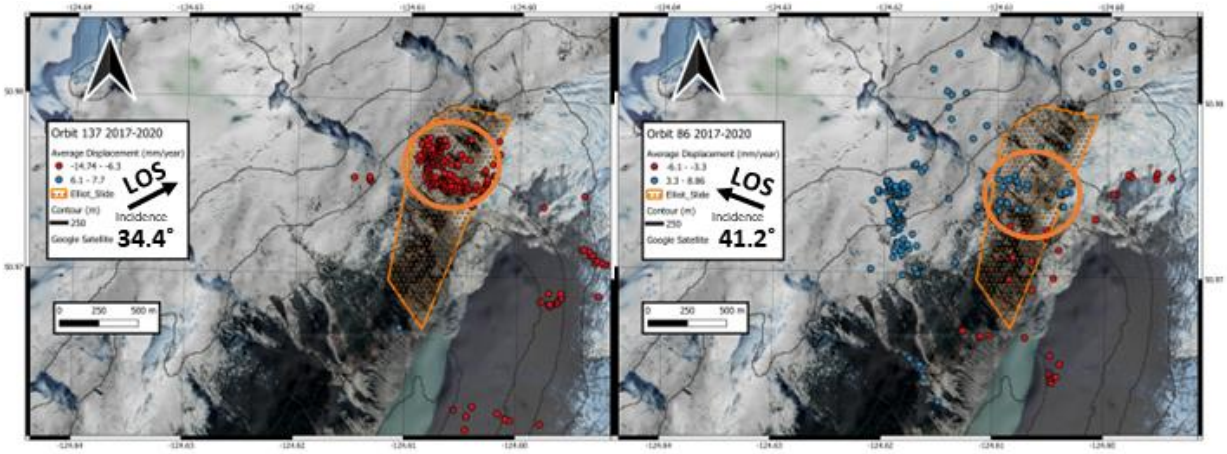

Figure 22 LOS displacement velocity results from the Elliot landslide. The red dot represents an increase in range direction and blue as a decrease. On the left are the results from orbit 174 and on the right the results from orbit 101.

3.6 StaMPS Visualizer

The Stamps Visualizer plots the cumulative displacement on the Y axis and the date on the X axis. The points were fit using a polynomial expression, and the ascending and descending orbits are displayed side by side. The onset of acceleration was determined at the point where the curve begins to dip or bend upwards; graphs with straight lines were deemed regions of uniform movement over the time series.

3.6.1 Koidern

Both orbits display movements away from and towards the satellite (Fig. 23). Orbit 123 shows stability over 2017-2018, but the 2019 movement away from the satellite is detected. The cumulative LOS displacement for orbit 123 is ~45 mm. The last three data points on orbit 123 appear to show acceleration away from the satellite. Orbit 116 shows a trend towards the satellite since 2017 and a cumulative displacement of ~30 mm.

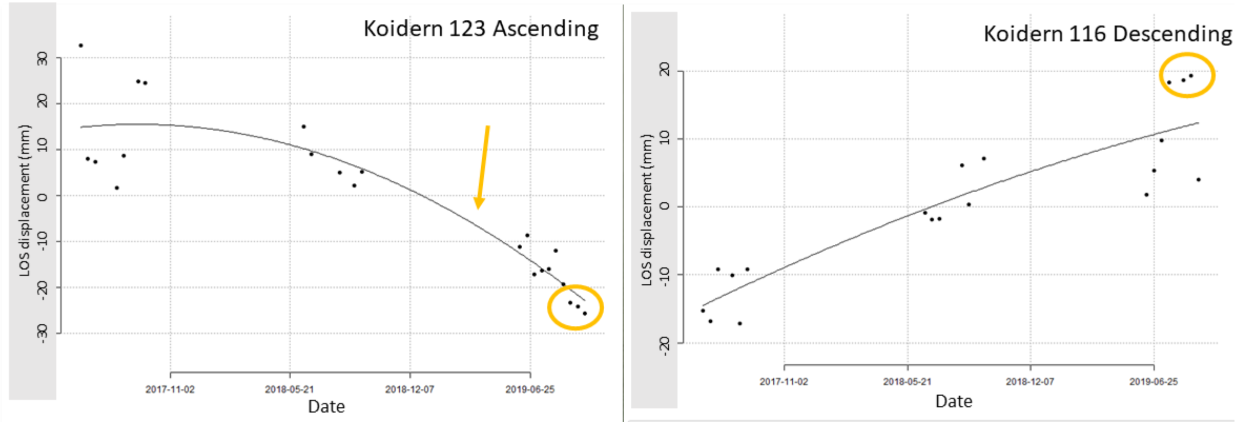

Figure 23 The StaMPS visualizer results for the Koidern Landslide with orbit 123 on the left and orbit 116 on the right. Positive values indicate movement toward, and negative values movement away from the satellite. The orange circle highlights the PS before the landslide, and the orange arrow denotes possible acceleration onset.

3.6.2 Taku River

Both orbits display movements away from and towards the satellite (Fig. 24). Orbit 174 shows stability over 2017-2019, but in 2020, movement away from the satellite is detected. The cumulative LOS displacement for orbit 174 is ~30 mm. Orbit 101 shows a trend towards the satellite since 2017 and a cumulative displacement of ~35 mm.

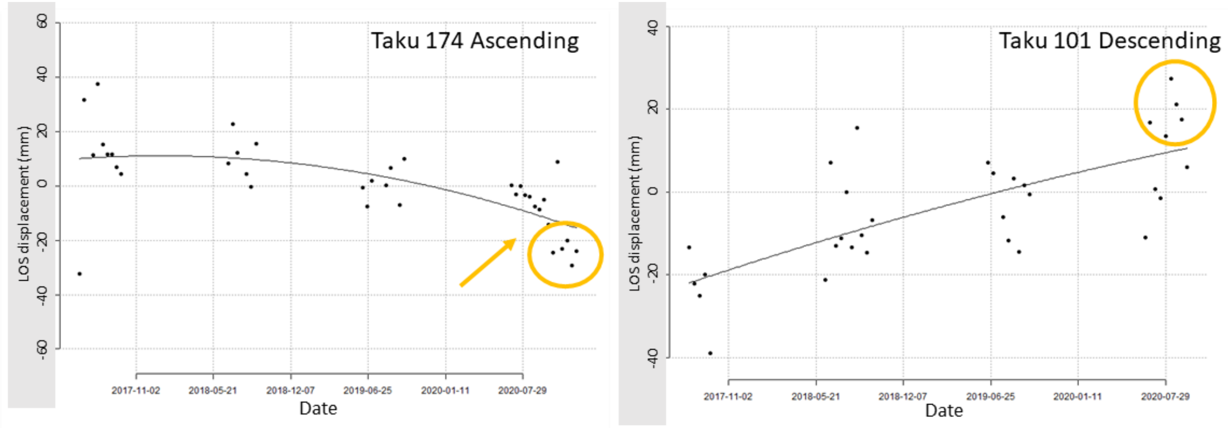

Figure 24 The StaMPS visualizer results for the Taku Landslide orbit 174 on the left and 101 on the right. Positive values indicate movement toward, and negative values movement away from the satellite. The orange circle highlights the PS before the landslide, and the orange arrow denotes possible acceleration onset.

3.6.3 Canoe Glacier

Both orbits display movements away from and towards the satellite (Fig. 25). Orbit 28 shows stability over 2017-2019, but the 2020 movement away from the satellite is detected. The cumulative LOS displacement for orbit 28 is ~60 mm over four years. Orbit 108 shows stability from 2017-2019 a trend of movement towards the satellite since 2020 and a cumulative displacement of ~40 mm. The sparse data from the early summer of 2021 shows movement away from and toward the satellite.

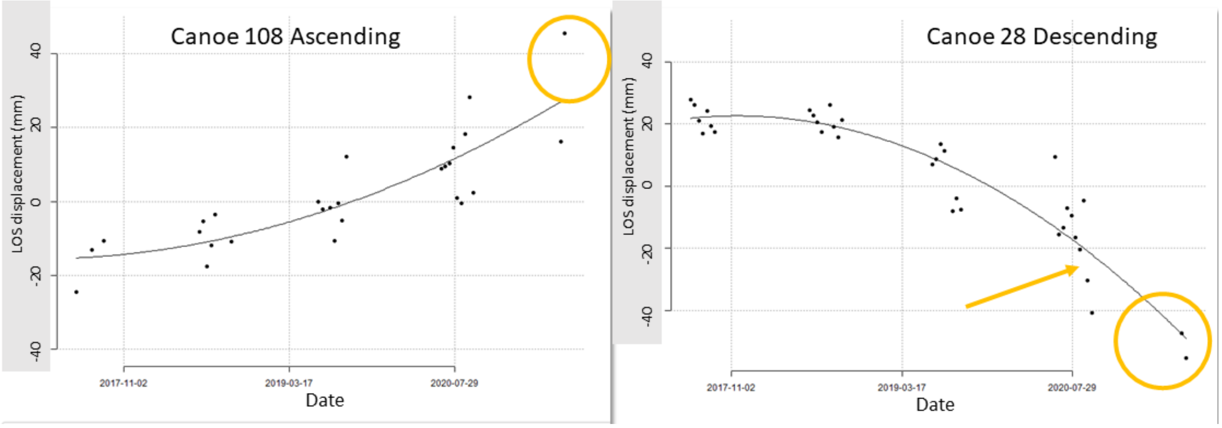

Figure 25 The StaMPS visualizer results for the Canoe Glacier Landslide with 108 on the left and 28 on the right. Positive values indicate movement toward, and negative values movement away from the satellite. The orange circle highlights the PS before the landslide, and the orange arrow denotes possible acceleration onset.

3.6.4 Ecstall River

Both orbits display movements away from the satellite (Fig. 26). Orbit 6 shows stability over 2018-2020, but in 2021 movement away from the satellite is detected. The cumulative LOS displacement for orbit 6 is ~40 mm. Orbit 108 shows a movement trend away from the satellite since 2018 and a cumulative displacement of ~70 mm. The acquisitions in the late summer of 2021 show movement away from the satellite in both orbits.

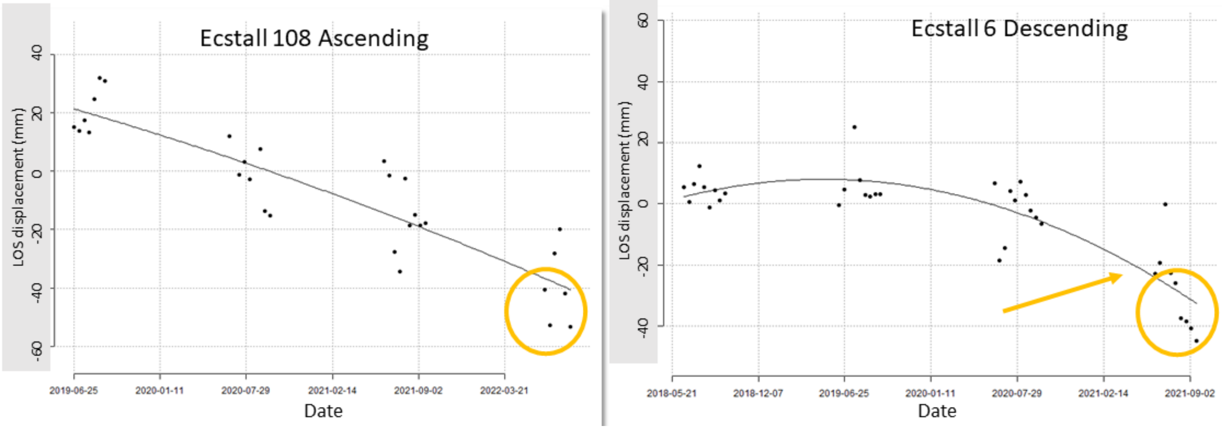

Figure 26 The StaMPS visualizer results for the Ecstall River Landslide with orbit 108 on the left and 0rbit six on the right. Positive values indicate movement toward, and negative values movement away from the satellite. The orange circle highlights the PS before the landslide, and the orange arrow denotes possible acceleration onset.

3.6.5 Elliot Lake

Both orbits display movements away from and towards the satellite (Fig. 27). Orbit 137 shows stability over 2017-20, but in 2020, movement away from the satellite is detected. The cumulative LOS displacement for orbit 137 is ~40 mm. Orbit 86 shows a trend towards the satellite since 2017 and a cumulative displacement of ~30 mm.

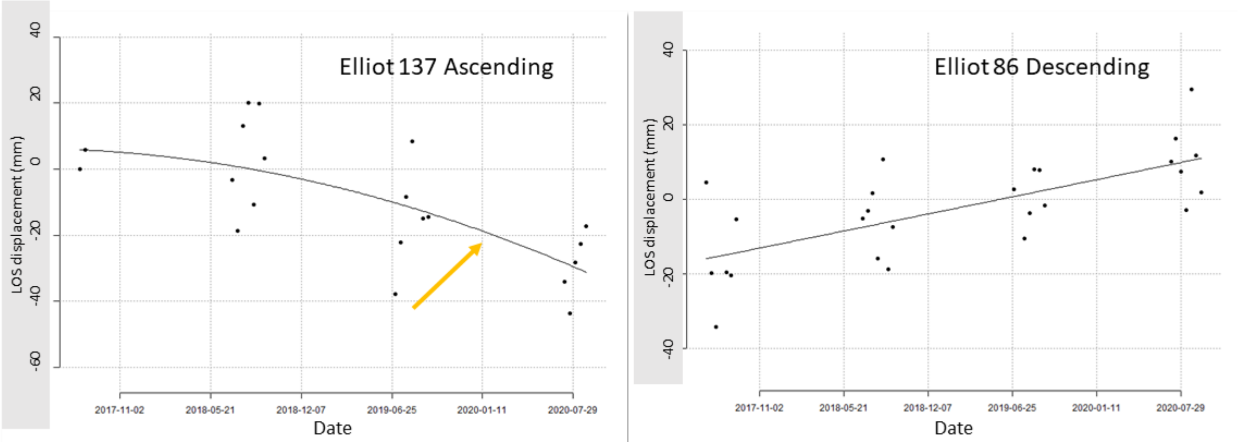

Figure 27 The StaMPS visualizer results for the Elliot Lake Landslide with orbit 137 on the left and 86 on the right. Positive values indicate movement toward, and negative values movement away from the satellite. The orange circle highlights the PS before the landslide, and the orange arrow denotes possible acceleration onset.

3.7 Inverse Velocity Plots

Identifying the data points accelerating before the landslide event is the key to plotting the inverse velocity. The results of the Canoe Glacier site were not of sufficient quality to be used in the study, and as such, only two interferograms were created before the failure. However, inverse velocity plots were created for the other four sites, and a forecasted failure time was established. The forecast time was extrapolated from the best-fit line as to when the line would reach zero on the Y-axis. The plotting of the acceleration was determined by analyzing the StaMPS visualizer results and calculating the displacement velocities once the onset of acceleration was determined.

The inverse velocities are plotted on the Y-axis with the date of the interferogram on the X-axis. The R^2 value represents the best-fit line's linearity and is displayed on the graphs.

3.7.1 Koidern River

The StaMPS visualizer results showed displacement trends over three years (Fig. 23). The study looked at the summer results and months preceding the failure. The inverse velocity plot for Koidern River had an R^2 value of 0.9002. The best-fit line forecasted failure on January 30, 2020, roughly five weeks after the landslide event (Fig. 28).

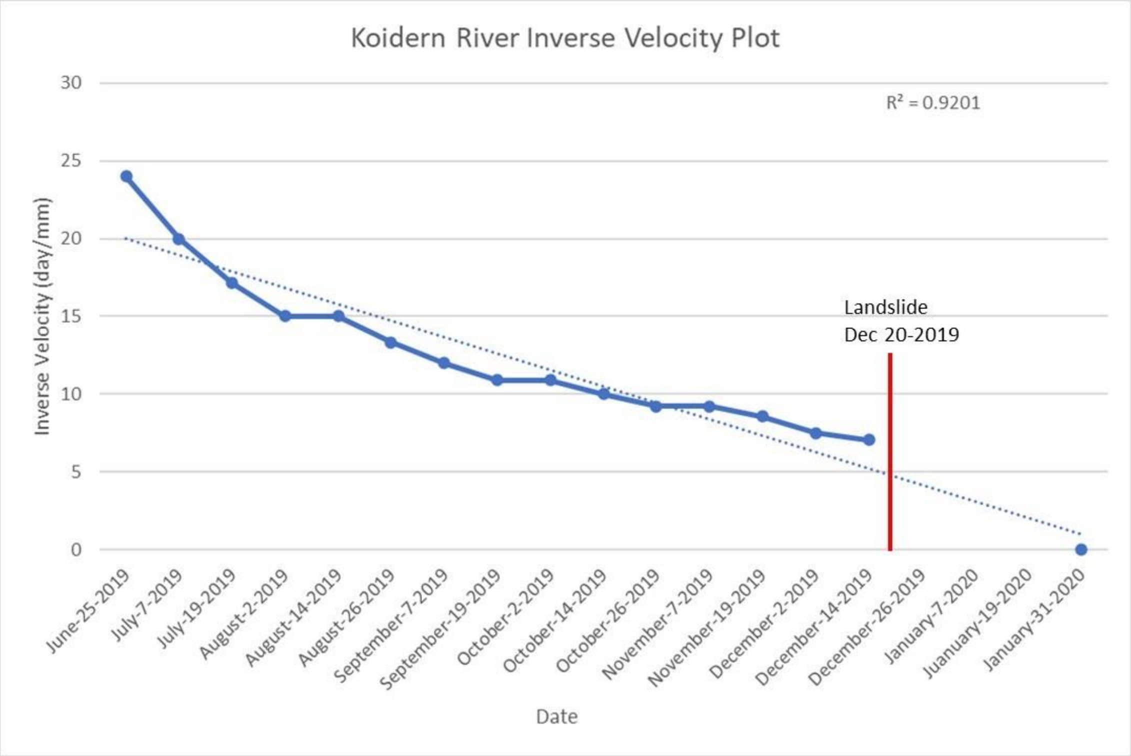

Figure 28 The Inverse Velocity Plot for Koidern River. The red line demotes the date of the landslide failure.

3.7.2 Taku River

The StaMPS visualizer results showed displacement trends over four years (Fig. 24). The study used the results of the two months preceding the failure. The inverse velocity plot for Taku River had an R^2 value of 0.9477. The best-fit line forecasted failure on January 26, 2021, roughly four weeks after the landslide event (Fig. 29).

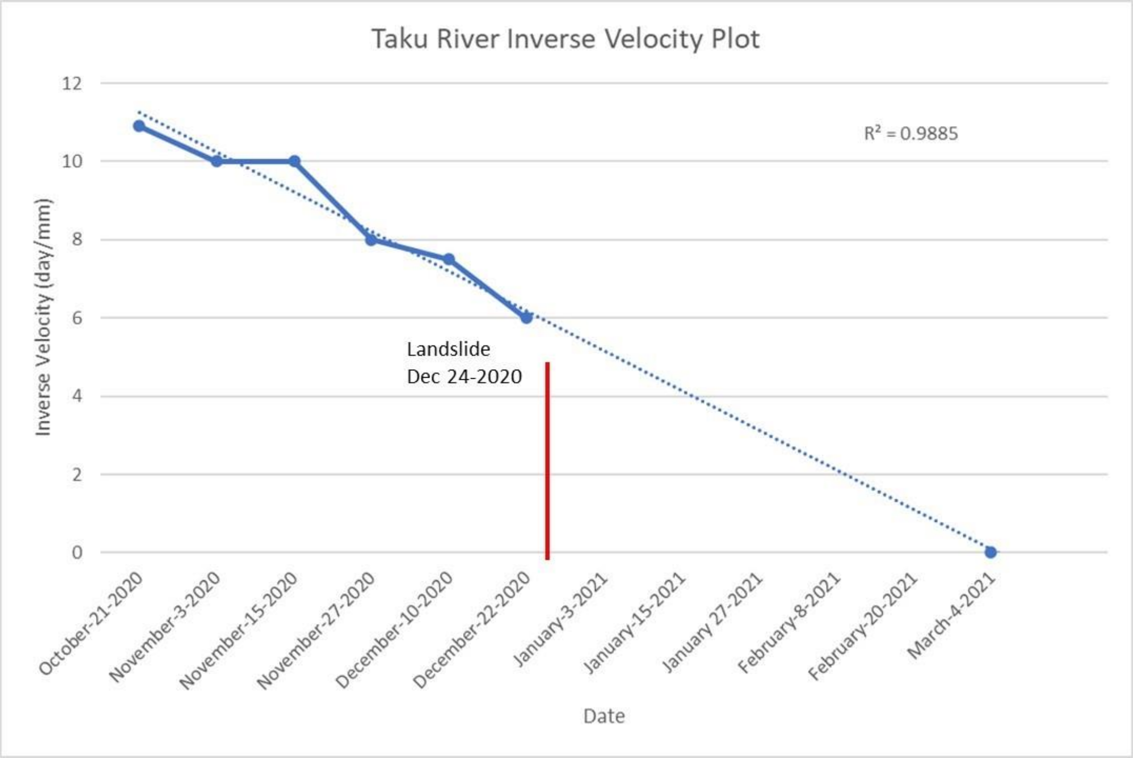

Figure 29 The Inverse Velocity Plot for Taku River. The red line demotes the date of the landslide failure.

3.7.3 Ecstall River

The StaMPS visualizer results showed displacement trends over four years (Fig. 26). The study used the results of the summer months preceding the failure. The inverse velocity plot for Ecstall River had an R^2 value of 0.9225. The best-fit line forecasted date of September 22, 2022, roughly 3 weeks after the landslide event (Fig. 30).

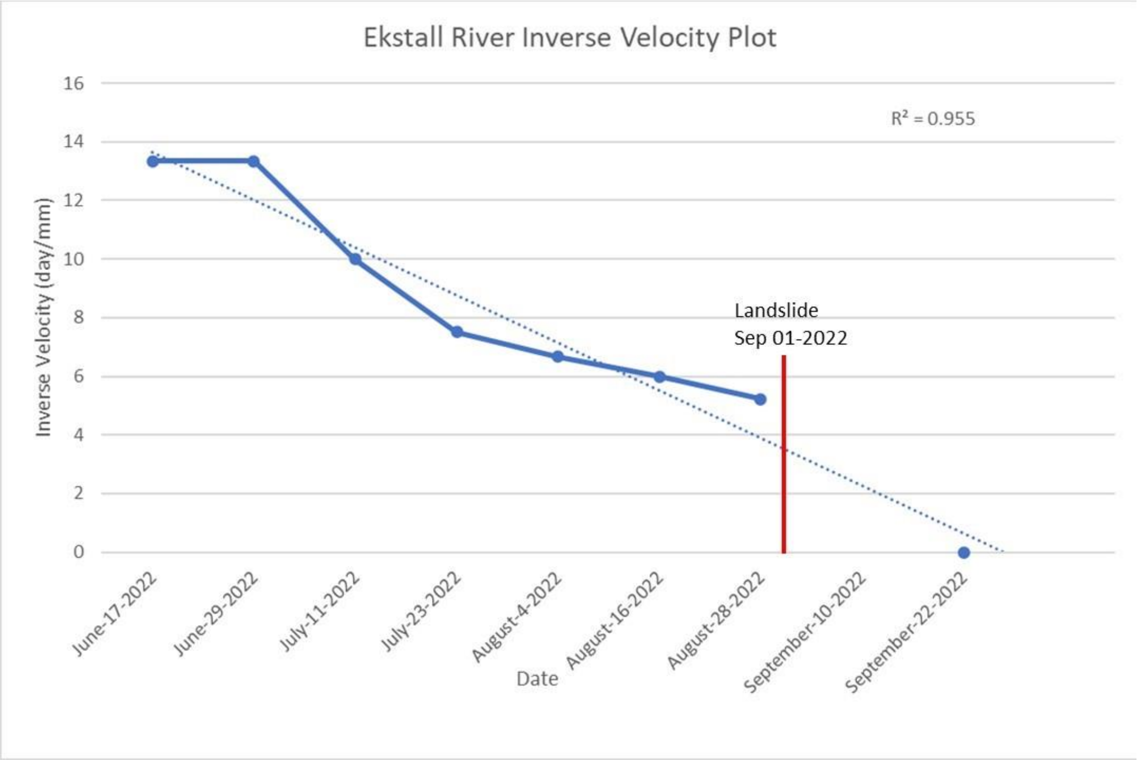

Figure 30 The Inverse Velocity Plot for Ecstall River. The red line demotes the date of the landslide failure.

3.7.4 Elliot Lake

The StaMPS visualizer results showed displacement trends over four years (Fig. 27). The study used the results of the summer months preceding the failure. The inverse velocity plot for Elliot Lake had an R^2 value of 0.9712. The best-fit line forecasted date of October 18, 2020, roughly four weeks before the landslide event (Fig. 31).

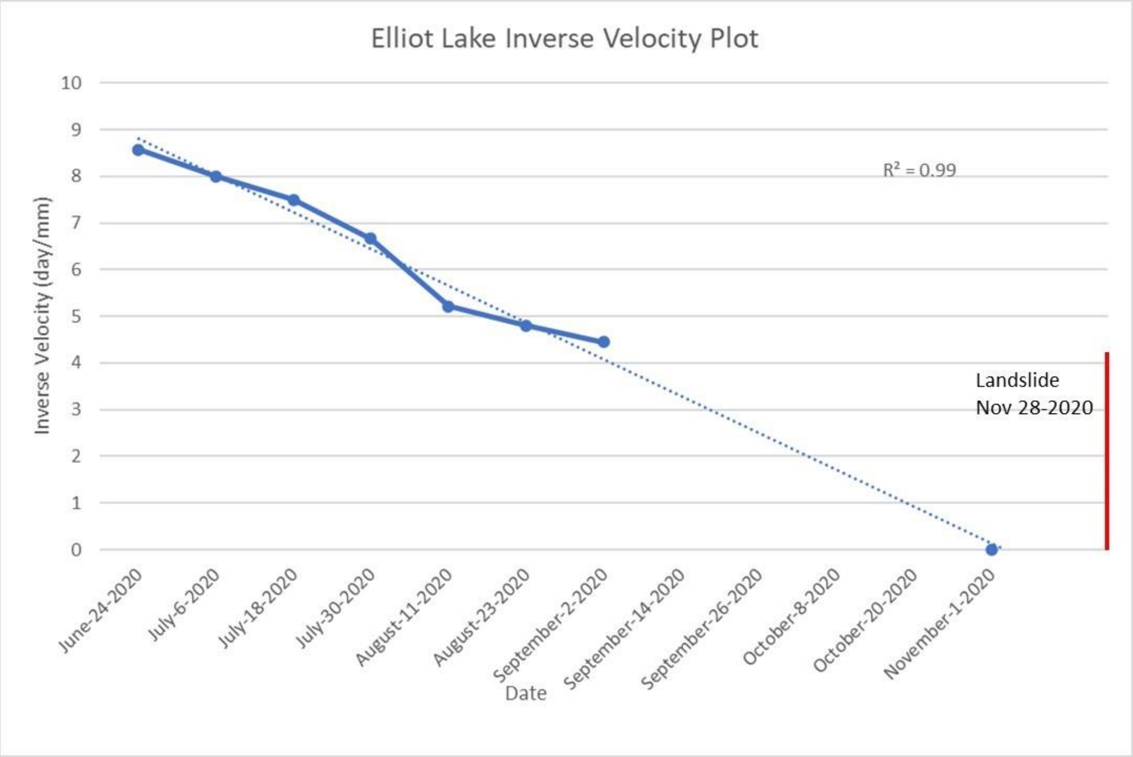

Figure 31 The Inverse Velocity Plot for Elliot Lake. The red line demotes the date of the landslide failure.

3.8 Weather

The weather conditions that may have triggered to the catastrophic failures were varied and site-specific. The Ecstall River and Elliot Lake sites had cumulative precipitation of 81.8 mm and 108.4 mm, respectively, in the two weeks preceding the landslides. An unseasonable hot air mass preceded the Canoe Glacier event termed the 2021 heat dome. The Taku River site had a precipitation event followed by below-freezing temperatures. The Koidern landslide had no precipitation beforehand and seasonal temperatures for December in the Yukon (Table 8).

Table 8 Weather from the closest weather station to each landslide displaying the average temperature and cumulative precipitation two weeks before the failures.

Site	Station	Climate ID	Average temp (C˚)	Precipitation (mm)
Koidern	Burwash A	2100181	-12.1	0.4
Taku River	Teslin (AUT)	2101102	-18.8	15.1
Canoe Glacier	Stewart A	1067748	22.4	0
Ecstall river	Kitimat hatchery	106D289	24.7	81.8
Elliot Lake	Fanny Island	1022795	7.9	108.4

3.9 Seismicity

The Koidern River, Ecstall River, and Elliot Lake sites had seismicity in the two weeks preceding the landslides and the Canoe Glacier and Taku River sites had no seismicity detected (Table 9). The Koidern site had a 2.3 ML earthquake 13 days before the slide. The Ecstall River site had a swarm of five earthquakes the day of the slide, as well as many less than 2 ML that are not shown in Table 9. Elliot Lake had three earthquakes on the day of the landslide, ranging from 2.1 to 2.3 ML.

Table 9 Seismicity above 2ML within 50 Km two weeks preceding the landslides in the study.

Site	Date	Depth (km)	Magnitude (ML)	Distance of earthquake from landslide event
Koidern	2019-12-07	1	2.3	45 km SW of event
Taku	NA	NA	NA	NA
Canoe	NA	NA	NA	NA
Ecstall	2020-08-30	10	2.5	200 Metres W of event
Ecstall	2020-08-30	10	2.1	10 Km N of event
Ecstall	2020-09-01	5	2.0	17 Km N of event
Ecstall	2020-09-01	5	2.1	7 Km N of event
Ecstall	2020-09-01	5	2.4	19 Km SW of event
Elliot	2020-11-25	40	2.3	30 Km SE of event
Elliot	2020-11-28	20	2.3	650 Metres NW of event
Elliot	2020-11-28	20	2.1	2 Km W of event

3.10 Discussion

Based on the study, it appears that InSAR technology has the potential to detect ground movements before a catastrophic event occurs. The analysis at each site revealed movement before the landslide, and some even detected the onset of acceleration. However, the occurrence of landslides is influenced by various factors, such as precipitation, temperature, and ground creep, which all impact the inverse velocity plots and make it challenging to predict such events precisely. Unfortunately, interferograms produced during snowy seasons resulted in degraded PS detection, rendering a year-round landslide forecasting detection system infeasible. Furthermore, the 12-day repeat time of the Sentinel-1 satellite may not be adequate to detect accelerations that cause landslides within days or hours. Nonetheless, InSAR results can still help identify hazard-prone slopes currently or recently in motion.

3.10.1 Displacement Velocities

Through the InSAR results over multiple years, precursory movement was observed at all landslide study sites, with some sites displaying accelerated movement the year before failure. Even at three low snow accumulation sites, PS and movement were detected, indicating that Sentinel-1 InSAR data can identify precursor ground movement on slopes before catastrophic failure. However, interferograms created during the winter months of Canoe Glacier were found to be unusable. Carlà (2019) concluded from the Bosmatto landslide study that InSAR could penetrate dry, cold snow to a 20-meter depth. Therefore, the effectiveness of a year-round landslide early warning system would depend on the amount and consistency of accumulated snow.

Displacement data can be unreliable due to seasonal changes in hydrological conditions that cause the ground to swell or subside. Determining whether the ground moved due to seismic activity, precipitation, or temperature changes during summer is difficult. The graphs show that the ground subsides during the summer as it dries out and releases pore pressure. Similar seasonal trends have been observed in InSAR studies conducted in permafrost regions (Rouyet et al., 2019; Wang et al., 2020; Liu et al., 2022). Therefore, in this study, the best-fit lines were used to accurately measure any movement and overcome the noise caused by seasonal variability in the data.

3.10.2 Weather Data

The weather dramatically impacts freeze and thaw cleaving, fracturing, erosional and hydrological processes at work on mountain slopes (Cloutier et al., 2017; Crosta et al., 2017). Weather events impacted all the sites in the study before their catastrophic failures. The Elliot Lake and Ecstall River sites were affected by sizeable cumulative precipitation before the landslides. The high temperatures associated with the heat dome event of June 2021 also contributed to accelerated snowmelt processes and may have thawed permafrost, adding to slope instability before the Canoe Glacier event. Conversely, temperatures colder than minus thirty Celsius were recorded before the landslides at the Koidern and Taku Rivers. The Taku River site had also recorded precipitation before the cold snap. The property of water to swell by 10% when frozen would impact the cleaving and fracturing processes at the site (Cloutier et al., 2017). Overall, each site had a unique weather event that that can be interpreted to have affected the slope integrity preceding the catastrophic failure.

3.10.3 Seismicity

It has been observed that earthquakes can cause landslides either immediately or days to weeks later, as reported by Cappa (2004) and Delgado (2019). Although no seismic activity was detected at the Taku River and Canoe Glacier sites, the other three sites had seismic activity before the landslide event. Two of the three seismically active sites had earthquakes on the same day as the catastrophic failure, while the Koidern River site had seismic activity a week before the landslide. Studies conducted in Greenland, Norway, and Iceland have also found seismic activity related to glacial melt and the movement of glaciers from degradation, as reported by Ekstrom (2006), Bungum (2010), and Lacroix (2020).

The landslides at Ecstall River and Elliot Lake happened after a hot summer that would have contributed to glacial melt and retreat. Both sites also experienced significant precipitation events before the landslide. The cumulative impact of a hot summer followed by heavy rainfall possibly triggered the seismic activity from the glacial recession. The sites recorded seismic activity on the same day as the landslide. Extreme precipitation and heat caused by climate change create a feedback loop that leads to glacial retreat, followed by an isostatic adjustment initiating seismic activity, and increasing landslide activity in the western Canadian Cordillera. However, currently the InSAR technique does not acquire imagery quickly enough to detect ground acceleration from same-day seismic activity.

3.10.4 Feasibility of Forecasting with Sentinel-1

Although the inverse velocity plots failed to predict the catastrophic landslides with enough warning time, the study found that sites with notable acceleration data could forecast failures within two months of the actual event. This emphasizes the challenge of precisely predicting failures resulting from destabilizing factors such as weathering, hydrological erosion, glacial loss, seismicity, and tertiary creep for years. Therefore, it is evident that a single event cannot be held responsible for such failures.

It is possible to use Sentinel-1 InSAR findings to monitor landslides in the western Canadian coast mountains utilizing snow-free summer imagery. The outcomes of winter stacks must be adequate to constitute an effective early warning system. Identifying the acceleration of the landslide before the failure is imperative to alert the inhabitants of an impending catastrophic failure. If InSAR provides unsatisfactory results from winter acquisitions, identifying the acceleration through InSAR is impossible. The seasonal method reveals areas of movement and stability. Therefore, the InSAR method can recognize unstable regions from space and guide geotechnical surveys on the ground. Additionally, the study's outcomes provide a foundation for future InSAR research to identify changes in stability.

3.11 Conclusion

All the sites in the study had precursor movement on the slopes detectable by the InSAR results. Each site was also impacted by recent extreme weather events preceding the catastrophic failure. The Elliot Lake and Ecstall River sites had same-day seismicity possibly linked to glacial loss and retreat. The results collected while the snow was on the ground were degraded and less robust than the seasonal approach. Unfortunately, the Sentinel-1 repeat window every 12 days is not a short enough temporal resolution for a reliable real-time landslide early warning system. In the end, the results show that the InSAR results can be used as a hazard identification tool for slopes that are moving or slopes that have begun to move recently.

Chapter Four: Limitations and Feasibility of InSAR and Landslide monitoring.

Chapters two and three explored the capabilities and limitations of InSAR for landslide monitoring and forecasting. This section will delve deeper into InSAR functionality's technical, methodological, and real-world aspects. Additionally, I will look toward the future of InSAR and its role in landslide monitoring.

Here is a review of some critical limitations in analyzing the displacement results. The InSAR methodology used in the study area could not capture continuous movement due to the limitations of Sentinel-1's sensor. The wavelength used by the sensor cannot penetrate snow and vegetation. In western Canada, this leads to a knowledge gap in ground movement during winter (Ferretti et al., 2001). Additionally, the PS methodology cannot detect some fast-moving ground deformation exceeding 40 mm between acquisitions (Squarzoni et al., 2020). A contributing factor to this limitation is that the temporal resolution of 12 days is insufficient to detect such movement (Bar & Dixon, 2021). Despite these limitations, the study still produced results and qualified the ground movement in the study area.

4.1 Technical Limitations

The Sentinel-1 constellation provides free data with high spatial and temporal resolution, enabling the scientific community to explore ground deformation on Earth with millimetre precision. Researchers have been able to monitor landslides from space and predict such events in hindsight within weeks (Crossetto et al., 2016; Intrieri et al., 2018; Carlà et al., 2019). However, several technical limitations still pose challenges.

Generating time series displacement maps can be challenging, primarily due to the intricate software packages discussed in Chapter 2 and the required computer processing power. The SNAP-StaMPS workflow by Crosetto (2016) necessitates two hardware systems, one for Windows and another for Linux. Maneuvering through various software packages can also be complicated, potentially discouraging inexperienced researchers from attempting the task. Furthermore, the StaMPS software demands the installation and understanding of an AWS instance to adjust the computer's performance based on the complexity and size of the time-series stacks. Additionally, due to hardware constraints, the SNAP software's processing capabilities are limited to only two S-1 IW SLC product bursts at a time, making it time-consuming to analyze large regions.

Another technical issue is that the displacement results from the StaMPS software cannot be viewed directly in the interface. Instead, the mean velocities compiled from the best-fit line methodology are exported as a .csv file. To track deformation for a single point over the monitoring period, Hoeser (2020) developed the StaMPS visualizer tool. However, this tool requires the user to have GIS software to view the average displacements and R studio to operate the visualizer. The introduction of two more software packages makes the processing chain even more complicated.

4.2 Methodological Limitations

The thesis focuses on how InSAR methodology intersects with landslide monitoring. It is worth noting that there are certain methodological limitations when dealing with radar images captured from space, especially in steep topography areas prone to landslides. Factors such as foreshortening, layover, and shadow may impact the accuracy of the findings. Shadows may obscure the signal source, while foreshortening and layover can limit the validity of the results

(Ferretti et al., 2007). The orientation of the landslide of interest is also a limiting factor. Since Sentinel-1 is a polar circular platform with a right-looking antenna slope, it is better suited for detecting movement towards and away from the satellite in an east-west direction. Therefore, slopes oriented in a north-south alignment may not be suitable for this approach. It is recommended to analyze the look angles of the satellite in relation to the slope of interest before proceeding with this methodology (Ferretti et al., 2007).

Regarding the pixel phase signal, there is a methodological limitation regarding the PS criteria used to select PS candidates. Specifically, pixels with a high phase noise signal in the SAR image are excluded. The topography and land cover influence this noise, typically consisting of pixels that exhibit variability over time (Hooper et al., 2012). This excludes pixels with dominant vegetation, wetlands, snow cover, and human-induced ground disturbance. In addition, the PS methodology may interpret slope movement as noise and exclude it from the time series analysis (Necula et al., 2017). The SBAS method analyzes all the distributed scatterers and may be better suited for highly vegetated, snow-dominated, and wet areas such as Canada. The SBAS method was not performed in this thesis due to the software constraints of SNAP but is recommended as a future suggestion for incorporation.

One significant drawback of using the StaMPS methodology for landslide forecasting is its tendency to primarily identify linear trends. To detect accelerating behaviour, the inverse velocity methodology is utilized. However, the analysis in StaMPS can sometimes filter out acceleration due to the phase signal being too unstable. According to a review by Osmanoglu (2016), SqueeSAR software can detect accelerating trends. Unfortunately, the review did not compare StaMPS to SqueeSAR due to financial limitations. Therefore, using the SqueeSAR methodology for landslide forecasting and inverse velocity plotting may be more effective than the current implementation of the StaMPS software, however with a cost trade-off.

To accurately assess slope movement, it's crucial to consider the distribution and quantity of PS that exhibit notable increases or decreases in range direction throughout the terrain. The findings of the study reveal that significant movement is observed across the maps not just where the landslides occurred. But in regions where glacial retreat is apparent, areas that past landslides are evident, and along river and stream beds. Nevertheless, the results of both studies found distinct trends of clustered PS and the identification of movement in multiple orbits. Consequently, utilizing InSAR as a means of identifying slow-moving slopes can be a site-specific and time-intensive process.

4.3 Real-World Contextual Limitations

In my thesis, I presented two different applications of InSAR for monitoring landslides. The first approach focused on monitoring the slopes in Garibaldi Volcanic Complex (GVC) that were prone to landslides and assessed whether bedrock geology affected their stability. The second study examined the feasibility of using InSAR time series to predict landslide failures. However, both studies faced expected challenges in detecting PS in areas with dense vegetation and snow. Weather, seismic activity, and geological factors also influenced the likelihood of landslides. All these variables had a stochastic impact on slope stability, challenging accurate forecasting of failures.

When examining the GVC slopes, the unpredictability of landslide occurrence does not hinder the capacity of the InSAR method to identify movement. However, determining the cause behind the movement is challenging. Without confirmation by ground truthing, it is not feasible to determine if the movement toward the satellite is caused by erosional accumulation, alterations in pore pressure due to hydrological factors, ground uplift from the isostatic adjustment, or motion linked to volcanic activity and inflation within the mountain. Moreover, confirming whether the movement occurs throughout the year or during a particular season becomes challenging due to the absence of consistent data during the winter. Consequently, in Canada, InSAR is currently restricted to being a tool for identifying large-scale moving slopes and directing subsequent on-site exploration and examination.

The landslides in chapter three followed their unique trajectory, influenced by site specific conditions. However, the practical challenge of using InSAR for landslide prediction is that each event is a complex product of its location and is influenced by multiple factors. To forecast landslides, the inverse velocity method relies on identification of distinct patterns of acceleration. This study found that the predicted failures occurred several weeks after (and in one case weeks before) the landslides actually occurred due to various climatic and seismic factors that quite likely triggered slope failures to occur prematurely. Ideally, daily InSAR acquisitions would provide a more nuanced monitoring of ground acceleration in landslide forecasting.

On December 23, 2021, a significant and unforeseen problem occurred that heavily impacted the study. The instrument electronics power supply of Sentinel-1B experienced an anomaly, which caused the satellite to fail in delivering radar data (ESA, 2022). Consequently, only Sentinel-1A was operational, leading to decreased data availability and only one look angle. This problem had a direct impact on the findings from the Ecstall site, as only one orbit of imagery was available just before the landslide event. This highlights one of the drawbacks of relying on satellite data which is that researchers have essentially no control over the instrumentation's operation, which can be a significant limitation in real-world applications, without purpose-built and test-focused orbital platforms.

4.4 Future of InSAR and Landslide Monitoring

It has been announced that in the coming year, the National Aeronautics and Space Administration of the United States and the Indian Space Research Organisation will launch an L and S-Band SAR satellite dedicated to ground movement monitoring. This satellite constellation is expected to provide valuable data for InSAR research in Canada, as the longer band wavelengths can penetrate tree canopies and snow cover. Furthermore, the Sentinel-1B satellite is set to be replaced by Sentinel-1C in early 2024. The Canadian Space Agency's RadarSat Constellation Mission also utilizes the C-Band wavelength and operates on a four-day repeat cycle. With these advancements in sensor technology and InSAR platforms, the future of monitoring is both feasible and exciting.

The future looks bright for InSAR with advancements in geosynchronous SAR systems. High-resolution images with a pixel size of 10 metres will be available every 8 hours, and SAR microsatellites with 1-2 hours revisit times are expected to launch soon (Monti et al., 2017; Paek et al., 2020). With multiple daily updates on hazardous slopes, the limitations of current satellites for InSAR identified in this work are likely to soon be overcome. The improved temporal resolution of the upcoming InSAR satellites will pave the way for real-time landslide early warning systems, utilizing satellite and ground-based monitoring tools to collect more data points characterizing the acceleration phase.

5.0 Conclusion

The study aimed to determine if Sentinel-1 InSAR data could be used to detect precursor ground movement-associated landslides. The InSAR results showed that ground displacement occurred on the slopes of all three study sites in the GVC, which corresponded with previous landslide activity. However, the InSAR results collected during winter months were less detailed and frequent than those collected through the summer months. While a year-round monitoring system is possible with Sentinel-1 data, there may be gaps in data coverage due to snow conditions and site topography. The volcanic units showed more instability than the intrusive bedrock units, except for Mt Garibaldi. Ultimately, the study generated baseline maps of all three mountains' displacement movements for 2017-2021.

The second part of the thesis examined the potential of InSAR results to identify accelerations preceding landslide failures. Analysis of data collected prior to landslides at 5 sites in the western Canadian cordillera analysis shows that all the sites displayed signs of movement on the slopes, which were detected by InSAR. Furthermore, each site encountered extreme weather conditions, which likely contributed to catastrophic failure. The Elliot Lake and Ecstall River sites experienced seismic activity on the same day as the landslide events, potentially connected to glacial loss and retreat. Results obtained during snowfall were less reliable than the seasonal approach. Unfortunately, the Sentinel-1 repeat window of 12 days is insufficient for a dependable real-time landslide early warning system. The study concluded that InSAR results could be valuable for identifying hazards on slopes that are moving or have recently begun to move.

The Sentinel-1 mission's temporal resolution is inadequate for creating a real-time monitoring system for landslide-prone slopes in western Canada. Factors that trigger landslide acceleration, such as precipitation, seismicity, and geological processes, can occur over seconds (in the case of earthquakes), hours to days to years. Hence, the primary role of Sentinel-1 in landslide monitoring is identifying large-scale moving slopes. This inventory can be further analyzed to determine the proximity to local communities, energy and transportation corridors, and sensitive wildlife habitats. However, future InSAR platforms could provide a promising solution with high temporal resolution, making landslide forecasting and monitoring a reality.

6.0 References

Adams, D. (1979). The hitch hiker's guide to the galaxy. Random House.

Allstadt, K. (2013). Extracting source characteristics and dynamics of the August 2010 Mount Meager landslide from broadband seismograms. Journal of Geophysical Research: Earth Surface, 118(3), pp. 1472-1490. doi:10.1002/jgrf.20110

Arias, P., Bellouin, N., Coppola, E., Jones, R., Krinner, G., Marotzke, J., ... & Zickfeld, K. (2021). Climate Change 2021: the physical science basis. Contribution of Working Group I to the Sixth Assessment Report of the Intergovernmental Panel on Climate Change; technical summary.

Bamler, R., & Hartl, P. (1998). Synthetic aperture radar interferometry. Inverse problems. Inverse problems, 14(4), pp. 1-55.

Barla, G., Antolini, F., Barla, M., Mensi, E., & Piovano, G. (2010). Monitoring of the Beauregard landslide (Aosta Valley, Italy) using advanced and conventional techniques. Engineering Geology, 116(3-4), pp. 218-235. doi:10.1016/j.enggeo.2010.09.004

Bar, N., & Dixon, R. (2021). Unveiling unknowns: Practical application of InSAR for slope performance monitoring and risk management across multiple surface mines. Engineering Geology, 293, pp. 1-12. doi:10.1016/j.enggeo.2021.106326

Bekaert, D., Walters, R., Wright, T., Hooper, A., & Parker, D. (2015). Statistical comparison of InSAR tropospheric correction techniques. Remote Sensing of Environment, 170, pp. 40-47. doi:10.1016/j.rse.2015.08.035

Bevington, A., & Menounos, B. (2022). Accelerated change in the glaciated environments of western Canada revealed through trend analysis of optical satellite imagery. Remote Sensing of Environment, 270, pp. 1-16. doi:10.1016/j.rse.2021.112862

Bovis, M., & Evans, S. (1996). Extensive deformations of rock slopes in southern Coast Mountains, southwest British Columbia, Canada. Engineering Geology, 44(1-4), pp. 163-182. doi:101016/S0013-7952(96)00068-3

Bozzano, F., Mazzanti, P., Perissin, D., Rocca, A., De Pari, P., & Discenza, M. (2017). Basin scale assessment of landslides geomorphological setting by advanced InSAR analysis. Remote Sensing, 9(3), pp. 1-19. doi:10.3390/rs9030267

Braun, A. (2021). Retrieval of digital elevation models from Sentinel-1 radar data – open applications. Open Geosciences, 13(1), pp. 532-569. doi:10.10.1515/geo-2020-0246

Bruce, J., & Cohen, S. (2004). Impacts of climate change in Canada. In Hard Choices: climate change in Canada pp. 273-281. Wilfred Laurier Press.

Bungum, H., Olesen, O., Pascal, C., Gibbons, S., Lindholm, C., & Vestøl, O. (2010). To what extent is the present seismicity of Norway driven by post-glacial rebound? Journal of the Geological Society, 167(2), pp. 373-384. doi:10.1144/0016-76492009-009

Burns, S. (2013). Processes, transport, deposition, and landforms: Slides. In F. John, M. Stoffel, & R. Marston, Treatise on Geomorphology. pp. 152-157. San Diego: Academic Press.

Cappa, F., Guglielmi, Y., Soukatchoff, V., Mudry, J., Bertrand, C., & Charmoille, A. (2004). Hydromechanical modeling of a large moving rock slope inferred from slope levelling coupled to spring long-term hydrochemical monitoring: example of the La Clapiere landslide (Southern Alps, France). Journal of Hydrology, 291(1-2), pp. 67-90. doi:10.1016/j.jhydrol.2003.12.013

Carlà, T., Farina, P., Intrieri, E., Ketizmen, H., & Casagli, N. (2018). Integration of ground-based radar and satellite InSAR data for the analysis of an unexpected slope failure in an open-pit mine. Engineering Geology, 235, pp. 235-252. doi:10.1016j.enggeo.2018.01.021

Carlà, T., Intrieri, E., Di Traglia, F., Nolesini, T., Gigli, G., & Casagli, N. (2017). Guidelines on the use of inverse velocity method as a tool for setting alarm thresholds and forecasting landslides and structure collapses. Landslides, 14(2), pp. 517-534. doi:10.1007/s10346-016-0731-5

Carter, N. (1932). Exploration in the Lillooet River watershed. Canadian Alpine Journal, 21, pp. 8-18.

Cascini, L., Fornaro, G., & Peduto, D. (2010). Advanced low-and full-resolution DInSAR map generation for slow-moving landslide analysis at different scales. Engineering Geology, 112(1-4), pp.29-42.

Chen, C., & Zebker, H. (2001). Two-dimensional phase unwrapping with use of statistical models for cost functions in nonlinear optimization. JOSA A, 18(2), pp. 338-351.

Clague, J., & O’Connor, J. (2021). Glacier-related outburst floods. In W. Haeberli, & C. Whiteman, Snow and ice-related hazards, risks, and disasters pp. 467-499. Elsevier. doi:10.1016/B978-0-12-817129-5.00019-6

Cloutier, C., Locat, J., Geertsema, M., Jakob, M., & Schnorbus, M. (2017). Potential impacts of climate change on landslides occurrence in Canada. In Slope safety preparedness for impact of climate change pp. 71-107. CRC Press.

Cossart, E., Braucher, R., Fort, M., Bourlès, D., & Carcaillet, J. (2008). Slope instability in relation to glacial debuttressing in alpine areas (Upper Durance catchment, southeastern France): evidence from field data and 10Be cosmic ray exposure ages. Geomorphology, 95(1-2), pp. 3-26. doi:10.1016/j.geomorph.2006.12.022

Crosetto, M., Castillo, M., & Arbiol, R. (2003). Urban subsidence monitoring using radar interferometry. Photogrammetric Engineering & remote sensing, 69(7), pp. 775-783. doi:10.14358/PERS.69.7.775

Crosta, G., Agliardi, F., Rivolta, C., Alberti, S., & Dei Cas, L. (2017). Long-term evolution and early warning strategies for complex rockslides by real-time monitoring. Landslides, 14(5), pp. 615-632. doi:10.1007/s10346-017-0817-8

Crozier, M. (2010). Deciphering the effect of climate change on landslide activity: A review. Geomorphology, 124(1-3), pp. 260-267.

Cruden, D., & Lu, Z. (1992). The rockslide and debris flow from Mount Cayley, BC, in June 1984. Canadian Geotechnical Journal, 29(4), pp. 614-626.

Cruden, D. M., & Varnes, D. J. (1996). Landslides: investigation and mitigation. Chapter 3-Landslide types and processes. Transportation research board special report, (247).

Cui, Y., Cheng, D., Choi, C., Jin, W., Lei, Y., & Kargel, J. (2019). The cost of rapid and haphazard urbanization: lessons learned from the Freetown landslide disaster. Landslides, 16(6), pp. 1167-1176.

Cui, Y., Miller, D., Schiarizza, P., & Diakow, L. (2018). British Columbia digital geology. British Columbia Ministry of Energy, Mines and Petroleum Resources. British Columbia Geological Survey Open File 2015-2.

Dai, K., Li, Z., Xu, Q., B. R., Milledge, D., Tomas, R., . . . Zhang, Q. (2020). Entering the era of earth observation-based landslide warning systems: A novel and exciting framework. IEEE Geoscience and Remote Sensing Magazine, pp. 136-153. doi:10.1109/MGRS.2019.2954395

Dehls, J., Lauknes, T., Hermanns, R., Bunkholt, H., Grydeland, T., Larsen, Y., . . . Eiken, T. (2014). Use of satellite and ground based InSAR in hazard classification of unstable rock slopes. Landslide Science for a Safer Geoenvironment, pp. 389-392. doi:10.1007/978-3-319-0505-8_60

Del Ventisette, C., Casagli, N., Fortuny-Guasch, J., & Tarchi, D. (2012). Ruinon landslide (Valfurva, Italy) activity in relation to rainfall by means of GBInSAR monitoring. Landslides, 9(4), pp. 497-509. doi:10.1016/j.geomorph.2019.03.014

Delgado Blasco, J., Foumelis, M., Stewart, C., & Hooper, A. (2019). Measuring urban subsidence in the Rome metropolitan area (Italy) with Sentinel-1 SNAP-StaMPS persistent scatterer interferometry. Remote Sensing, 11(2), pp. 1-17.

Deline, P., Gruber, S., Amann, F., Bodin, X., Delaloye, R., Failletaz, J., ... & Weber, S. (2021). Ice loss from glaciers and permafrost and related slope instability in high-mountain regions. In Snow and ice-related hazards, risks, and disasters (pp. 501-540). Elsevier.

Dini, B., Manconi, A., Loew, S., & Chophel, J. (2020). The Punatsangchhu-I dam landslide illuminated by InSAR multitemporal analyses. Scientific reports, 10(1), pp. 1-10. doi:10.1038/s41598-020-65192-w

Dong, J., Liao, M., Xu, Q., Zhang, L., Tang, M., & Gong, J. (2018). Detection and displacement characterization of landslides using multi-temporal satellite SAR interferometry: A case study of Danba County in the Dadu River Basin. Engineering Geology, 240, pp. 95-109. doi:10.1016/j.enggeo.2018.04.015

Duro, J., Iglesias, R., Monells, D., & Calvo, R. (2020). Exploitation of InSAR techniques as a support of in situ sensors to improve safety and productivity in mining operations. Proceedings of the 2020 International Symposium on Slope Stability in Open Pit Mining and Civil Engineering, pp. 1531-1546. doi:10.36487/ACG_repo/2025_106

Earle, S. (2019). Physical Geology-2nd Edition. Victoria , BC: BC Campus.

Ekstrom, G., Nettles, M., & Tsai, V. (2006). Seasonality and increasing frequency of Greenland glacial earthquakes. Science, 311(5768), pp. 1756-1758. doi:10.1126/science.1122112

ESA. (2022). Mission ends for Copernicus Sentinel-1B satellite. Retrieved from The Eoropean Space Agency: https://www.esa.int/Applications/Observing_the_Earth/Copernicus/Sentinel-1/Mission_ends_for_Copernicus_Sentinel-1B_satellite

Evans, S. (1982). Landslides and surficial deposits in urban areas of British Columbia: a review. Canadian Geotechnical Journal, 19(3), pp. 269-288.

Evans, S. (1987). A rock avalanche from the peak of Mount Meager, British Columbia. Current Research part A, Geological Survey of Canada.

Evans, S., Hugr, O., & Claque, J. (2001). Dynamics of the 1984 rock avalanche and associated distal debris flow on Mount Cayley, British Columbia, Canada; implications for landslide hazard assessment on dissected volcanoes. Engineering Geology, 61(1), pp. 29-51. doi:10.1016/S0013-7952(00)00118-6.

Ferretti, A., Monti-Guarnieri, A., Prati, C., Rocca, F., & Massonet, D. (2007). InSAR principles-guidelines for SAR interferometry processing and interpretation. Noordwijk, Netherlands: ESA Publications.

Ferretti, A., Prati, C., & Rocca, F. (2001). Permanent scatterers in SAR interferometry. IEEE Transactions on geoscience and remote sensing, 39(1), pp. 8-20. doi:10.1109/36.898661

Flentje, P., Chowdhury, R. T., & Brizaga, V. (2005). Towards real-time landslide risk management in an urban area. pp. 1-11.

Friele, P., Jakob, M., & Claque, J. (2008). Hazard and risk from large landslides from Mount meager volcano, British Columbia, Canada. Georisk, 2(1), pp. 48-64. doi:10.1080/17499510801958711

Friele, P.; Millard, T.H.; Mitchell, A.; Allstadt, K.E.; Menounos, B.; Geertsema, M.; Clague, J.J. (2021). Observations on the May 2019 Joffre Peak landslides, British Columbia. Landslides, 17(4), pp. 913-930. doi:10.1007/s10346-019-01332-2

Fukuzono, T. (1985). A new method for predicting the failure time of a slope failure. Proceedings of the 4th International Conference and Field Workshop on Landslide, pp. 145-150.

Gabriel, A., Goldstein, R., & Zebker, H. (1989). Mapping small elevation changes over large areas: Differential radar interferometry. Journal of Geophysical Research: Solid Earth, 94(B7), pp. 9183-9191. doi:10.1029/jB094iB07p09183

Gaffet, S., Guglielmi, Y., Cappa, F., Pambrun, C., Monfret, T., & Amitrano, D. (2010). Use of the simultaneous seismic, GPS and meteorological monitoring for the characterization of a large unstable mountain slope in the southern French Alps. Geophysical Journal International, 182(3), pp. 1395-1410. doi:10.1111/j.1365-246X.2010.04683.x

Geertsema, M., Menounos, B., Bullard, G., Carrivick, J., Clague, J., Dai, C., . . . Pichierri, M. (2022, March). The 28 November 2020 landslide, tsunami, and outburst flood–a hazard cascade associated with rapid deglaciation at Elliot Creek, British Columbia, Canada. Geophysical research letters, 49(6), p. p.e2021GL096716. doi:10.1029/2021GL096716

Glade, T., & Crozier, M. (2005). A review of scale dependency in landslide hazard and risk analysis. Landslide hazard and risk, pp. 75-138.

Government of Canada. (2023, 03 12). Government of Canada. Retrieved from Historical Data: https://climate.weather.gc.ca/historical_data/search_historic_data_e.html

Government of Canada. (2023, 03 12). Search the Earthquake Database. Retrieved from Government of Canada: https://www.earthquakescanada.nrcan.gc.ca/stndon/NEDB-BNDS/bulletin-en.php

Grebby, S., Sowter, A., Gee, D., Athab, A., Barreda-Bautista, B., Girindran, R., & Marsh, S. (2021). Remote Monitoring of Ground Motion Hazards in High Mountain Terrain Using InSAR: A Case Study of the Lake Sarez Area, Tajikistan. Applied Sciences, 11(18), pp. 1-17. doi:10.3390/app11188738

Green, N. (1990). Late Cenozoic volcanism in the Mount Garibaldi and Garibaldi Lake volcanic fields, Garibaldi volcanic belt, southwestern British Columbia. Geoscience Canada, 17(3), pp. 171-175.

Green, N., Armstrong, R., Harakal, J., Souther, J., & Read, P. (1988). Eruptive history and K-Ar geochronology of the late Cenozoic Garibaldi volcanic belt, southwestern British Columbia. Geological Society of America Bulletin, 100(4), pp. 563-579. doi:10.1130/0016-7606(1988)100<0563:EHAKAG>2.3.CO;2

Hermanns, R., Niedermann, S., Ivy-Ochs, S., & Kubik, P. (2004). Rock avalanching into a landslide-dammed lake causing multiple dam failure in Las Conchas valley (NW Argentina)—evidence from surface exposure dating and stratigraphic analyses. Landslides, 1(2), pp. 113-122. doi:10.1007/s10346-004-0013-5

Hoeser, T. (2018). Analysing the capabilities and limitations of InSAR using Sentinel-1 data for landslide detection and monitoring. Doctoral dissertation, Department of Geography, University of Bonn. doi:10.13140/RG.2.2.35085.59362

Hoeser, T. (2020). StaMPS_Visualizer. v3.0. Zenodo. doi:10.5281/zenodo.4407188

Holm, K., Bovis, M., & Jakob, M. (2004). The landslide response of alpine basins to post-Little Ice Age glacial thinning and retreat in southwestern British Columbia. Geomorphology, 57(3-4), pp. 201-216. doi:10.1016/S0169-555X(03)00103-X

Hooper, A. (2008). A multi-temporal InSAR method incorporating both persistent scatterer and small baseline approaches. Geophysical Research Letters, 35(16). doi:10.1029/2008GL034654

Hooper, A. (2010). A statistical-cost approach to unwrapping the phase of InSAR time series. Proceedings of the International Workshop on ERS SAR Interferometry. Frascati, Italy.

Hooper, A., Bekaert, D., Spaans, K., & Arıkan, M. (2012). Recent advances in SAR interferometry time series analysis for measuring crustal deformation. Tectonophysics(514), pp. 1-13. doi:10.1016/j.tecto.2011.10.013

Hooper, A., Zebker, H., Segall, P., & Kampes, B. (2004). A new method for measuring deformation on volcanoes and other natural terrains using InSAR persistent scatterers. Geophysical Research Letters, 31(23).

Huggel, C., Clague, J., & Korup, O. (2012). Is climate change responsible for changing landslide activity in high mountains? Earth Surface Processes and Landforms, 37(1), pp. 77-91. doi:10.1002/esp.2223

Hugonnet, R., McNabb, R., Berthier, E., Menounos, B., Nuth, C., Girod, L., . . . Kääb, A. (2021). Accelerated global glacier mass loss in the early twenty-first century. Nature, 592(7856), pp. 726-731. doi:10.1038/s41586-021-03436-z

Huntley, D., Bobrowsky, P., Macleod, R., Cocking, R., Joseph, J., & Rotheram-Clarke, D. (2021). Field testing innovative geospatial and photogrammetric monitoring technologies in mountainous terrain near Ashcroft, British Columbia. Journal of Mountain Science, 18(1), pp. 1-20.

Intrieri, E., Carlà, T., & Gigli, G. (2019). Forecasting the time of failure of landslides at slope-scale: A literature review. Earth-Science Reviews(193), pp. 333-349. doi:10.1016/j.earscirev.2019.03.019

Intrieri, E., Raspini, F., Fumagalli, A., Lu, P., Del Conte, S., Farina, P., . . . Casagli, N. (2018). The Maoxian landslide as seen from space: detecting precursors of failure with Sentinel-1 data. Landslides, 15(1), pp. 123-133. doi:10.1007/s10346-017-0915-7

Jakob, M., Hungr, O., Friele, P., & Clague, J. (2005). Multifaceted hazard assessment of Cheekye fan, a large debris-flow fan in south-western British Columbia. In Debris-flow Hazards and Related Phenomea pp. 659-683. Berlin: Praxis Springer.

Kilburn, C., & Petley, D. (2003). Forecasting giant, catastrophic slope collapse: lessons from Vajont, Northern Italy. Geomorphology, 54(1-2), pp. 21-32. doi:10.1016/S0169-555X(03)00052-7

Kim, J., Coe, J., Lu, Z., Avdievitch, N., & Hults, C. (2022). Spaceborne InSAR mapping of landslides and subsidence in rapidly deglaciating terrain, Glacier Bay National Park and Preserve and vicinity, Alaska and British Columbia. Remote Sensing of Environment, 281, pp. 1-16. doi:10.1016/j.rse.2022.113231

Kos, A., Amann, F., Strozzi, T., Delaloye, R., von Ruette, J., & Springman, S. (2016). Contemporary glacier retreat triggers a rapid landslide response, Great Aletsch Glacier, Switzerland. Geophysical Research Letters, 43(24), p. 12. doi:10.1002/2016GL071708

Lacasse, S., Nadim, F., Lacasse, S., & Nadim, F. (2009). Landslide risk assessment and mitigation strategy. In K. Sassa, & P. Canuti, Landslides – Disaster Risk Reduction. pp. 31-61. Berlin: Springer. doi:10.1007/978-3-540-69970-5_3

Lacroix, P., Belart, J., Berthier, E., Sæmundsson, Þ., & Jónsdóttir, K. (2022). Mechanisms of landslide destabilization induced by glacier-retreat on Tungnakvíslarjökull area, Iceland. Geophysical Research Letters, 49(14), p. e2022GL098302. doi:10.1029/2022GL098302

Lazecky, M., Comut, F., Nikolaeva, E., Bakon, M., Papco, J., Ruiz Armenteros, A., . . . Ondrejka, P. (2016). Potential of Sentinel-1A for nation-wide routine updates of active landslide maps. International Archives of the Photogrammetry, Remote Sensing and Spatial Information Sciences. pp. 1-7. doi: 10.5194/isprs-archives-XLI-B7-775-2016

Li, M., Zhang, L., Ding, C., Li, W., Luo, H., Liao, M., & Xu, Q. (2020). Retrieval of historical surface displacements of the Baige landslide from time-series SAR observations for retrospective analysis of the collapse event. Remote Sensing of Environment(240), pp. 1-11. doi:10.1016/j.rse.2020.11695

Liu, S., Segoni, S., Raspini, F., Yin, K., Zhou, C., Zhang, Y., & Casagli, N. (2020). Satellite InSAR as a New Tool for the Verification of Landslide Engineering Remedial Works at the Regional Scale: A Case Study in the Three Gorges Reservoir Area, China. Applied Sciences, 10(18), pp. 1-18 doi:10.3390/app1018643

Lu, C., Ni, C., Chang, C., Yen, J., & Chuang, R. (2018). Coherence difference analysis of Sentinel-1 SAR interferogram to identify earthquake-induced disasters in urban areas. Remote Sensing, 10(8), pp. 1-21 doi:10.3390/rs10081318

Mancini, F., Grassi, F., & Cenni, N. (2021). A workflow based on SNAP–StaMPS open-source tools and GNSS data for PSI-Based ground deformation using dual-orbit Sentinel-1 data: Accuracy assessment with error propagation analysis. Remote Sensing, 13(4), pp. 1-22 doi:10.3390/rs13040753

Masson-Delmotte, V. P., Zhai, P., Pirani, S. L., Connors, C., Péan, S., Berger, N., ... & Scheel Monteiro, P. M. (2021). Ipcc, 2021: Summary for policymakers. in: Climate change 2021: The physical science basis. contribution of working group i to the sixth assessment report of the intergovernmental panel on climate change.

Massey, N., MacIntyre, D., Desjardins, P., & Cooney, R. (2005). Digital geology map of British Columbia: whole province. BC Ministry of Energy and Mines, GeoFile 1, 2005-1

Mateos, R., Azañón, J., Roldán, F., Notti, D., Pérez-Peña, V., Galve, J., . . . Devantèry, N. (2017). The Combined Use of PSInSAR and UAV Photogrammetry Techniques for the Analysis of the Kinematics of a Coastal Landslide Affecting an Urban Area (SE Spain). Landslides, 14(2), pp. 743-754.

Mazzanti, P., Antonielli, B., Sciortino, A., Scancella, S., & Bozzano, F. (2021). Tracking Deformation Processes at the Legnica Glogow Copper District (Poland) by Satellite InSAR—II: Żelazny Most Tailings Dam. Land, 10(6), p. 1-20. doi:10.3390/land10060654

McNeely, R., & McCuaig, S. (1991). Geological Survey of Canada radiocarbon dates XXIX. Geological Survey of Canada, Paper 89-7, pp. 1-132

Michoud, C., Baumann, V., Lauknes, T., Penna, I., Derron, M., & Jaboyedoff, M. (2016). Large Slope Deformations Detection and Monitoring Along Shores of the Potrerillos Dam Reservoir, Argentina, Based on a Small-Baseline InSAR Approach. Lanslides, 13(3), pp. 451-466.

Mokievsky-Zubok, O. (1977). Glacier-caused slide near Pylon Peak, British Columbia. Canadian Journal of Earth Sciences, 14(11), pp. 2657-2662. doi:10.10.1139/e77-230

Monti Guarnieri, A., & Rocca, F. (2017). Options for continuous radar Earth observations. Science China Information Sciences, 60(6), pp. 1-5. doi:10.1007/s11432-016-9067-7

Morgan, J., Boudreau, A., Verdugo, M., Meloni, F., & Colombo, D. (2020). New satellite sensors for monitoring mining areas: a look at the future. Slope Stability 2020: Proceedings of the 2020 International Symposium on Slope Stability in Open Pit Mining and Civil Engineering, pp. 1521-1530. Perth, Australia: Australian Centre for Geomechanics.

Necula, N., Niculiță, M., Tessari, G., & Floris, M. (2017). InSAR analysis of Sentinel-1 data for monitoring landslide displacement of the north-eastern Copou hillslope, Iaşi city, Romania. Proceedings of Romanian geomorphology symposium, pp. 11-14. Lasi City, Romania.

O'Neel, S., Larsen, C., Rupert, N., & Hansen, R. (2010). Iceberg calving as a primary source of regional-scale glacier-generated seismicity in the St. Elias Mountains, Alaska. Journal of Geophysical Research: Earth Surface, 115, pp. 1-12. doi:10.1029/2009JF001598, 2010

Osmanoğlu, B., Sunar, F., Wdowinski, S., & Cabral-Cano, E. (2016). Time series analysis of InSAR data: Methods and trends. ISPRS Journal of Photogrammetry and Remote Sensing,, 115, pp. 90-102. doi:10.1016/j.isprsjprs.2015.10.003

Paek, S., Balasubramanian, S., Kim, S., & de Weck, O. (2020). Small-satellite synthetic aperture radar for continuous global biospheric monitoring: A review. Remote Sensing, 12(16), pp. 1-31. doi:0.3390/rs12162546

Petley, D. (2020a). Koidern Landslide: a long runout event in Canada. AGU Blogshere: https://blogs.agu.org/landslideblog/2020/09/07/koidern-landslide/

Petley, D. (2020b). Taku river: another very large landslide in British Columbia, Canada. AGU Blogsphere: https://blogs.agu.org/landslideblog/2020/12/29/taku-river-landslide-1/

Petley, D. (2022). The 1 September 2022 rock avalanche on the Ecstall river in British Columbia, Canada. AGU Blogsphere: https://blogs.agu.org/landslideblog/2022/09/21/ecstall-river-1/

Pollon, C. (2021, August 17). A Massive Landslide sends a wake-up to BC's mining sector. The Tyee: https://thetyee.ca/News/2021/08/17/Massive-BC-Landslide-Sends-Wake-Up-Mining-Sector/

Porter, M., & Morgenstern, N. (2013). Landslide risk evaluation: Canadian technical guidelines and best practices related to landslides: a national initiative for loss reduction. Geological Survey of Canada, Open File 7312, pp. 1-21.

Ramirez, R., Lee, S., & Kwon, T. (2020). Long-term remote monitoring of ground deformation using Sentinel-1 interferometric synthetic aperture radar (InSAR): Applications and insights into geotechnical engineering practices. Applied Sciences, 10(21), pp. 1-20. doi:10.3390/app10217447

Raspini, F., Bianchini, S., Ciampalini, A., Del Soldato, M., Solari, L., Novali, F., . . . Casagli, N. (2018). Continuous, semi-automatic monitoring of ground deformation using Sentinel-1 satellites. Scientific Reports, 8(1), pp. 1-11. doi:10.1038/s41598-018-25369-w

Read, P. B. (1990). Mount Meager Complex, Garibaldi Belt, southwestern British Columbia. Geoscience Canada, 17(3), pp. 167-170.

Roberti, G., Ward, B., van Wyk de Vries, B., Friele, P., Perotti, L., Clague, J., & Giardino, M. (2018). Precursory slope distress prior to the 2010 Mount Meager landslide, British Columbia. Landslides, 15(4), pp. 637-647. doi:10.1007/s10346-017-0901-0

Rocca, F. (1997). An overview of SAR interferometry. In Proc. 3re ERS Symp. Florence.

Rocca, F. P. (1997). Possibilities and limits of SAR interferometry. In Image Processing Techniques. First Latino-American Seminar on Radar Remote Sensing, (p. 15). Buenos Aires, Argentina.

Rogers, A., & Ingalls, R. (1969). Venus: Mapping the surface reflectivity by radar interferometry. Science, 165(3895), pp. 797-799. doi:10.1126/science.165.3895.797

Rouyet, L., Lauknes, T., Christiansen, H., Strand, S., & Larsen, Y. (2019). Seasonal dynamics of a permafrost landscape, Adventdalen, Svalbard, investigated by InSAR. Remote Sensing of Environment, 231, p. 111236. doi:10.1016/j.rse.2019.111236

Roy, P., Martha, T., Khanna, K., Jain, N., & Kumar, K. (2022). Time and path prediction of landslides using InSAR and flow model. Remote Sensing of Environment, 271, pp. 1-14. doi:10.1016/j.rse.2022.112899

Saito, M. (1969). Forecasting Time of Slope failure by Tertiary Creep. Proceedings of the 7th International Conference on Soil Mechanics and Foundation Engineering, 2, pp. 677-683. Mexico City.

Saito, M., & Uezawa, M. (1961). Failure of soil due to creep. Proceedings of the 5th International Conference on Soil Mechanics and Foundation Engineering, 1, pp. 315-318. Mexico City.

Schaefer, L., Di Traglia, F., Chaussard, E., Lu, Z., Nolesini, T., & Casagli, N. (2019). Monitoring volcano slope instability with Synthetic Aperture Radar: A review and new data from Pacaya (Guatemala) and Stromboli (Italy) volcanos. Earth-science reviews(192), pp. 236-257. doi:10.1016/j.erscirev.2019.03.009

Schwab, J., Gori, P., & Jeer, S. (2005). Landslide and Planning. American Planning Association.

Shugar, D., Jacquemart, M., Shean, D., Bhushan, S., U. K., Sattar, A., . . . Emmer, A. (2021). A massive rock and ice avalanche caused the 2021 disaster at Chamoli, Indian Himalaya. Science, 373(6552), pp. 300-306. doi:10.1126/science.abh4455

SNAP. (2020). ESA Sentinel Application Platform v8.03. Retrieved from http://step.esa.int

Squarzoni, G., Bayer, B., Franceschini, S., & Simoni, A. (2020). Pre-and post-failure dynamics of landslides in the Northern Apennines revealed by space-borne synthetic aperture radar interferometry (InSAR). Geomorphology(369), pp. 1-12. doi:10.1016/j.geomorph.2020.107353

Stewart-Jones, E., & Gruber, S. (2023). Transferring Cryosphere Knowledge between Mountains Globally: A Case Study of Western Canadian Mountains, the European Alps and the Scandes. Journal of Alpine Research| Revue de géographie alpine, (111-2). doi:10.4000/rga.12203

Strozzi, T., Luckman, A., Murray, T., Wegmuller, U., & Werner, C. (2002). Glacier motion estimation using SAR offset-tracking procedures. IEEE Transactions on Geoscience and Remote Sensing, 40(11), pp. 2384-2391. doi:10.1109/TGRS.2002.805079

Svennevig, K., Dahl-Jensen, T., Keiding, M., Merryman Boncori, J., Larsen, T., Salehi, S., . . . Voss, P. (2020). Evolution of events before and after the 17 June 2017 rock avalanche at Karrat Fjord, West Greenland–a multidisciplinary approach to detecting and locating unstable rock slopes in a remote Arctic area. Earth Surface Dynamics, 8(4), pp. 1021-1038. doi:10.5194/esurf-8-1021-2020

Tavenas, F., & Leroueil, S. (1981). Creep and failure of slopes in clays. Canadian Geotechnical Journal, 18(1), pp. 106-120. doi:10.1139/t81-010

Terzaghi, K. (1950). Mechanism of landslides. In Application of Geology to Engineering Practice (Berkeley Volume) pp. 82-123. Washington, DC, USA: Geological Society of America. doi:10.1130/Berkey.1950

Turner, A. K. (2018). Social and environmental impacts of landslides. Innovative Infrastructure Solutions, 3, 1-25. 10.1007/s41062-018-0175-y

van der Kooij, M., & Lambert, A. (2002). Results of processing and analysis of large volumes of repeat-pass InSAR data of Vancouver and Mount Meager (BC). IEEE International Geoscience and Remote Sensing Symposium, 2, pp. 1228-1230. doi:10.1109/IGARSS.2002.1025897

Voight, B. (1988). A method for prediction of volcanic eruption. Nature, 332(6160), pp. 125-130. doi:10.1038/332125a0

Wang, L., Marzahn, P., Bernier, M., & Ludwig, R. (2020). Sentinel-1 InSAR measurements of deformation over discontinuous permafrost terrain, Northern Quebec, Canada. Remote Sensing of Environment, 248, pp. 1-21. doi:10.1016/j.rse.2020.111965

Wang, X. (2015). An Adaptive approach of satellite baseline estimation in InSAR. International Journal of Geosciences, 6(12), pp. 1-6.

Ward, B., Williams-Jones, G., & Geertsema, M. (2020). Moving mountains: Landslides and Volcanoes in a Warming Cryosphere. The Alpine Club of Canada, pp. 1-4.

Weaver, A. (2003). The science of climate change. Geoscience Canada, 30(3), pp. 91-109.

Winberry, J., Huerta, A., Anandakrishnan, S., Aster, R., Nyblade, A., & Wiens, D. (2020). Glacial earthquakes and precursory seismicity associated with Thwaites Glacier calving. Geophysical Research Letters, 47(3), p. e2019GL086178. doi:10.1029/2019GL086178

Wright, T., Parsons, B., & Lu, Z. (2004). Toward mapping surface deformation in three dimensions using InSAR. Geophysical Research Letters, 31(1). doi:10.1029/2003GL018827

Yagüe-Martínez, N., Prats-Iraola, P., Gonzalez, F., Brcic, R., Shau, R., Geudtner, D., . . . Bamler, R. (2016). Interferometric processing of Sentinel-1 TOPS data. IEEE Transactions on Geoscience and Remote Sensing, 54(4), pp. 2220-2234.